Technische Universität München (TUM)
Fakultät für Elektrotechnik und Informationstechnik
Lehrstuhl für Hochfrequenztechnik

Semianalytical methods in the design of transparent metasheets with applications to microwave radomes

Ezgi Öziş

Vollständiger Abdruck der von der Fakultät für Elektrotechnik und Informationstechnik der Technischen Universität München zur Erlangung des akademischen Grades eines Doktor-Ingenieurs genehmigten Dissertation.

Vorsitzender:	Prof. Dr.-Ing. Bernhard Seeber
Prüfer der Dissertation:	1. Prof. Dr.-Ing. Thomas F. Eibert
	2. Prof. Dr.-Ing. Alberto Moreira

Die Dissertation wurde am 12.12.2019 bei der Technischen Universität München eingereicht und durch die Fakultät für Elektrotechnik und Informationstechnik am 20.05.2020 angenommen.

Acknowledgements

The presented work has been carried out during my time in the High Frequency and Radar Institute of Deutsches Zentrum Luft und Raumfahrt (DLR), in Oberpfaffenhofen. I would like to express my gratitude to a number of people who supported me during my PhD study.
It has been a great honor that Prof. Dr.-Ing. Thomas F. Eibert was my supervisor in TUM during my PhD study and his door was always open to have useful discussions about my research and also whenever I experienced difficulties. I am also gratefully and deeply indebted to his guidance and supervision on my thesis in that he steered me in the right direction. I also want to thank my supervisor Dr. rer. nat. habil. Andrey V. Osipov in DLR who supported me with his professional advice.
I am also grateful to Prof. Dr.-Ing. Alberto Moreira and Dr.-Ing. Thomas Neff who gave an excellent administrative support in our institute in DLR. Without their precious support, it would not be possible to conduct this research. I wish to express my sincere thanks for providing me with all the necessary facilities for the research.
My thanks also go to Stefan Thurner who did the measurements and took the photos of the measurement setup in Tech laboratory in DLR.
Last but not the least, I am grateful to my family for their encouragement, always believing in me, taking care and loving me.

Abstract

In recent years, metamaterials have been attracting immense attention in electrical and optical engineering. These are artificial materials which are engineered to shape the electromagnetic responses and properties. Metamaterials are realized by the adjustment of many electrically small inclusions in a dielectric substrate. Changing size, position and shape of those particles affects the electromagnetic response. Two-dimensional metamaterials are called metasheets, and their application to microwave radomes is the subject of this study.

While there exist closed expressions for the scattering parameters of some geometrical structures, for others such expressions cannot be found and only full-wave simulations can be used. Despite its geometrical simplicity, the circular ring inclusion belongs to the latter group. A dimensional parametric analysis with full-wave simulations is performed in this thesis to understand the electromagnetic response of an infinite planar periodic array of circular rings.

An important aim of this thesis is to find a way of controlling microwave transmission through metasheets realized as periodic planar arrays of circular inclusions. As the transmission is dominated by the geometrical parameters of the circular inclusions, it is useful to find an analytical expression for the transmission coefficient as a function of those geometrical parameters. This expression cannot be derived from first principles. Thus, an empirical expression with free parameters is proposed to describe the transmission behavior of the metasheet by using the results of full-wave simulations at discrete values of the geometrical parameters of the ring inclusions. The free parameters are determined by fitting so that the simulated values for the transmission coefficient are recovered in the best way.

As an application of this semianalytical method, a metasheet (metalens) compensating the phase distortions of a hemispheric radome for a fixed frequency in the Ka-band is designed. The phase distortions are calculated by ray tracing and the resulting fields are incident on the metasheet. The electric fields transmitted through the finite electrically large metasheet is calculated by Physical Optics (PO) upon homogenization of the metasheet. To check the accuracy of the approach, the method is firstly applied to a circular finite electrically large metasheet

with circular rings as inclusions. In order to decrease the complexity of the calculation, the equivalent surface currents are calculated by using the tranmission coeffcient of the homogenized metasheet, and cylindrical coordinates are chosen to reduce the two-dimensional integral to a line integral over the rim of the metasheet. In the PO calculation for the hemispheric radome, the PO integration surface is subdivided into small facets, followed by an expansion in Taylor series of the phase part of the free-space Green function, which permits analytical integration. The approach provides a good estimation of the electromagnetic response of the metalens, which is confirmed by measurements.

Kurzfassung

In den letzten Jahren haben Metamaterialien in der Elektrotechnik und Optik immense Beachtung gefunden. Diese sind künstliche Materialien, die entwickelt werden, um bestimmte elektromagnetische Reaktionen und Eigenschaften zu erzeugen. Metamaterialien werden durch die Anordnung vieler elektrisch kleiner Einschlüsse in eine Trägerstruktur hergestellt.

Das Ändern von Größe, Position und Form dieser Partikel beeinflusst die elektromagnetische Reaktion. Diese Arbeit konzentriert sich auf zweidimensionale Metamaterialien, sogenannte Metasheets, und deren Anwendung auf Mikrowellenradome.

Während es geschlossene analytische Ausdrücke gibt, um die Streuparameter für einige geometrische Strukturen zu berechnen, können für andere solche Ausdrücke nicht gefunden werden und ihre Analyse ist nur mit Vollwellensimulationen möglich. Trotz seiner geometrischen Einfachheit gehört der Kreisringeinschluss zu der letzteren Gruppe. Eine umfassende parametrische Analyse wird in dieser Arbeit mit Vollwellensimulationen durchgeführt, um die elektromagnetische Antwort einer unendlichen planaren periodischen Anordnung von Kreisringen zu verstehen.

Ein wesentliches Ziel dieser Arbeit ist es, die Mikrowellentransmission durch Metasheets als unendliche planare periodische Anordnungen kreisförmiger Einschlüsse zu steuern. Da die Transmission durch die geometrischen Parameter der kreisförmigen Einschlüsse bestimmt wird, ist es notwendig einen analytischen Ausdruck für den Transmissionskoeffizienten als Funktion dieser geometrischen Parameter zu finden. Dieser Ausdruck kann nicht aus physikalischen Grundprinzipien abgeleitet werden. Daher wird ein empirischer Ausdruck mit freien Parametern verwendet, um das Übertragungsverhalten des Metasheets zu beschreiben, das durch Vollwellensimulationen bei diskreten Werten für die geometrischen Parameter der Ringeinschlüsse bestimmt wird. Die freien Parameter des empirischen Ausdrucks für den Transmissionskoeffizienten werden so angepasst, dass die simulierten Werte für den Transmissionskoeffizienten am besten übereinstimmen.

Als Anwendung dieser semianalytischen Methode wird ein Metasheet entworfen, das die Phasenverzerrungen eines hemisphärischen Radoms bei Frequenzen um 28 GHz im Ka-Band

ausgleicht. Die Phasenverzerrungen des hemisphärischen Radoms werden durch Ray Tracing berechnet. Das Ergebnis wird als Designziel für das Metasheet verwendet. Das durch das endliche elektrisch große Metasheet transmittierte elektrische Feld wird mit Hilfe von Approximation der Physikalischen Optik (PO) berechnet. Zur Überprüfung der Genauigkeit der PO-Berechnung wird die PO zunächst für ein kreisförmiges elektrisch großes Metasheet mit Kreisringen verwendet. Um die Komplexität der Berechnung zu verringern, wird eine äquivalente Näherung der Oberflächenströme verwendet und die Zylinderkoordinaten werden so gewählt, dass das zweidimensionale Integral zu einem Linienintegral reduziert werden kann. Bei der PO-Berechnung für die Anwendung des hemisphärischen Radoms werden Taylorreihen im Phasenteil der Freiraum-Green-Funktion und die mit der semianalytischen Methode bestimmten Transmissionskoeffizienten verwendet. Das Ergebnis dieser Berechnung liefert eine gute Schätzung der elektromagnetischen Reaktion, die durch Messungen bestätigt wird.

Contents

List of Figures

List of Tables

Chapter 1

Introduction

1.1 Importance of metamaterials

Metamaterials are periodic structures with unit cells smaller than the wavelength of the incident wave engineered to modify the wave propagation by changing the size and the design of the unit cells. The properties of such artificial materials can be controlled well. Such a control gives a chance to develop new technological properties. As an example, metamaterials can influence the radiation pattern of antennas or scattering properties of various objects. Metamaterials can also have unusual propeties, which are not present in natural materials. This is the main difference between conventional materials and metamaterials. Another benefit of using metamaterials is that they can increase the performance of electromagnetic devices and decrease the cost and the size of devices [Cened].

1.2 History of radomes

The design of radomes has been studied since the 1940s with increased interest. A radome is an important component of many antenna systems, which protects the antenna from environmental effects such as rain, ice, wind. Also, it streamlines the design to reduce the aerodynamic drag. On the other hand, the radome should not affect the performance of the antenna negatively. In the radome design, choosing a suitable material is the key point; therefore, material technology and material engineering help to improve the capabilities of a radome. Radomes are mainly used in aerospace and radar technology [JW70]. There are different kinds of radomes [Sha18]. Radomes can be differently shaped as shown in Figs. 1.1 and 1.2 depending on the type of application. The shape of the nose is the critical part of the radome, particularly for rapidly moving objects such as an aircraft or a missile [CB16]. To increase the aerodynamical performance of radomes, mathematical modelling and engineering studies are necessary [CB16].

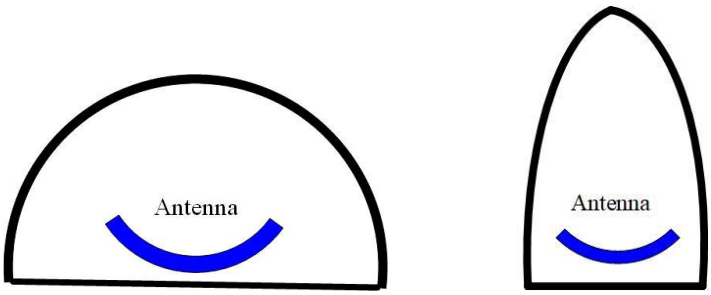

(a) Hemisphere (b) Elliptical

Figure 1.1 Hemispheric and eliptical radomes.

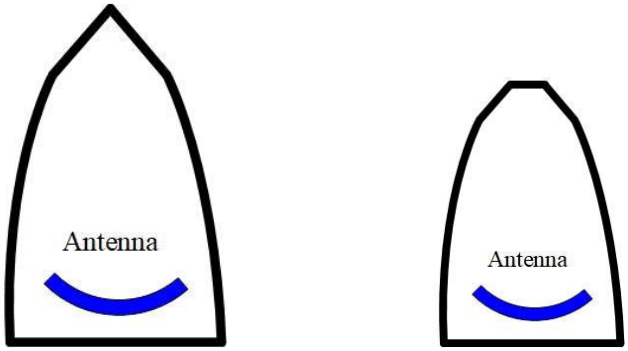

(a) Ogival shape with sharp nose (b) Ogival shape with flat nose

Figure 1.2 Ogival shaped radomes with different nose types.

The developments of the radome between 1940 and 1970 are briefly addressed in this section in order to better understand the critical points in the radome design. A first operational hemispheric radome was designed for the Boeing B-18A in 1941. The material of the radome was plexiglass (a kind of thermoplastic polymer) [Das15]. This radome was used in a radar test for improving the guidance of the bomber. Tests indicated the suitability of the radome [JW70]. For radomes in the radar applications in 1941, plywood was chosen for radomes used for Navy patrol torpedo boats and aircrafts. Plywood has the negative property of absorbing moisture, which distorts the performance of the radome. For solving this problem, resin impregnated glass fabric was used as an additional layer on the plywood material to block moisture, but the tests were insufficiently successful. Then, three different materials were tried to handle the moisture problem better. Firstly, polystyrene foam was used. It showed a good electrical performance but it could not resist properly to the heavy mechanical stress. Secondly, phenolic-resin impregnated cotton canvas was used. It had good strengths. Thirdly, glass cloths which are similar to resin reinforcing materials, were utilized. Foam, plywood and different kinds of resins were used for

constructing radomes in the past [Das15]. The aspects involved in the fabrication of a radome include thermal properties, rain erosion resistance, mechanical and electrical properties [Nas96]. The thickness of the walls of the radome is the key parameter that affects the electrical performance of the radome and the antenna. The radome should be thin to reduce reflections and improve the transmission. Ideally, if it is thinner than the operational wavelength of the radar or antenna and the permittivity of the radome material is close to unity, the transmission can be increased. The thickness of the walls should be increased to increase the mechanical strength of the radomes but it affects the electrical performance negatively.

After 1942, the research interest on the electrical properties of radomes started to increase. As a test design, a sandwich radome with three layers was developed in the Radiation Laboratory, Massachusetts Institute of Technology [JW70]. The preferred material for this design was laminated glass-fabric skin combined with cellular core of polystyrene fiber material with low density. During 1955 and 1956, glass ceramic was used for the design of radomes. These radomes were used for the Navy's Tarter, Terrier missile systems, Air Force's Gar IX and Gar XI and the Navy's Shrike and Typhon [JW70]. During the 1960s, cordierite, boron nitride, silicon nitride got on a new significance. Choosing a wrong material can decrease mechanical sustainability and degrade the electrical performance. Therefore, the materials should be analyzed carefully and measured [SS68]. The electrical performance of a radome is affected by not only the type of materials but also the shape of a radome. The geometry of the radome, being mainly decided by aerodynamic needs, often leads to a severe decrease of the electrical performance of enclosed antennas [CRT81].

For analyzing the electromagnetic properties of radomes, several assumptions are often made to simplify the calculations and analyses. For example, plane wave solutions are often used in the analysis of the wave propagation because of the large distances between transmitting and receiving antennas. The plane wave solutions are applicable to electrically large antennas and radomes [Sha18]. Under the plane wave assumption, the curved radome is considered as locally planar. For flat surfaces, conventional boundary conditions can be applied to account for the polarization, incidence angle, and frequency of the wave.

The type of material is a key element in the design of a radome with improved electrical properties. However, the choice of material cannot improve all electrical properties at once. The combination of natural and artificial materials for designing the surface of the radome can bring additional features to the radome.

1.3 Some historical developments in electromagnetic theory

This section addresses the principles and concepts of the classical electromagnetic theory which are used in this thesis. The equivalence principle defines electromagnetic fields by replacing real sources with equivalent sources. The principle, also known as Huygen's principle, helps to explain the propagation, refraction and reflection of electromagnetic waves [Huy93], [Lia18].

In 1800s, Helmholtz described "polarization" as displacement of the charges in dielectric media. He showed that there were longitudinal waves of electric polarization. According to Helmholtz's theory, the propagation of perturbations in a dielectric medium must have different velocities for transversal and longitudinal waves [Cah93].

Maxwell's equations (1860-65) are a set of electrodynamic equations to describe all electromagnetic phenomena in nature. According to these equations, light is an electromagnetic wave. Hertz verified Maxwell's equations by his experiments. Many scientists including Edison, Thompson, Dolbear and Hughes studied electromagnetic waves [Max65], [SS03] but only Hertz could make the correlation with Maxwell's theory [SS03].

For scalar diffraction theory, integral formulas were formulated by Kirchhoff and Rayleigh [Heu73]. An exact solution for diffraction of a plane wave by a perfectly conducting infinitely thin half-plane was derived by Sommerfeld in 1896 [BW99]. The solution describes well diffraction at the apertures in plane screens [MM01].

In 1901, A. Love developed the concept of equivalent surface currents that behaves as Huygen's secondary sources [Lov01]. T. Young did a double-slit interference experiment for demonstrating the wave properties of light [Lia18], [You07]. Fresnel [Fre00] studied diffraction of light by using wave equations and boundary values. He combined the Huygen's principle and the interference principle. It became a mathematical basis for the analysis of light propagation.

Diffraction of electromagnetic waves was studied by Stratton and Chu [SC39], Richards and Wolf [RW59], Kottler [Kot23], [MM01].

The Stratton-Chu integral representation is a vectorial equivalent of the Fresnel-Kirchhoff diffraction integral which was based on the Kirchoff's integral formula [MM01]. Franz developed an integral model for the description of the field vectors in the interior of a source-free closed surface [Lah16].

1.4 Equivalent circuits and lumped elements

In metamaterial design, adjusting the dimensions of the particles, deciding the type of particles, positioning the particles and shaping the unit cells are the corner stones to modify the electromagnetic response. In engineering analysis of metamaterials, equivalent circuit models are often used. In this modeling, ideal simple circuit elements are utilized, namely resistors, capacitors, inductors, voltage or current sources. At RF and microwave frequencies, lumped elements are based on small parts of TEM lines shorter than the wavelength at the operational frequency [Bah03].

Because of the small sizes and fabrication process, the quality factor Q is not higher than that of a distributed circuits. On the other hand, lumped elements have lower costs and wider bandwidths. The rules of circuit theory, the transmission lines and the equivalent circuit lumped elements help to determine the electromagnetic behavior of the structure, for instance, reflection, transmission and absorption. The circuits can be modeled with simple shunt and series circuits to estimate the response. Increasing the complexity of the circuit is not preferred because it may cause unnecessary complications [MDP48].

Analytical methods, full-wave simulations and measurement-based methods are used to develop equivalent circuit models. The values of the lumped elements are extracted from DC resistance measurements and S—parameter data [Bah03].

1.5 Equivalent circuit approach for metasheets

Metasheets are two-dimensional metamaterials. The other two dimensions of the layer become much larger than the thickness. Because of this shape, an assumption about the field distribution, which is named **locally quasistatic**, can be made. The field distribution is assumed as uniform and waves travel along the layer but at every point of the field distribution over the thickness remains unchanged. This assumption gives a chance to use a transmission line approach to analyze the metasheets because the waves propagate along the axis of the transmission lines. The field distribution is assumed quasistatic in the directions which are orthogonal to the axis of the transmission line [Tre03].

A combination of transmission line and equivalent circuit approaches results in an efficient and adequate tool. Even if the number of thin layers increases, this tool can still work to analyze a multilayer metasheet. The time consumption of the analysis can be decreased compared to full-wave simulations [Cap09].

1.6 Importance of hybrid approaches

When two or many methods are mutually combined and used together, then this is called a hybrid method. For practical applications, analytical solutions can be inaccurate or too difficult. Therefore, approximate calculations can be performed by using numerical methods or asymptotic methods. In the framework of numerical methods, electromagnetic problems such as scattering and radiation are reduced to algebraic problems, which can be solved by using computers. For electrically large structures, asymptotic methods are preferred. If an electrically large structure includes electrically small particles, then hybrid methods combining numerical and asymptotic methods can be suitable. The application of numerical methods to electrically large structures requires powerful computers; otherwise, it can take a long time [Hag05]. To reduce the need for heavy numerical computations, analytical and numerical methods can be combined and used as a semianalytical or hybrid method.

1.7 Importance of lenses

Lenses are devices which focus or collimate propagating signals or transform incoming phase fronts into desired outgoing phase fronts. The design targets of a lens are a large bandwidth, decreasing the complexity of manufacturing, high gain, low cost, little weight. The shapes of lenses are decided according to the phase delays of waves propagating through the material of the lens. Well-known lenses are dielectric lenses and metal gratings. The phase delays happen because of the refraction in the dielectric lenses or because of diffraction or interferences when the lens has metal parts. The Fresnel zone plate is another kind of lens which can be used for focusing and imaging. Because of the flat design, a reduction in thickness, weight and absorption loss is possible [Hri00]. The negative sides of Fresnel zone plates are zone edge blockage and low efficiency [Rot84], [HH95].

For controlling the phases, lenses with concentric annular zones can be designed to be opaque (reflection), partially-opaque or transparent. The disadvantage of a partially-opaque lens is that it produces approximately the same bandwidth as a conventional lens of the same diameter. It does not increase the efficiency. F. Sobel studied the phase correcting zone plate for microwave and millimeter bands [Wil85]. Measurements were carried out at 140 and 210 GHz. Further studies were performed to improve the features of lenses, and lenses were designed for frequencies between 10 to 280 GHz. In phase correcting plates, a different dielectric material can be used for each zone. It can help to have different refraction because of the different

permittivity values of the material while keeping the thickness of the lens constant. It can be named “planar lens” [Wil85]. Lens studies were also conducted for antennas, which are referred to as microwave lens antennas [MPM95], [McG86]. There were also studies on metamaterial based gradient index lenses [ea06], [ea07a] and Luneburg lenses [KS10], [QHT09] for enabling ultrathin light-weight flat lenses for broadband operation [NIKS13], [ea12a]. In [LFHB14] [ea16a], dielectric metasurface lenses have been designed for higher focusing efficiency in transmission mode in the optical frequency range.

1.8 Motivation of the research

In microwave engineering, controlling or correcting the phase distribution, improving gain and broadening the bandwidth of the electromagnetic response of antennas play a significant role. There have been many studies to improve these features [HL16], [Sug18], [ARA17].

The first motivation reason is that antenna systems may comprise phased arrays which are utilized for a scanning performance in transmission and receiving. Direction finding (DF), scanning synthetic aperture radar (SAR) and similar applications mainly use such systems [MC10]. Every radome changes the phase of the signal which causes a loss in DF accuracy and SAR resolution [AMC94], [MC10]. The shape, the material, material composition (for example laminated or solid etc.) of the radome and varying incident angles cause phase shifts. The phase shift plays an important role in the evaluation of the performance of radomes, and this is an important topic in antenna engineering [NAM10]. In this study, a planar Fresnel lens is designed by using metasheets.

A further reason is that finding the suitable dimensions of a particle for the defined microwave application may take too long. It is therefore desirable to reduce the simulation time.

1.9 Objectives

The objectives of this thesis are to develop a semianalytical (hybrid) method to accelerate the design process for planar metasheets and to design a metasheet for compensating the phase distortion caused by a hemispheric radome in the Ka-band. The combination of metasheet and radome can be called "metaradome". The definition of the metaradome is given in Chapter 2. For the calculation of the electric field transmitted through electrically large metasheets, an approach combining homogenization of the metasheet with the PO method is developed. In order to keep

the mechanical complexity of the design as low as possible, simply shaped inclusions (metal rings) without any lumped elements and electronic components are used.

1.10 Outline of the thesis

In Chapter 2, general formulations about electromagnetics, information from literature about frequency selective surfaces, metamaterials, metasheets, arrays of circular inclusions, application areas of metamaterials and potential applications of metaradomes are given. In Chapter 3, modeling of metamaterials with finite element methods is explained, and the simulation results for the infinite periodic planar metasheets obtained by HFSS are presented. In Chapter 4, a semianalytical model, which is based on the equivalent circuit modeling for infinite planar circular rings, is explained. In Chapter 5, the PO method and its usage for electrically large finite-size metasheets are explained. A metalens design for a hemispheric radome in the Ka-band is described, and an experimental validation of the design is presented in Chapter 6.

Chapter 2

Metamaterials in Microwave Applications

2.1 General formulations

2.1.1 Maxwell's equations and plane waves

Maxwell's equations are [Col92]

$$\nabla \times \mathbf{E} = -\frac{\partial \mathbf{B}}{\partial t} \tag{2.1}$$

$$\nabla \times \mathbf{H} = \mathbf{J} + \frac{\partial \mathbf{D}}{\partial t} \tag{2.2}$$

$$\nabla \cdot \mathbf{D} = \rho \tag{2.3}$$

$$\nabla \cdot \mathbf{B} = 0. \tag{2.4}$$

where (2.1) is Faraday's law of induction. (2.2) is Ampère's law. (2.3) and (2.4) are Gauss laws for the electric and magnetic fields. The quantities **E** and **H** are the electric and magnetic field intensities (electric and magnetic vectors), respectively. The quantities **D** and **B** are the electric and magnetic flux densities (electric displacement, magnetic induction), respectively. ρ and **J** are the volume charge density and electric current density of any external charges (excluding induced polarization charges and currents) [Orfed]. Maxwell's equations in source-free regions

of space are therefore given by

$$\nabla \times \mathbf{E} = -\frac{\partial \mathbf{B}}{\partial t} \tag{2.5}$$

$$\nabla \times \mathbf{H} = \frac{\partial \mathbf{D}}{\partial t} \tag{2.6}$$

$$\nabla \cdot \mathbf{D} = 0 \tag{2.7}$$

$$\nabla \cdot \mathbf{B} = 0. \tag{2.8}$$

In vacuum, the relations between electric and magnetic flux densities **D**, **B** and field intensities **E**, **H** are described as

$$\mathbf{D} = \varepsilon_0 \mathbf{E} \tag{2.9}$$

$$\mathbf{B} = \mu_0 \mathbf{H}, \tag{2.10}$$

where ε_0 and μ_0 are permittivity and permeability in free space (vacuum). In homogeneous dielectric or magnetic materials, the relation between electric and magnetic flux densities **D**, **B** and field intensities **E**, **H** are described as [BW99]

$$\mathbf{D} = \varepsilon \mathbf{E} \tag{2.11}$$

$$\mathbf{B} = \mu \mathbf{H}, \tag{2.12}$$

where ε, μ are permittivity and permeability of the medium. The speed of light in vacuum is

$$c = \frac{1}{\sqrt{\varepsilon_0 \mu_0}}. \tag{2.13}$$

The intrinsic impedance of free space (vacuum) is defined as

$$Z_0 = \sqrt{\frac{\mu_0}{\varepsilon_0}}. \tag{2.14}$$

The impedance of a material in terms of the corresponding vacuum value is

$$Z = Z_0 \sqrt{\frac{\mu_r}{\varepsilon_r}}, \tag{2.15}$$

where μ_r and ε_r are relative permeability and relative permittivity. Maxwell's equations can be written for linear combinations of single frequency solutions [Orfed]

$$\mathbf{E}(\mathbf{r}, t) = \int_{-\infty}^{+\infty} \mathbf{E}(\mathbf{r}, \omega) e^{j\omega t} \frac{d\omega}{2\pi}, \tag{2.16}$$

where ω is angular frequency. Time-harmonic fields are expressed as

$$\mathbf{E}(\mathbf{r},t) = Re[\mathbf{E}(\mathbf{r})e^{j\omega t}] \tag{2.17}$$

$$\mathbf{H}(\mathbf{r},t) = Re[\mathbf{H}(\mathbf{r})e^{j\omega t}]. \tag{2.18}$$

where $\mathbf{E}(\mathbf{r})$ and $\mathbf{H}(\mathbf{r})$ are complex-valued. For traveling waves, fields should be real. When the time derivatives are replaced with $j\omega$, then Maxwell's equations in (2.1)- (2.4) can be written in the form [Col92]

$$\nabla \times \mathbf{E} = -j\omega\mathbf{B} \tag{2.19}$$

$$\nabla \times \mathbf{H} = \mathbf{J} + j\omega\mathbf{D} \tag{2.20}$$

$$\nabla \cdot \mathbf{D} = \rho \tag{2.21}$$

$$\nabla \cdot \mathbf{B} = 0. \tag{2.22}$$

The simplest electromagnetic waves are uniform plane waves, which propagate along a fixed direction. It is assumed that it is the z direction in a lossless medium. Uniformity means that the fields are functions of z and t as $\mathbf{E}(z,t)$, $\mathbf{H}(z,t)$. Then, the gradient, divergence, and curl operations simplify to [Orfed]

$$\nabla = \hat{\mathbf{z}}\frac{\partial}{\partial z} \tag{2.23}$$

$$\nabla \cdot \mathbf{E} = \frac{\partial E_z}{\partial z} \tag{2.24}$$

$$\nabla \times \mathbf{E} = \hat{\mathbf{z}} \times \frac{\partial \mathbf{E}}{\partial z}. \tag{2.25}$$

According to equations in (2.11) and (2.12) , the source-free Maxwell's equations become

$$\hat{\mathbf{z}} \times \frac{\partial \mathbf{E}}{\partial z} = -\mu\frac{\partial \mathbf{H}}{\partial t} \tag{2.26}$$

$$\hat{\mathbf{z}} \times \frac{\partial \mathbf{H}}{\partial z} = \varepsilon\frac{\partial \mathbf{E}}{\partial t} \tag{2.27}$$

$$\frac{\partial E_z}{\partial z} = 0 \tag{2.28}$$

$$\frac{\partial H_z}{\partial z} = 0. \tag{2.29}$$

Equations (2.26) and (2.27) can be written in an equivalent form:

$$\hat{\mathbf{z}}\times\frac{\partial\mathbf{E}}{\partial z}=-\frac{1}{c_m}Z\frac{\partial\mathbf{H}}{\partial t} \tag{2.30}$$

$$Z\hat{\mathbf{z}}\times\frac{\partial\mathbf{H}}{\partial z}=\frac{1}{c_m}\frac{\partial\mathbf{E}}{\partial t}, \tag{2.31}$$

where $c_m=\frac{1}{\sqrt{\varepsilon\mu}}$, and (2.30) and (2.31) can be expressed as

$$\frac{\partial\mathbf{E}}{\partial z}=-\frac{1}{c_m}\frac{\partial(Z\mathbf{H}\times\hat{\mathbf{z}})}{\partial t} \tag{2.32}$$

$$\frac{\partial(Z\mathbf{H}\times\hat{\mathbf{z}})}{\partial z}=-\frac{1}{c_m}\frac{\partial\mathbf{E}}{\partial t}. \tag{2.33}$$

Equations (2.32) and (2.33) can be written in terms of forward and backward fields ($\mathbf{E}_+(z,t)$, $\mathbf{E}_-(z,t)$) [Orfed]

$$\frac{\partial\mathbf{E}_+}{\partial z}=-\frac{1}{c_m}\frac{\partial\mathbf{E}_+}{\partial t} \tag{2.34}$$

$$\frac{\partial\mathbf{E}_-}{\partial z}=\frac{1}{c_m}\frac{\partial\mathbf{E}_-}{\partial t}. \tag{2.35}$$

Harmonic time-dependent waves should be real as

$$\mathbf{E}(z,t)=Re[\mathbf{E}(z)e^{j\omega t}] \tag{2.36}$$

$$\mathbf{H}(z,t)=Re[\mathbf{H}(z)e^{j\omega t}], \tag{2.37}$$

where $\mathbf{E}(z)$ and $\mathbf{H}(z)$ are transverse to z direction. For time-periodic fields, equations (2.34) and (2.35) convert into the first-order differential equations

$$\frac{\partial\mathbf{E}_\pm(z)}{\partial z}=\mp jk\mathbf{E}_\pm(z), \tag{2.38}$$

where $k=\omega\sqrt{\varepsilon\mu}$, with the solutions for the forward and backward fields

$$\mathbf{E}_+(z)=\mathbf{E}_{0+}e^{-jkz} \tag{2.39}$$

$$\mathbf{E}_-(z)=\mathbf{E}_{0-}e^{jkz}, \tag{2.40}$$

where $\mathbf{E}_\pm$ are arbitrary constant vectors such that $\hat{\mathbf{z}}\cdot\mathbf{E}_\pm=0$. The general solution of a single-frequency wave can be expressed as

$$\mathbf{E}(z)=\mathbf{E}_{0+}e^{-jkz}+\mathbf{E}_{0-}e^{jkz} \tag{2.41}$$

$$\mathbf{H}(z)=\frac{1}{Z}\hat{\mathbf{z}}\times(\mathbf{E}_{0+}e^{-jkz}-\mathbf{E}_{0-}e^{jkz}). \tag{2.42}$$

In this study, $e^{j\omega t}$ is suppressed. If the propagation medium is free space (vacuum), the parameters ε_0, μ_0, Z_0, c are used. The free-space wavelength and corresponding wavenumber k_0 are given by [Orfed]

$$\lambda_0 = \frac{2\pi}{k_0} = \frac{c}{f} \tag{2.43}$$

$$k_0 = \frac{\omega}{c}, \tag{2.44}$$

where $\omega = 2\pi f$. For a lossy dielectric substrate, the relative permittivity of the substrate and the loss tangent are described by [Col92]

$$\begin{aligned} \varepsilon_r &= \varepsilon_r' - j\varepsilon_r'' \\ \tan(\delta) &= \frac{\varepsilon_r''}{\varepsilon_r'}. \end{aligned} \tag{2.45}$$

For small losses such as $\varepsilon_r'' \ll \varepsilon_r'$, the wavenumber is

$$jk = \alpha + j\beta = j\sqrt{\varepsilon_r'}k_0 + \frac{k_0\varepsilon_r''}{2\sqrt{\varepsilon_r'}} \tag{2.46}$$

where α is the attenuation constant and β is the phase constant. The waves attenuate according to $e^{-\alpha z}$ while propagating in the $+z$ direction [Col92].

2.1.2 Transmission and reflection coefficients

According to boundary conditions at a planar interface separating two dielectric media with characteristic impedances Z_1 of medium 1 and Z_2 of medium 2 (Fig. 2.1), the total electric (E) and magnetic (H) fields are continuous across the interface as

$$E^1 = E^2 \tag{2.47}$$

$$E^1 = H^2 \tag{2.48}$$

The total electric field can be written in terms of forward and backward electric fields (E_+, E_-) as

$$E = E_+ + E_- \tag{2.49}$$

Reflection and transmission coefficients at the interface are shown as q and τ respectively. The relation between fields and the reflection, transmission coefficients are expressed as [Orfed]

$$\begin{bmatrix} E_+^1 \\ E_-^1 \end{bmatrix} = \frac{1}{\tau}\begin{bmatrix} 1 & q \\ q & 1 \end{bmatrix}\begin{bmatrix} E_+^2 \\ E_-^2 \end{bmatrix}$$

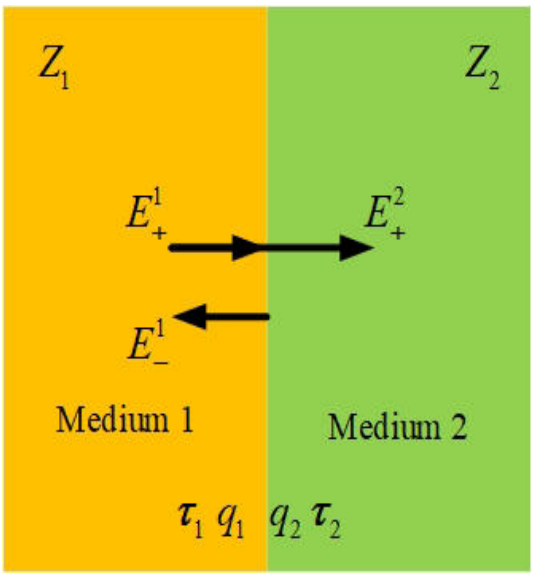

Figure 2.1 The interface between two dielectric media

where $E_-^2 = 0$. The reflection and transmission coefficients are defined in terms of characteristic impedances as [Som06], [Col92]

$$q = \frac{Z_2 - Z_1}{Z_2 + Z_1} \tag{2.50}$$

and

$$\tau = \frac{2Z_2}{Z_2 + Z_1}. \tag{2.51}$$

The relationship between reflection and transmission coefficient is [Col92]

$$\tau = 1 + q. \tag{2.52}$$

In a two-interface problem, a dielectric slab Z_d separates the semi-infinite media Z_1 and Z_2 as in Fig. 2.2. For describing the complete transmission response from medium 1 into medium 2 in Fig. 2.2, the transmission coefficient is defined by

$$T = \frac{E_+^2}{E_+^1}. \tag{2.53}$$

The relation between fields E_+^2 and E_+^1 can be described in terms of fields in the dielectric slab E_{d+}^1, E_{d-}^1, E_{d+}^2, E_{d-}^2 and internal reflection and transmission coefficients (q_1, q_2, τ_1, τ_2) at two interfaces as shown in Fig. 2.2 [Orfed]. E_-^2 is assumed zero. The relation between E_{d+}^2, E_{d-}^2 and E_+^2 is

$$\begin{bmatrix} E_{d+}^2 \\ E_{d-}^2 \end{bmatrix} = \frac{1}{\tau_2} \begin{bmatrix} 1 & q_2 \\ q_2 & 1 \end{bmatrix} \begin{bmatrix} E_+^2 \\ 0 \end{bmatrix}. \tag{2.54}$$

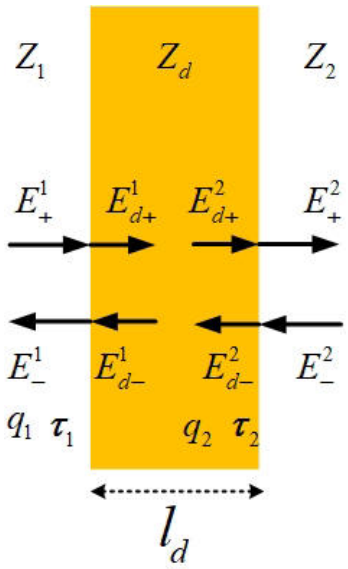

Figure 2.2 The dielectric slab between two semi-infinite mediums

The relation between E_+^1, E_-^1 and E_{d+}^2, E_{d-}^2 is described as

$$\begin{bmatrix} E_+^1 \\ E_-^1 \end{bmatrix} = \frac{1}{\tau_1}\begin{bmatrix} 1 & q_1 \\ q_1 & 1 \end{bmatrix}\begin{bmatrix} E_{d+}^1 \\ E_{d-}^1 \end{bmatrix} = \frac{1}{\tau_1}\begin{bmatrix} 1 & q_1 \\ q_1 & 1 \end{bmatrix}\begin{bmatrix} e^{jkl_d} & 0 \\ 0 & e^{-jkl_d} \end{bmatrix}\begin{bmatrix} E_{d+}^2 \\ E_{d-}^2 \end{bmatrix}. \tag{2.55}$$

Inserting (2.54) in (2.55) gives [Orfed]

$$\begin{bmatrix} E_+^1 \\ E_-^1 \end{bmatrix} = \frac{1}{\tau_1}\begin{bmatrix} 1 & q_1 \\ q_1 & 1 \end{bmatrix}\begin{bmatrix} e^{jkl_d} & 0 \\ 0 & e^{-jkl_d} \end{bmatrix}\frac{1}{\tau_2}\begin{bmatrix} 1 & q_2 \\ q_2 & 1 \end{bmatrix}\begin{bmatrix} E_+^2 \\ 0 \end{bmatrix}. \tag{2.56}$$

After multiplying the matrix factors, the transmission response can be obtained as

$$T = \frac{\tau_1\tau_2 e^{-jkl_d}}{1+q_1q_2e^{-j2kl_d}}. \tag{2.57}$$

Inserting (2.52) in (2.57) results in

$$T = \frac{(q_1+1)(q_2+1)e^{-jkl_d}}{1+q_1q_2e^{-j2kl_d}}. \tag{2.58}$$

2.1.3 Planar slot arrays

Babinet's principle is an important and useful principle in electromagnetic theory. This principle is based on the duality feature of the electromagnetic field. When a plane wave is incident, incident wave in a complementary situation can be defined as the clockwise rotation of the plane of polarization through 90° around the direction of propagation [OT17].

In the complementary waves, the roles of electric field vector (**E**) and magnetic field vector (**H**) are interchanged. Boundary conditions must be fulfilled, and this can be done by replacing all electric walls with magnetic walls and vice versa. Both incident and complementary incident fields satisfy Maxwell's equations in free space [BSU69], [Bal05], [Boo46], [ea07b]. The relations between the field and the complementary field in the same medium, are described by the equations [Cha88]

$$\mathbf{H}_B = \pm\sqrt{\frac{\epsilon}{\mu}}\mathbf{E}_A, \tag{2.59}$$

$$\mathbf{E}_B = \mp\sqrt{\frac{\mu}{\epsilon}}\mathbf{H}_A. \tag{2.60}$$

Conducting strip and slot resonators are the physical realizations of the complementary resonators (Fig. 2.3) [Naq16], [KO60]. These resonators are used in antenna design.

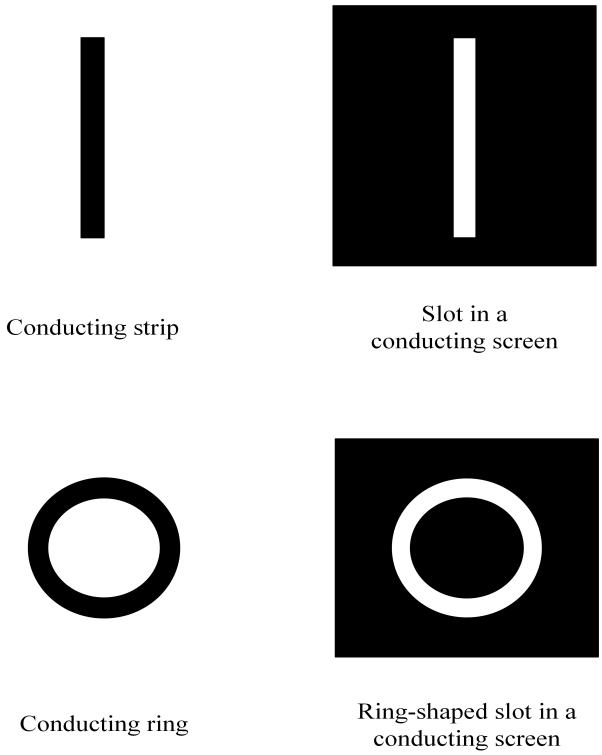

Figure 2.3 Conducting strip, ring and slot resonators

The consequence is that a slot antenna has the same radiation pattern as a dipole antenna with the electric and magnetic planes interchanged. In this study, the circular rings and circular slots are studied, and according to this principle, the amplitude of the transmission coefficient of planar arrays of circular slots is identical with the amplitude of the reflection coefficient for planar arrays of circular rings in free space. The resonance frequencies become also interchangeable.

2.1.4 Equivalent surface currents and Green's function

In this section, the equivalent surface currents and Green's functions are explained. For understanding the PO method in Chapter 5, the equivalent currents on the surface should be analyzed. In Fig. 2.4, the region A represents a volume with sources, and region B is a source-free region. In the source-free region, the observation point is positioned. The fields in the region B are $\mathbf{E}_t, \mathbf{H}_t$. In region A, the field of the sources and the reflected field from the boundary S are $\mathbf{E}_i, \mathbf{H}_i$ and $\mathbf{E}_r, \mathbf{H}_r$, respectively. The surface S is the boundary between these two regions (region A and region B), and the unit normal vector is directed into the region where the observation point is located [Cha88].

The tangential components of electric and magnetic fields are continuous on the surface. The reflected field is the field reflected at the boundary S. The transmitted field is the field refracted through the boundary S. If the conductivity σ, permittivity ε and permeability μ of both regions are the same, then the complete region becomes homogeneous and the original sources and the observation point are positioned in the same medium. When there is no reflection, only the transmitted field forms the field in region B. The equivalence theorem states that instead of using the original sources to calculate the scattered field in region B, the distribution of surface electric and magnetic currents can be used [Col60].

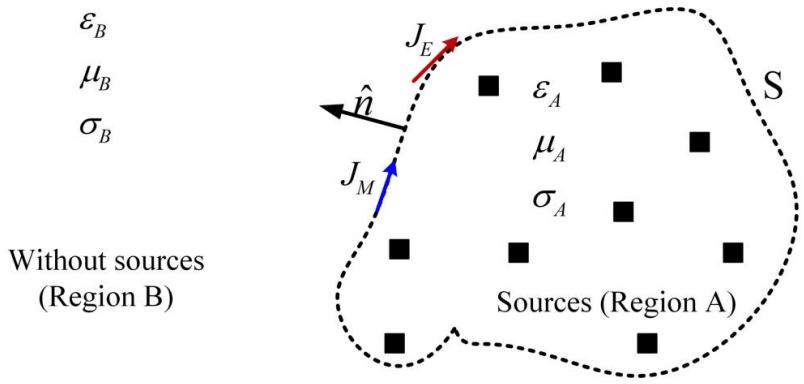

Figure 2.4 Surface enclosing the field sources (Squares symbolize the sources).

The reflected and transmitted fields should satisfy the homogeneous form of Maxwell's equations as [Cha88], [Som06], [Uma89]

$$\nabla \times \mathbf{E}_r = -j\omega\mu_A \mathbf{H}_r \tag{2.61}$$

$$\nabla \times \mathbf{H}_r = (\sigma_A + j\omega\epsilon_A)\mathbf{E}_r \tag{2.62}$$

$$\nabla \times \mathbf{E}_t = -j\omega\mu_B \mathbf{H}_t \tag{2.63}$$

$$\nabla \times \mathbf{H}_t = (\sigma_B + j\omega\epsilon_B)\mathbf{E}_t. \tag{2.64}$$

At the boundary surface S, the tangential components of $\mathbf{E}$ and $\mathbf{H}$ are continuous. Thus

$$E_i^t + E_r^t = E_t^t \tag{2.65}$$

$$H_i^t + H_r^t = H_t^t. \tag{2.66}$$

The tangential components ($\mathbf{E}^t$, $\mathbf{H}^t$) of $\mathbf{E}$,$\mathbf{H}$ on S relate to the surface current densities $\mathbf{J}_E$ and $\mathbf{J}_M$ according to

$$\mathbf{J}_E = \hat{n} \times \mathbf{H}_t^t = \hat{n} \times (\mathbf{H}_i^t + \mathbf{H}_r^t) \tag{2.67}$$

$$\mathbf{J}_M = -\hat{n} \times \mathbf{E}_t^t = -\hat{n} \times (\mathbf{E}_i^t + \mathbf{E}_r^t). \tag{2.68}$$

These currents completely define the fields in region B [Col60]. They are called equivalent surface currents. To solve electromagnetic radiation problems uniquely, a specific boundary condition is to be applied on the fields at infinity.

The Green's function is the response to a point source. Consider the solution of the scalar Helmholtz equation in a homogeneous medium [Cha88], [Broed]

$$\nabla^2 G(r) + k^2 G(r) = -\delta(r). \tag{2.69}$$

The scalar Green's function is a solution of (2.69). For simplification, the position of a source is at the origin. Available solutions of (2.69) are

$$G_1 = \frac{e^{-jkr}}{4\pi r} \tag{2.70}$$

and

$$G_2 = \frac{e^{+jkr}}{4\pi r}, \tag{2.71}$$

where r is the distance between the observation point and the source point. If the medium is vacuum, then k is replaced by k_0. The solution (2.70) describes an outgoing wave and is used in integral formulas to describe scattered and radiated fields. The factor $\frac{1}{4\pi}$ is found by integrating (2.69) over a sphere of infinitesimal radius centered at the origin. To write the Green's function for a general case, the distance r becomes $|\mathbf{r}-\mathbf{r_1}|$ which is the distance between the observation point and the source point [Kon86].

2.2 Frequency selective surfaces

A periodic array of metal resonators or small apertures in a metal surface behaves like an electromagnetic filter when it is illuminated by an electromagnetic wave. This is named a "frequency selective surface" (FSS). Being a filter means that the structure shows a stopband and/or bandpass behavior at a desired frequency or a frequency range [Mun00].

FSS structures can be classified into infinite periodic, cascaded, multilayered, finite periodic and electrically large, planar or curved [NJ15], [Ton17]. Different types of inclusions such as rings, patches, square loops, strips and slots are used to design FSS layers. The inclusions with fractal geometries are used to provide a multiband operation [BRAJ06]. Methods like perturbation methods or genetic algorithms are used, and different design models such as multi-resonant unit-cells, multi-element unit-cells, composite unit-cells, complementary structures are utilized to design FSS layers [MB10], [Ton17].

Frequency selective surfaces are used in different applications, including noise reduction, RF interference, beam-forming, reconfiguration of antenna radiation patterns for better communication, in the defense area [HCWC15], [CM12].

There are many important studies about FSS and some of them are mentioned in this section. With the help of a FSS, a radome can be designed as a spatial filter to permit transmission at the operating frequency and reflect the out-of-band waves to other directions [ea12b], [CHD09]. A frequency selective radome can be designed as a resistive or metal FSS, for example by using compact interdigitated Jerusalem crosses to behave as a pass band filter within a defined frequency band and as an absorber above the transmission band [CM12]. In [LPC+17], an active FSS which is controlled by a PIN diode positioned between a cross-shaped loop and an inductive stub on the surface, is designed. The operating frequencies are either the C or the X band. A flexible printed circuit board is preferred to adjust the curved and flat structures easily and properly. The goal of an active FSS is to make the design light and mechanically strong or to include the effect of real environments. More research and studies are needed about multidimensional shapes and composite materials.

2.3 Metamaterials

From the 1960's, the interest in metamaterials started to increase in the scientific and engineering community. In 1967, Veselago showed that left-handed materials can support electromagnetic

waves with phase and group velocities pointing in opposite directions [Ves68]. Another well-known contribution to the development of metamaterials is the first ever realization of a negative-index material (NIM) as an array of copper strips and split ring resonators on printed circuit boards [Die13].

The word "metamaterial" is a combination of "meta" and "material". The greek word "meta" means something beyond, something higher level [Sih09], [GPG14]. The properties of metamaterials come out on the macroscopic level by combining different components at microscopic level. Properties of metamaterials can also be extraordinary, which are not observed in the elemental materials and in nature [Sih07]. The choice of the periodicity, dimensions and positions of inclusions let a metamaterial give different responses to the excitations, since effective permittivity and permeability are affected. The key point is that the unit cells and the inclusions should be smaller than the operational wavelength of the incident wave [Wal01].

The LC circuit, where L is inductance and C is capacitance of a resonator, can be considered for defining the resonance property of a metamaterial, because electrically small resonators are used to design metamaterials. By using electrically small resonators, a metamaterial should be homogenized similar to natural materials [Sih07].

The inclusions can be metal conductive or nonmetal conductive materials. For instance, conductive graphene, aluminum zinc oxide and indium tin oxide are nonmetal conductive materials. Silver, gold, aluminum, zinc, copper, gold alloys, aluminum alloys and zinc alloys are metal conductive materials. Ceramic, ferroelectric, ferrite, polymer material such as FR4, fiber-reinforced resin composite and fiber reinforced ceramic matrix composite can be used as the material of the inclusions [RLJ17]. Metamaterials can be adjusted on a flexible substrate such as polymide, polyester, polytetrafluoroethylene, polyurethane, polyarylate, PET film and PVC film. The flexible substrate can be mainly useful to design metamaterials for curved surfaces such as radome walls. Such designs can be helpful for antennas and radomes in microwave applications [RLJ17]. The equivalent circuit is a well known approach to design metamaterials. Commercial software including the finite integration technique-based CST Microwave Studio and the FEM solver of ANSOFT HFSS are mainly used for full-wave electromagnetic simulations of metamaterials [Cap09].

When a metamaterial is applied to a product, it may be disposed according to the shape of the specific product so that the metamaterials let the product fit. The metamaterial itself can constitute a main part of the product. When a metamaterial is used for making a radome, it can be utilized as the main body of the radome, or a metamaterial is disposed on the surface

of the radome body made by a conventional ordinary material to enhance its electromagnetic performance [RLJ17].

In the metamaterial design, differently shaped particles are used depending on the type of application. The electrically small inclusions can have different shapes such as diamond, snowflake, I shape, hexagonal, hexagon ring, cross-slotted shape, cross shape, Y-hole, Y shape, a round-hole shape, an annular shape, square ring, circular ring, square disc, circular disc, square split ring resonator (SRR), circular SRR and plus shape [RLJ17], [Mun00]. Some known shapes of resonators are shown in Fig. 2.5.

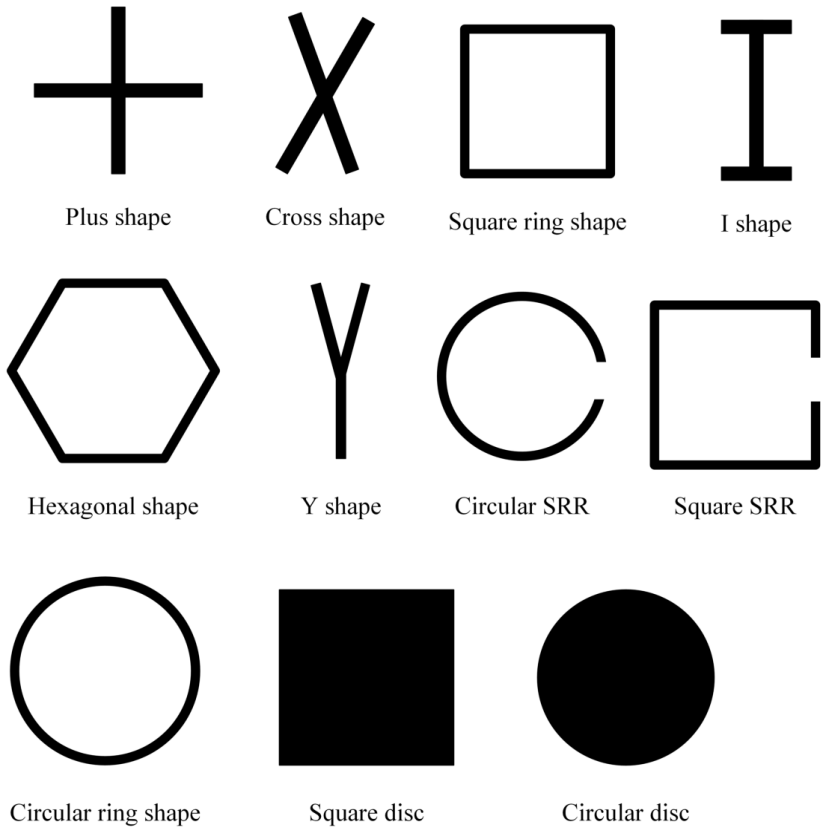

Figure 2.5 Some known shapes of the resonators in metamaterials.

2.4 Types of metamaterials

Electromagnetic metamaterials are classified into several categories such as double negative, single negative, electromagnetic bandgap, double positive, bi-isotropic, bi-anisotropic and chiral. These metamaterials can enhance the electromagnetic performance of beam steerers, modulators, band-pass filters, lenses, microwave couplers and antenna radomes in optical and microwave applications [KA18], [MK11]. Further types of metamaterials are as follows:

Chiral metamaterials are constructed from chiral elements [MK11].

Terahertz metamaterials act at terahertz frequencies. The terahertz frequency range is defined from 0.1 to 10 THz [KA18], [Par18].

Photonic metamaterials are artificially designed subwavelength periodic structures to react at optical frequencies. The sub-wavelength periodicity differentiates the photonic metamaterial from photonic band gap structures [Par18].

Nonlinear metamaterials may also be produced from nonlinear components. They have properties which change with the power of the incident wave. Such metamaterials can show magnetic, electric and magnetoelectric nonlinear reactions [Sha15].

Tunable metamaterials can tune the transmitted, reflected, or absorbed electromagnetic (EM) wave through the structure [KA18]. Tunable metamaterial gives the opportunity to control and change the electromagnetic responses such as transmission, reflection and absorption. Thus, the metamaterial becomes alterable and adaptable by permitting change of its structural components to adjust its macroscopic properties to the desired application [KA18], [Sih07], [zOE17a]. The example applications can be tunable phase shifters, filters, antennas and nonlinear components [CWR+06], [SMK06], [HPH+07], [ZHW+12]. There are different ways to make the metamaterial tunable. Permittivity and permeability can be tuned electrically, magnetically, seperately or simultaneously [AGK15], [SV07]. The change of geometry, size and position of inclusions, type of substrate or inclusion [TBM+14] is a well-known way. Another approach [zOE17a] is the use of active lumped elements such as voltage-controlled capacitors [zAB+07], varactors [HPS10], pin diodes [SCC+10], [PSK05], micro-electro-mechanical systems (MEMS) [DPC14], [BMea11] and non-Foster active elements. The resistance is affected by pin diodes. The resonance frequency can be controlled by voltage-controlled capacitors. The refractive index of a liquid crystal substrate can be tuned by applying a bias electric field because the positions of molecules are affected [SCP13], [ZKD+07].

The combination of FSS structures with liquid crystals can shift the frequency upon application of a bias voltage [ea13], [zOE17a]. Using ferrites helps also to make metamateri-

als tunable. When a magnetic bias is applied to a ferrite, the effective negative permeability can be changed. The structure can be tuned by controlling the applied magnetic bias. With this approach, tunability can be achieved in a broad frequency range [ZHW+12]. Tunable metamaterials can be used for radome walls to enhance the properties of an antenna covered by the radome [zOE17a].

2.5 Metasheets

A metasheet can be seen as a two-dimensional model of a metamaterial. A metasheet can achieve unusual and worthwhile electromagnetic properties. The thickness of the structure is small enough to be negligible with respect to the operational wavelength of the surrounding medium. The periodicity of the inclusions in a metasheet is small compared to the wavelength. A metasheet can be considered as homogeneous on the wavelength scale; therefore, it can be described by effective averaged surface properties. Because of being homogeneous, it does not produce any diffraction lobes as diffraction gratings do [Tre15]. The key difference between metasheets and FSSs is the size of the unit cells. In metasheets, the size is smaller than the wavelength, so no grating lobes occur. In an FSS, the size is comparable or greater than the wavelength, so there are grating lobes. The thickness of the resonators can be also negligible compared to the free-space wavelength. In the microwave region, even very thin metal inclusions can be considered as perfect electric conductors, since the skin depth is extremely small.

2.6 Applications and realizations of metamaterials

The properties of metamaterials can be unusual; therefore, metamaterials are promising for various types of applications. Metamaterials can be used effectively in antenna design, filter design and polarization converters to fulfill different requirements. Metamaterials can shape transmission, absorption, beam forming, directivity pattern, absorption, beam divergence, polarization conversion, beam deflection and beam convergence [RLJ17].

Negative-index materials (NIM), which are also referred to as left-handed materials, can be used as a superlens to have a high-resolution optical image [Pen00]. It creates an opportunity to be utilized in medical and optical imaging. Additionally, left-handed transmission lines or composite right/left-handed transmission lines can be useful in microwave and antenna applications. Another type of metamaterials is gradient refractive index metamaterials which can be utilized for beam-bending lenses and beam focusing lenses [CSL09].

In antenna design, metamaterials can help to improve the radiation properties such as directivity enhancement with a zero-index metamaterial for flat horn antennas, gain enhancement and reduction of the return loss of a patch antenna [GPG14]. Using metamaterials can help to reduce the size of an antenna. Metamaterials can help to achieve multiband operation and reconfigurability of microwave instruments.

Metamaterial structures can be used as cloaks. The generated electric and magnetic fields are blocked by an object or the electromagnetic wave is guided around the object. Coordinate transformation techniques are used to design cloaks [GPG14].

Metamaterials can be used for increasing the sensitivity and resolution of a sensor. Metamaterial sensors can play an important role in agricultural and biomedical applications [GPG14], [KRCB12]. Split ring resonators (SRRs) in a nested architecture are developed to increase the sensitivity in strain sensors, which are used in biomedical applications [ea10]. Resonant-type metamaterials, split ring resonators and spiral resonators can be used to design sensors for mapping soil humidity in agriculture application [KRCB12].

Some other interesting engineering applications of microwave metamaterials are in particular a broadband and reduced-loss 3D transformation optics lens for wide-angle scanning, a 3D planar gradient index lens for increasing the gain in the radiation and a random metasurface with reduced radar cross section (RCS) [Cui17].

For the industrialization of metamaterials, mass production should be developed. The connection between fundamental research in universities/ research institutes and companies for industrial implementations should be improved. For example, the center of the Kuang-Chi Research Institute of Advanced Technology has developed its own industrialization architecture. Under this architecture, real demands are introduced from the market and clients, and filtered based on specific criteria [LJZZ15]. Metamaterials can be used together with different technologies such as fibre, silicon photonic, laser and photovoltaic technologies [TUZ17].

2.7 Concept of metaradomes

The surface of radomes can be designed by using metasheets. As mentioned in Section 2.5, a **metasheet**, which is a quasi-two-dimensional version of a metamaterial, can be widely used in microwave systems such as antennas and radomes. The standard dielectric material of the radome wall can be replaced with the metasheet, or a metasheet can be inserted into the radome as an additional part. These two design models create a **metaradome**.

Metaradomes can be designed and developed for different application areas:

1. Maritime
2. Telecommunication
3. Radar
4. Aerospace
5. Automative.

Metaradomes can be a part of directional antennas, which are used in wireless networks to shape the directivity of the antennas. They can be designed for reconfigurable antennas to be used in another interesting application such a cognitive radio [PYQG15], [TC09], [PG13], which finds automatically available channels in a frequency spectrum, and its transmission or reception parameters are changed for having an optimum communication bandwidth within a determined spectral zone. A reconfigurable wireless system can be modified by depending on networks and user's choice [BKGA11]. With the help of metamaterials, radomes may attain new electrical properties such as tailored transmission, absorption and reflection behaviors. Metamaterials bring the benefits of correction of phase distortions, reduction of transmission losses and shaping the frequency dependence of the electromagnetic response. A metasheet can convert a radome into a multiband radome with reconfigurable frequency pass and stop bands, enhanced out-of-band rejection, on/off modes and also increasing the antenna gain. Available metaradome studies are overviewed in [zOE17a]. The most important directions of research related to metasheets in the radome applications are as follows [zOE17a]:

1. The bandwidth of transparent structures should be extended. Because of the resonance nature of the metamaterial inclusions, the bandwidth is limited. Wide and narrow bandwidths can be used in different application areas. Therefore, having a narrow bandwidth is not unfavorable for some specific applications such as cost-effective wireless networking for large outdoor scenes like seaports and rail yards [Teced].

2. Simulation of electrically large and curved radomes is a complicated calculation problem. For having a homogeneous surface, the size of the inclusions, which are distributed over an electrically large structure, should be as small as possible compared to the operational wavelength. This large amount of small particles is distributed over a finitely sized area, implying that the assumption of periodicity is not applicable; therefore, simulation of curved metasheets can be a future research field [zOE17b].

2.8 Studies on different circular inclusions

In this section, different types of circular inclusions, whose dimensions are smaller than the operational wavelength, are addressed. The basic types of the associated arrays are as follows:

1. Dense arrays of circular holes in a perfectly conducting sheet (screen) which are named "holey metasurfaces" (holey MTS). Such arrays can be used to realize partially reflective surfaces (PRS), which initiate leaky wave and beam forming, when positioned in front of a patch antenna or any other radiator. The gain and bandwidth are influenced by reflection from the PRS and the distance from the radiator. Moreover, depending on the character and appearance of structure, they can be used as back reflector [BBM+16].

2. Array of particles positioned on a dielectric substrate, which are backed by an electrically thin metal layer to shape the electromagnetic response and improve the efficiency and gain. A subclass of such arrays is referred to as "high-impedance surfaces" (HIS) which reflect electromagnetic waves with zero phase shift around the resonance frequency. It can decrease the thickness of an antenna system. Because of having subwavelength periodicity, the quasi-static regime can be considered. Electrically small circular patches can be used as particles [BBM+16].

Other studied ring configurations are the conventional split ring resonator (SRR), broadside coupled split ring resonator (BC-SRR), non-bianisotropic split ring resonator (NB-SRR) and double slit split ring resonator (DS-SRR) [MH13], [DSNP+12], [BM12], [CR12].

2.9 Planar array of circular rings

The main difficulty in the estimation of the electromagnetic response of metamaterial arrays of circular rings such as transmission or reflection is the complicated spectral and spatial structure of the induced currents on the subwavelength scale. The distance between the rings changes because of the rounded shape of the inclusion (Fig. 2.6), which results in field variations. A simplification is that the distance between the inclusions is smaller than the operating wavelength; therefore, the field which illuminates the unit cells, can be considered as quasi-static field [BBM+16].

The equivalent transmission line model of free-space propagation is used to estimate the electromagnetic response of the array of circular rings. An **effective width** (w_{eff}) description helps to account for the changeable distance between the inclusions. This effective width is

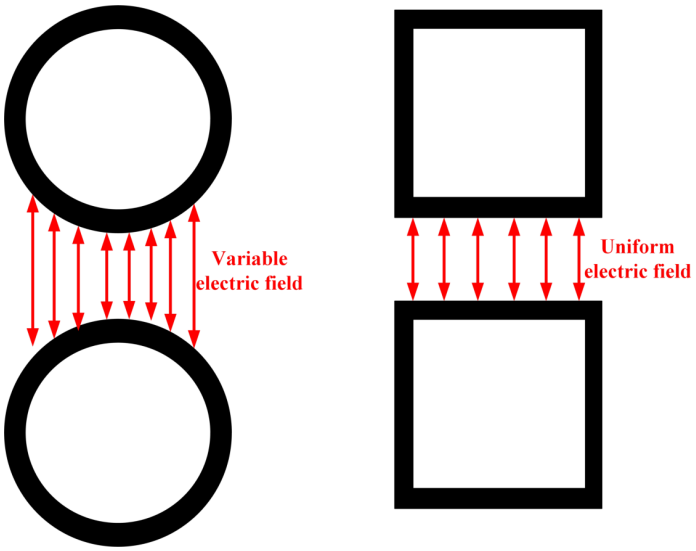

Figure 2.6 Electric field lines between two metal rings for plane-wave excitation.

calculated by the integral mean value theorem, so the inclusions are modeled as an equivalent array of sub-wavelength squared holes [BBM+16]. Another approach is a polarizability based analysis. The assumption that the inclusions are electrically small, helps to express their contributions in terms of electric dipoles but information cannot be provided about the geometry of the inclusion itself [BBM+16]. The polarizabilities of the inclusions are defined in terms of their dimensions for a single inclusion, not for a periodic array of inclusions [OT17], [Tre03].

Chapter 3

Modelling Infinite Planar Metasheets

3.1 High-frequency structure simulator (HFSS)

Full-wave simulators are used for different varieties of high-frequency electronic products. Some of the products are antennas, antenna arrays, RF or microwave components, high-speed interconnects, filters, connectors, integrated circuit (IC) packages and printed circuit boards. The High-Frequency Structure Simulator (Ansys HFSS) is an electromagnetic simulation software. Ansys HFSS is utilized to design high-frequency, high-speed electronics found in communication systems, radar systems, advanced driver assistance systems (ADAS), satellites, internet-of-things (IoT) product, and other high-speed RF and digital devices [Anyed]. HFSS uses the Finite Element Method (FEM) to solve Maxwell's equations [Dined].

3.2 Differential equation solvers

Examples of differential equation solving methods are the finite-difference time-domain (FDTD), finite element (FEM) and transmission-line matrix (TLM) methods [ST]. Differential equation solvers are used for both frequency and time-domain calculations. Such solvers can be useful to solve driven problems and eigenvalue problems. For differential equation solvers in frequency domain, iterative solvers are often used (especially in three dimensions). The closed-form and infinite-series analytical solutions are widely used for simpler problems. FEM plays a key role in analyzing complex metamaterials. The performance of computational electromagnetic tools and computers has been constantly improved. A lot of efforts have been invested in developments of algorithms [BIR08], [Rao05].

3.3 Comparison of electromagnetic modeling techniques

Method of Moments (MOM), FEM and the finite difference (FD) method are well-known algorithms and further studies are done on electromagnetic modeling [EH96], [Eib04]. FD uses the field components, or the potentials, on a structured grid of points to discretize Maxwell's equations. FD and FDTD are efficient algorithms because they need a small number of operations per grid point. For having a good approximation of complex boundaries, FEM can be preferred because it divides the computational region into subdomains. This is named as "discretization or meshing". A disadvantage of FEM is that calculations in time domain are slow. FEM is mainly used for eddy current calculations and time harmonic problems. FEM requires many computer resources in terms of CPU [BIR08], [Die13], [Rao05].

Integral equations are the ways to solve Maxwell's equations with the method of moments. Currents or charges on the surface of dielectrics and conductors are the unknowns in MOM [DeLed]. This method is suitable for scattering and radiation problems involving open regions, metal bodies and small current-carrying surfaces [DeLed], [BIR08].

3.4 Finite Element Method (FEM)

FEM is a well-known method to solve boundary-value problems of partial differential equations. Richard Courant published this method in 1943, to solve elasticity and structural problems [Die13]. FEM is based on meshing. The body is meshed into subregions using trapezodial, tetrahedral, or other types of meshing schemes. For having a better approximation, the size of the subdomains should be as small as possible. To determine the fields, a linear system of equations is solved. A finite number of basis functions is used to approximate the solution. The basis functions are mainly low-order polynomials, which are nonzero only in a few adjacent subregions [BIR08]. Many well-developed finite element simulation programs can subdivide arbitrarily shaped lines, surfaces, and volumes into the corresponding elements [BIR08], [Rao05].

3.5 HFSS simulation setup for infinite periodic planar layer

For simulations in this thesis, HFSS has been used. The simulation setup can be chosen according to the type of the design and type of meshing to be used [Dined]. A vacuumbox is defined between two Floquent ports as a simulation volume shown in Fig. 3.1. The length of the vacuumbox is not a fixed value. The length of the vacuumbox should be sufficiently long in order to propertly account for evanesent higher-order modes in the structure but on the other hand it should be as

small as possible in order not to increase the simulation time. For converting the unit cell into a periodic structure, master/slave boundary conditions are used. The master/slave boundaries are paired, and their surfaces should have identical sizes and shapes [Ansedb]. In the simulations, direct or iterative solvers are used to expedite the simulation. In HFSS, the transmission and the reflection are described in terms of a scattering matrix (S-matrix). The scattering matrix corresponds to a microwave network relating the incident, reflected and transmitted power waves.

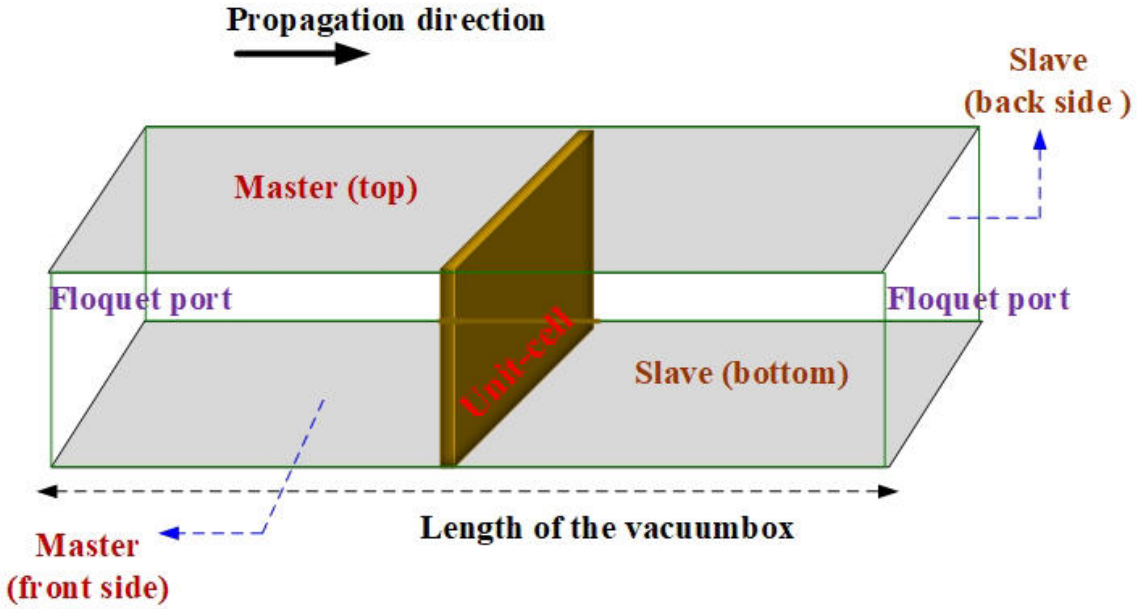

Figure 3.1 Simulation setup for a unit cell of an infinite planar layer.

In the full-wave simulations of this thesis, the simulation parameters such as the vacuumbox length, the solution setup and the type of meshing are not kept constant. The simulation-specific information is given in this chapter and the following chapters.

3.6 Infinite periodic planar metasheets from metal circular rings

In this section, results of a parametric study of the infinite periodic arrays from rings are presented based on full-wave simulations. As explained in Section 2.9, the unit cell and the size of the resonator affect the electromagnetic response dramatically. The size of the resonator and the unit cell are changed according to the desired frequency range. Analyzing the full-wave simulation results gives a chance to better understand the properties of the arrays of circular rings. Results of the full-wave simulations and measurements for concentric double rings on substrate FR4

and slots in a metal screen will also be shown. The effects of the dimensional parameters of the rings, dielectric substrate, thickness of the substrate and the unit cell are presented to get an idea of the electromagnetic responses of the infinite periodic planar array of metal circular rings, whose dimensional parameters are the outer radius (r_{out}), the inner radius (r_{in}) and the unit-cell length (periodicity p) as shown in Fig. 3.2. A normally linearly polarized plane wave is considered as the incident wave.

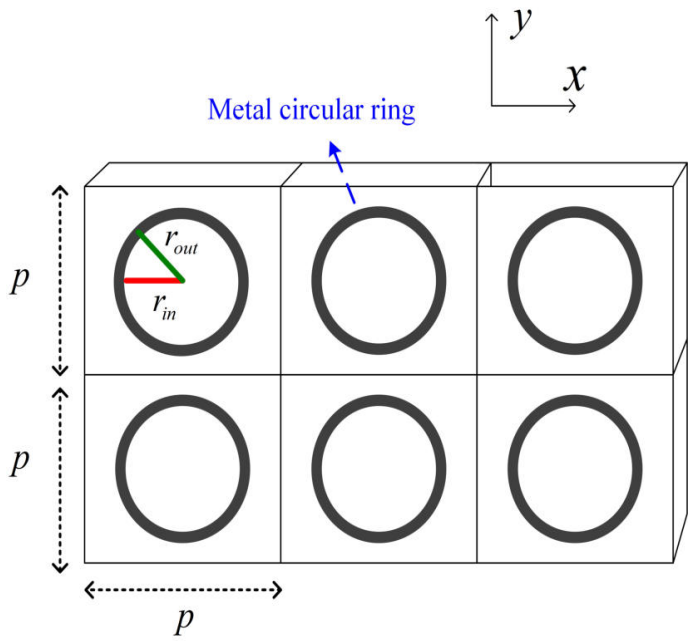

Figure 3.2 An infinite periodic planar array of circular rings obtained by the repetition of the unit cell.

The width of the rings ($r_{out} - r_{in}$) should be as small as possible to keep the shape of the resonator as a narrow planar ring. The resonator should not degenerate in a disc. The parameters are changed separately to better see the influence of every parameter on the transmission coefficient. Infinite periodic arrays of the rings in free space and on a dielectric substrate are analyzed.

In Fig. 3.3, the unit cell of the ring array is varied, while the dimension of the ring is kept constant. The transmission coefficient in Fig. 3.3 is S_{21} extracted from HFSS. In the metasheets, the unit cell should be smaller than the operational wavelength. When the size of the unit cells are smaller than the wavelength, the complete structure attains a macroscopic electromagnetic behavior because of the homogeneity [Mem15]. The length of the vacuumbox between two Floquet ports is 120 mm. The thickness of the rings is 0.018 mm. By changing the unit-cell size,

the resonance frequency is shifted nonlinearly. For understanding the effect, the polarizability approach, which is explained a bit later, can be used. Changing the unit-cell size changes the distance between the inclusions. When the distance becomes smaller, the interaction between the inclusions increases and causes a shift in the resonance [Mun00]. The frequency dependence of transmission can be shaped by changing the unit-cell size of the structure [PHA+08]. When the planar metasheet is illuminated by an incident wave, the coupling of electric fields gets stronger with smaller unit cells. In the full-wave simulations, auto meshing is used. The iterative solver and first-order basis functions are used for the unit-cell lengths 8 mm and 10 mm. The direct solver and mixed-order basis functions for the unit-cell size 12 mm are used. The ring material is perfect electric conductor (PEC).

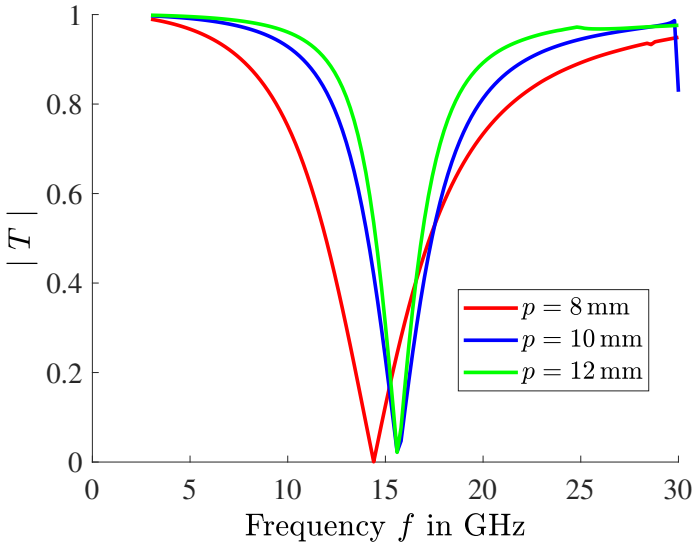

Figure 3.3 Amplitude of the transmission coefficient of an infinite periodic array of circular rings (outer radius 3.6 mm, inner radius 3.4 mm) in free space versus frequency.

For modeling transmission and reflection of arrays of electrically small inclusions, the concept of polarizability can be used. The inclusions can be electrically and/or magnetically polarizable. The electromagnetic response of inclusions can be expressed in terms of electric and/or magnetic dipole moments. The incident electric and magnetic fields induce current distributions in the inclusions. Collective electric and magnetic polarizabilities of the unit cells in the metasheet can be expressed as [ea15], [KPDRT18]

$$\mathbf{P} = \hat{\alpha}_{ee}\mathbf{E}_{inc} \tag{3.1}$$

$$\mathbf{M} = \hat{\alpha}_{mm}\mathbf{H}_{inc}, \tag{3.2}$$

where **P** and **M** are the induced electric and magnetic moments, $\hat{\alpha}_{ee}$ is the scalar electrical polarizability, and $\hat{\alpha}_{mm}$ is the scalar magnetic polarizability. $\mathbf{E}_{inc}$ and $\mathbf{H}_{inc}$ are the incident field vectors. Dipole moments are linearly dependent on the field through a polarizability. In this study, the magnetoelectric coupling is not included because the inclusion is a metal ring. Bi-anisotropic inclusions such as the Omega particle have this coupling. The transmission coefficient is obtained from the ratio of the forward scattered wave to the incident wave and the reflection coefficient from the ratio of the reflected wave to the incident wave. The equations for a normally incident plane wave which goes through the metasheet, can be written as [ea15], [KPDRT18]

$$\mathbf{E}_r = \frac{j\omega}{2S}(\eta_0\hat{\alpha}_{ee} - \frac{1}{\eta_0}\hat{\alpha}_{mm})\mathbf{E}_{inc} \tag{3.3}$$

$$\mathbf{E}_t = (1 + \frac{j\omega}{2S}(\eta_0\hat{\alpha}_{ee} + \frac{1}{\eta_0}\hat{\alpha}_{mm}))\mathbf{E}_{inc}, \tag{3.4}$$

where ω is the angular frequency, S is the area of the unit cell, η_0 is the free-space wave impedance, $\hat{\alpha}_{ee}$ and $\hat{\alpha}_{mm}$ are the effective (collective) electric and magnetic polarizabilities of the unit cells and $\mathbf{E}_r$, $\mathbf{E}_t$ are reflected and transmitted electric field vectors respectively [ea15], [KPDRT18]. By using (3.3) and (3.4), the relation between the resonance frequency, the unit-cell area and the effective electric polarizability can be defined. For example, for a perfect transmission, the magnitude values of transmission (T) and reflection (R) coefficients should be

$$R = \frac{|\mathbf{E}_r|}{|\mathbf{E}_{inc}|} = 0 \tag{3.5}$$

$$T = \frac{|\mathbf{E}_t|}{|\mathbf{E}_{inc}|} = 1. \tag{3.6}$$

Inserting (3.3) and (3.4) in (3.5) and (3.6) gives the equations

$$\frac{j\omega}{2S}(\eta_0\hat{\alpha}_{ee} - \frac{1}{\eta_0}\hat{\alpha}_{mm}) = 0. \tag{3.7}$$

$$\frac{j\omega}{2S}(\eta_0\hat{\alpha}_{ee} + \frac{1}{\eta_0}\hat{\alpha}_{mm}) = -2 \tag{3.8}$$

The resonance frequency of the metasheet can be expressed in terms of the effective electric polarizability and the unit-cell area as

$$\omega = \frac{-2S}{j\eta_0\hat{\alpha}_{ee}}. \tag{3.9}$$

The relation between the individual polarizabilites α_{ee}, α_{mm} of the inclusion and the effective polarizabilities are written as [ea15], [KPDRT18]

$$\hat{\alpha}_{ee} = \frac{1}{\frac{1}{\alpha_{ee}} - \beta_e}, \tag{3.10}$$

$$\hat{\alpha}_{mm} = \frac{1}{\frac{1}{\alpha_{mm}} - \beta_e}, \tag{3.11}$$

where β_e is the interaction constant of the infinite periodic array of electric dipoles. Thus, the angular frequency can be expressed in terms of the individual polarizability, the interaction constant and the unit-cell area as

$$\omega = \frac{-2S(\frac{1}{\alpha_{ee}} - \beta_e)}{j\eta_0}. \tag{3.12}$$

Equation (3.12) shows the relation between the frequency of a perfect transmission and the parameters of the array. The interaction constant (β_e) cannot be defined in a simple form even for simply shaped particles; therefore, the response of infinite planar metasheets has to be calculated by full-wave simulation.

Figure 3.4 shows the dependence of the transmission coefficient on frequency for several values of r_{in}. When the inner radius decreases, the stop-band region becomes broader due to the enlargement of the metal part of the ring, as the ring approaches a disc. In the full-wave simulations, an iterative solver, first order basis functions and auto meshing are used. The ring is PEC. The length of the vacuumbox between two Floquet ports is 120 mm. The length of the unit cell is 12 mm. The thickness of the ring is 0.018 mm.

A dielectric substrate is necessary due to mechanical reasons. Periodic structures without a dielectric substrate are analyzed to understand the role of the inclusions. The dielectric substrates can have a strong effect on the transmission and reflection curves. When a periodic array of planar inclusions is placed on a dielectric substrate, the resonant frequency changes. If the thickness of the dielectric substrate increases, the frequency may shift to lower values. By adjusting the parameters of the substrate, the transmission and reflection curves can be reshaped. Figure 3.5 shows the transmission coefficient of the array of PEC circular rings on different dielectric substrates with the thicknesses of 2 mm. The relative permittivities of the substrates RO3203, RO6010 and FR4 are 3.02, 10.2 and 4.4, respectively. The periodicity (unit-cell length) is 12 mm. The length of the vacuumbox between the two Floquet ports is 150 mm. The thickness of the ring is 0.018 mm. As it is seen from Fig. 3.5, when the relative permittivity increases, the resonance frequency decreases. Auto meshing, mixed order basis functions, the direct solver are used in the full-wave simulations where R03203 and R06010 are used for the dielectric substrate. First

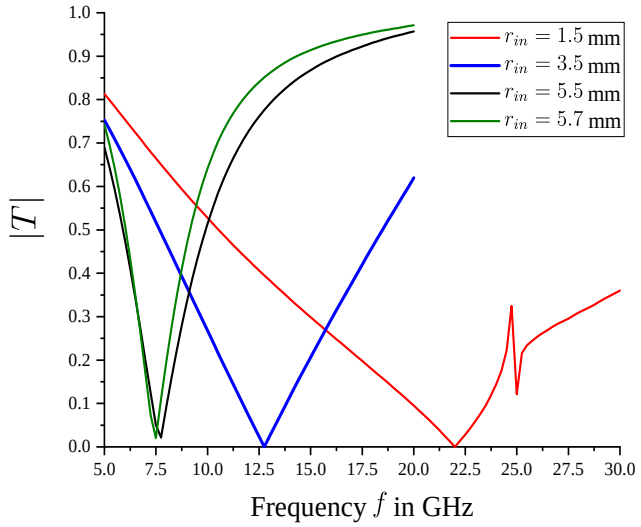

Figure 3.4 Amplitude of the transmission coefficient of an infinite periodic planar array of circular rings in free space with the fixed outer radius 5.9 mm and a varying inner radius (r_{in}).

order basis functions, iterative solver, auto meshing are used in the full-wave simulation where FR4 is used for the dielectric substrate.

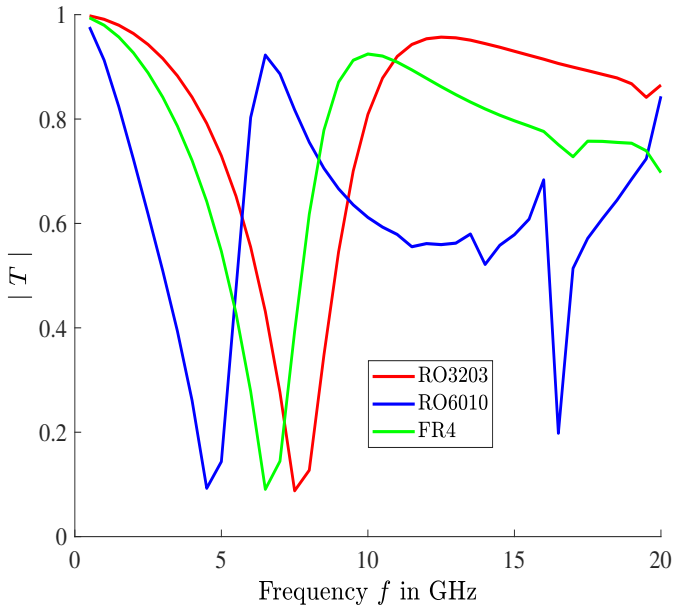

Figure 3.5 Amplitude of the transmission coefficient of a periodic array of rings (outer radius 5 mm and inner radius 4.8 mm on the different dielectric substrates) versus frequency.

The values of the resonance frequencies of the full-wave simulated infinite periodic planar array of circular rings ($r_{out}=5$ mm and $r_{in}=4.8$ mm, $p=12$ mm) without and with the dielectric substrates are shown in Table 3.1.

Table 3.1 Resonance frequencies of the array of circular rings ($r_{out}=5$ mm, $r_{in}=4.8$ mm).

In free space	RO3203	FR4	RO6010
10.6 GHz	7.5 GHz	6.5 GHz	4.5 GHz

The resonance frequency of the array of circular rings in free space is $f_0=10.6$ GHz. The shift in the resonance frequency caused by a substrate with the relative permittivity ε_r can be estimated by the formula [Mun00]

$$f_{new} \simeq \frac{f_0}{\sqrt{\varepsilon_r}}. \tag{3.13}$$

The exact resonance frequency of an array of rings on a substrate lies however between f_{new} and f_0, where the resonance frequency of the array on substrate RO3203 is between $f_{new}=6.09$ GHz and $f_0=10.6$ GHz. The resonance frequency of the array on substrate RO6010 is between $f_{new}=3.25$ GHz and $f_0=10.6$ GHz. It is seen that the resonance frequency is closer to f_{new}. Equation (3.13) does not give an exact estimate for the resonance frequency.

Figure 3.6 shows the effect of changing the thickness of the dielectric substrate. For metasheets, the thickness of the substrate should be smaller than the operational wavelength. First order basis functions, an iterative solver, interpolating sweep and auto meshing are chosen in the HFSS simulation setup. The unit-cell length is 12 mm. The length of the vacuumbox between two Floquet ports is 150 mm. The thickness of rings is 0.018 mm. As it is seen in Fig. 3.6, the resonance frequency is not a linear function of the thickness (t) .

The resonance frequency is mainly affected by the interaction of the arrays of planar metal inclusions and dielectric substrate. When the thickness increases too much, the metasheet starts to convert into a 3-D bulk structure. Inclusions can strongly interact with the surface of the dielectric substrate at their sides. Therefore, increasing the thickness of the substrate does not bring a linear shift on the resonance frequency. As observed in Fig. 3.6, the resonance frequency is kept mainly constant even if the thickness is changed from 2.5mm to 3mm. Roughly, it can be said that the resonance frequency is inversely proportional to the thickness of the dielectric substrate.

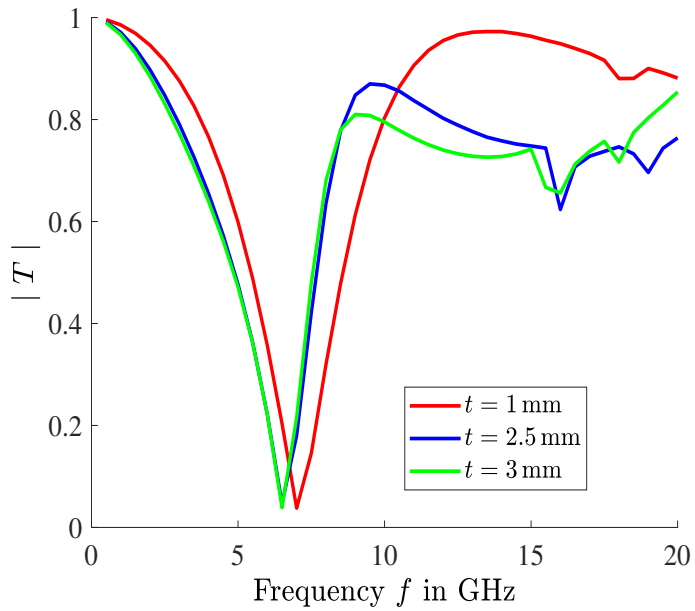

Figure 3.6 Amplitude of the transmission coefficient of an infinite periodic planar array of rings (outer radius 5 mm, inner radius 4.8 mm) on a dielectric substrate (FR4-epoxy) for several thickness values versus frequency.

3.7 Concentric double circular rings

One can use several concentric rings as an inclusion to get more design freedom. For example, the concentric circular rings in Fig. 3.7 have two resonance frequencies, at which the amplitude of the transmission coefficient is the lowest. If the size of one ring is kept constant and the size of the other one is changed, only one resonance frequency is shifted in free space as it is observed in Figs. 3.8 and 3.9.

The array consists of PEC rings in free space with the unit-cell size 12 mm. The vacuumbox length between the Floquet ports is 90 mm. The iterative solver, first order basis functions, interpolating sweep and classic mesh are chosen in the HFSS simulation setup.

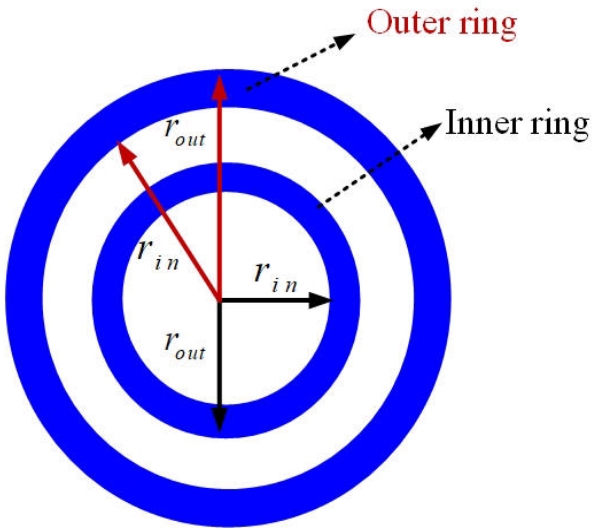

Figure 3.7 Double-ring inclusion.

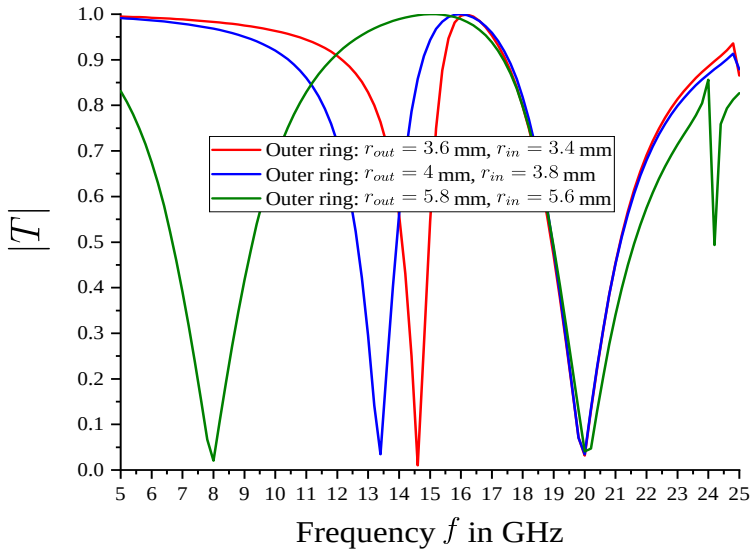

Figure 3.8 Amplitude of the transmission coefficient of an infinite periodic planar array of concentric circular rings in free space (outer and inner radii of the inner ring are 2.8 mm and 2.6 mm, respectively) versus frequency.

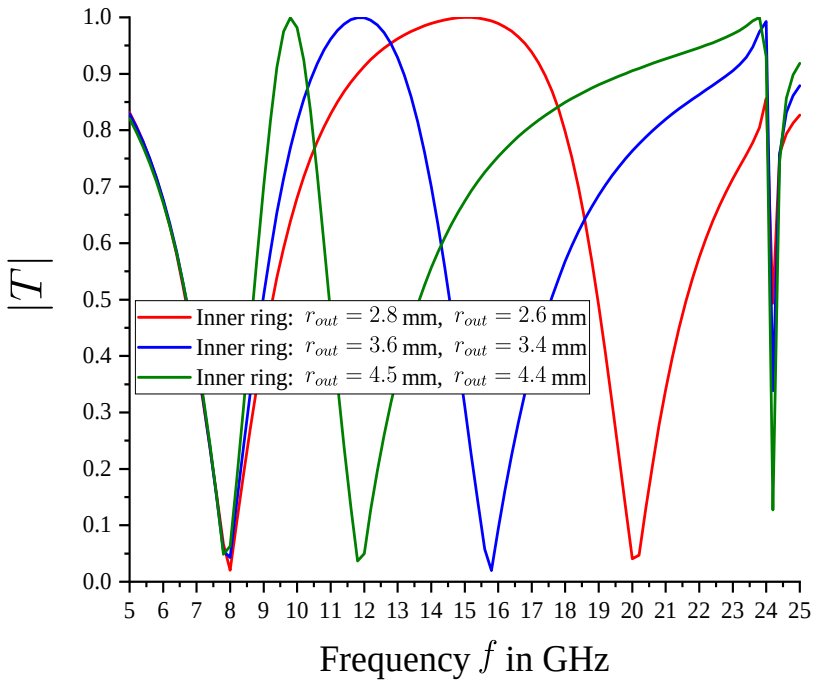

Figure 3.9 Amplitude of the transmission coefficient of infinite periodic planar array of concentric double circular rings in free space (outer and inner radii of the outer ring are 5.8 mm and 5.6 mm, respectively) versus frequency.

3.8 Concentric double circular slots

Arrays of circular slots in a metal screen in Fig. 3.10 show complementary transmission and reflection properties with respect to the circular rings, which can be explained by the Babinet principle. The array of concentric double circular slots create two resonance frequencies where the amplitude of the transmission coefficient has its maximum value. Figure 3.11 is an illustration of the complementary properties.

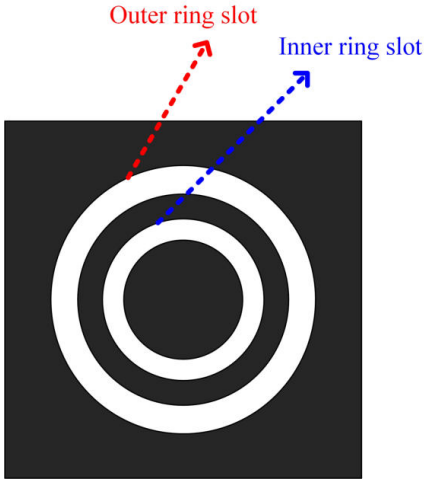

Figure 3.10 Concentric double circular slots in a metal screen.

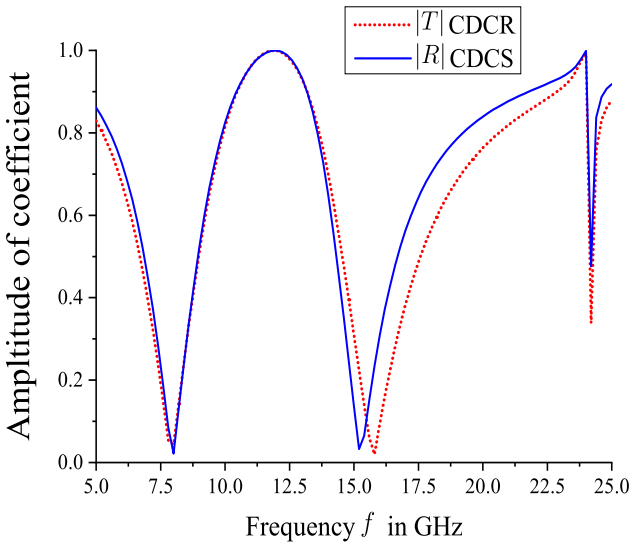

Figure 3.11 Comparison of the reflection coefficient for the infinite periodic array of concentric circular slots and transmission coefficient of the infinite periodic array of concentric double circular rings.

The reflection coefficient of an infinite periodic array of concentric double circular slots (CDCS) and the transmission coefficient of an infinite periodic array of concentric double circular rings (CDCR) are compared. It is seen that the reflection coefficient of the slot array can be estimated from the transmission coefficient of the ring array or vice versa. For the outer ring (or slot), the radius values are $r_{out} = 5.8$ mm, $r_{in} = 5.6$ mm and for the inner ring (or slot), the radius values are $r_{out} = 3.6$ mm, $r_{in} = 3.4$ mm. The thickness of the rings (metal screen for slots) is 18 μm. The length of the unit cell is 12 mm. The length of the vacuumbox between the Floquet ports is 90 mm. The iterative solver, first order basis functions, interpolating sweep and classic mesh are chosen in the HFSS simulation setup. The curves are not identical in Fig. 3.11 because the structure has a finite thickness. In the higher frequencies, the thickness starts to be comparable with the wavelength.

Below, a variety of full-wave simulation results for complementary concentric rings in the UHF band is presented. This frequency band is used for the Galileo Navigation Signals [Galed]. To have resonance frequencies at the lower frequencies, the unit-cell size and the radius of the rings should be increased.

Figure 3.12 shows that when the thickness of the metal screen increases, the magnitude of the transmission coefficient decreases. The material of the metal parts was assumed to be PEC in the simulations. For better transmission, thin metal inclusions are preferred. The change in the thickness of the screen insignificantly affects the resonance frequencies. The unit-cell length is 79 mm. The radii values are chosen as $r_{out} = 39.23$ mm and $r_{in} = 37.73$ mm for the outer ring and $r_{out} = 30.125$ mm and $r_{in} = 29.625$ mm for the inner ring. The length of the vacuumbox between two Floquet ports is 300 mm. The PEC screen with the slots is in free space. There is no substrate. Auto meshing, an iterative solver and mixed order basis functions are chosen in the HFSS simulation setup.

Next, a metal screen with circular slots, which are backed by a dielectric substrate, is considered because of its material properties. Its relative permittivity is 1.05 and the dielectric tangent loss is 0.0003. The substrate Rohacell51GA is close to vacuum; therefore, the electromagnetic response is close to the case of the ring array in free space. Furthermore, in Fig. 3.13, the dielectric substrate is kept constant and only the dimensions of the rings in the unit cell are changed. The unit-cell length is 79 mm. The thickness of the substrate is 3 mm. The material of the rings is copper. The vacuumbox length between the Floquet ports is 320 mm. Interpolating sweep, an iterative solver, mixed-order basis functions, auto meshing are chosen in the HFSS simulation

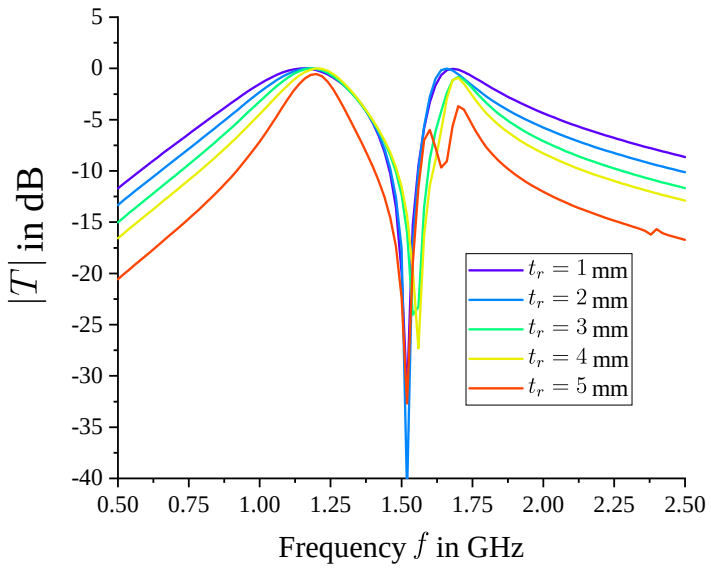

Figure 3.12 Amplitude of the transmission coefficient of an infinite planar array of concentric double circular slots in free space versus frequency for various thickness.

setup. The thickness of the metal screen is 3mm. The dimensions of the slots are given in Tables 3.2 and 3.3.

The amplitude of the transmission coefficient or the resonance frequency can be altered by changing the dielectric substrate material, the thickness of the dielectric substrate, dimensional parameters of the rings and the unit cell. The dimensions of the rings are adjusted to have the same resonance frequencies with different dielectric substrates in Fig. 3.14.

Table 3.2 Outer ring dimensions of concentric double circular slots in a metal screen backed by a Rohacell51G substrate.

Concentric double circular slots	r_{out} in mm	r_{in} in mm
(1)	39.00	37.96
(2)	38.66	38.30
(3)	38.50	38.46
(4)	39.00	37.96

The effect of dielectric substrate on the resonance frequencies are strong. Only adjusting the dimensions of the slots may not be enough. The unit cell should be changed also. The material of the screen is copper. The thickness of the metal screen is 0.2mm. The thickness

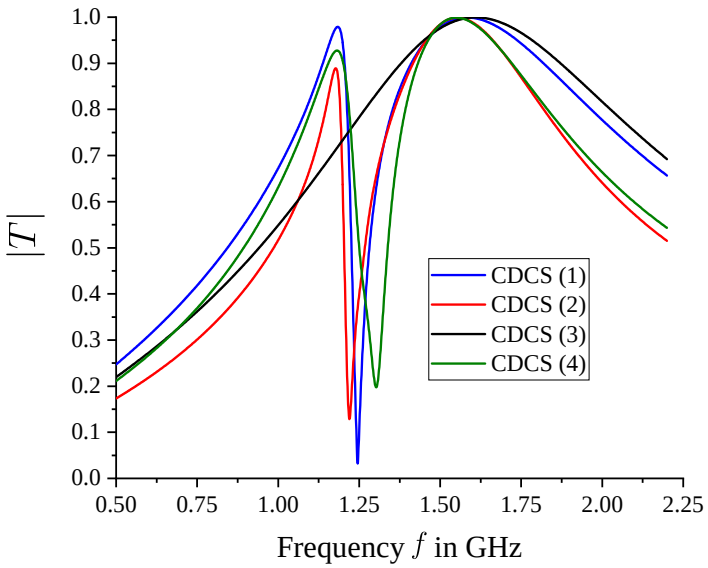

Figure 3.13 Amplitude of the transmission coefficient of an infinite planar array of concentric double circular slots versus frequency (The average radius is kept same. The substrate is Rohacell51GA.)

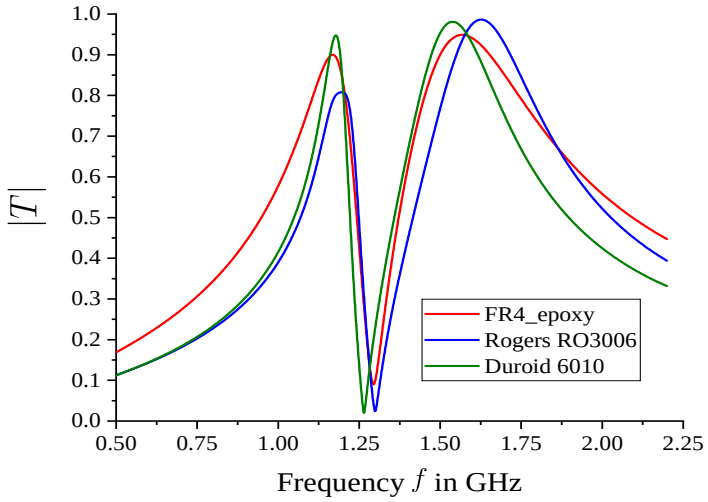

Figure 3.14 Amplitude of the transmission coefficient of an infinite planar array of concentric double circular slots for three different dielectric substrates. The dimensions of the circular slots are adjusted so as to have the same resonance frequencies.

of the dielectric substrate is 3 mm. Classic meshing, mixed-order basis functions, an iterative

Table 3.3 Inner ring dimensions of concentric double circular slots in a metal screen backed by a Rohacell51G substrate.

Concentric double circular slots	r_{out} in mm	r_{in} in mm
(1)	36.5	29.5
(2)	35	31
(3)	37	29
(4)	35	31

solver are chosen in the HFSS simulation setup. The dimensions of the slots for three different substrates are given in Tables from 3.4 to 3.6.

Table 3.4 Dimensions of concentric double circular slots in a metal screen backed by the substrate Duroid6010 for periodicity $p = 50$ mm.

Concentric double rings	r_{out} in mm	r_{in} in mm
Outer ring	21.5	20.0
Inner ring	17.5	16.0

Table 3.5 Dimensions of concentric double circular slots in a metal screen backed by the substrate Duroid3006 for periodicity $p = 60$ mm.

Concentric double rings	r_{out} in mm	r_{in} in mm
Outer ring	25	24
Inner ring	20.5	19

As it is seen from Fig. 3.15, changing the material of the substrate affects both resonance frequencies. While the relative permittivity is increased, the resonance frequencies are shifted to lower frequencies. For staying in the defined frequency range, the dimensions of the rings should be smaller if the relative permittivity of the dielectric substrate increases. The dimension of the concentric double circular slots is shown in Table 3.7. The unit-cell length (periodicity) is 79 mm. The thicknesses of the rings is 0.2 mm. The thickness of the dielectric substrate is 3 mm. The length of the vacuumbox is 320 mm. Classic meshing, an iterative solver, mixed-order basis functions are chosen in the HFSS simulation setup.

Table 3.6 Dimensions of concentric double circular slots in a metal screen backed by the substrate FR4 for periodicity $p = 60$ mm.

Concentric double slots	r_{out} in mm	r_{in} in mm
Outer ring	27.5	26.5
Inner ring	23	22

The unit-cell size and the dimensions of the rings need to be adjusted to have the resonance response in the preferred frequency band. According to the simulation results in this chapter, the rings and the unit cells are smaller for the X band than for the UHF band.

Full-wave simulation is insufficient as a design method. Metasheet design by full-wave simulations means the need to do many tries by changing the design parameters. The full-wave simulations are useful to verify the electromagnetic response of the designed structure. For designing the metasheets, suitable methods should be developed.

Table 3.7 Dimensions of concentric double circular slots in a metal screen backed by various dielectric substrates.

Concentric double circular slots	r_{out} in mm	r_{in} in mm
Outer ring	38.96	38.00
Inner ring	34.00	32.00

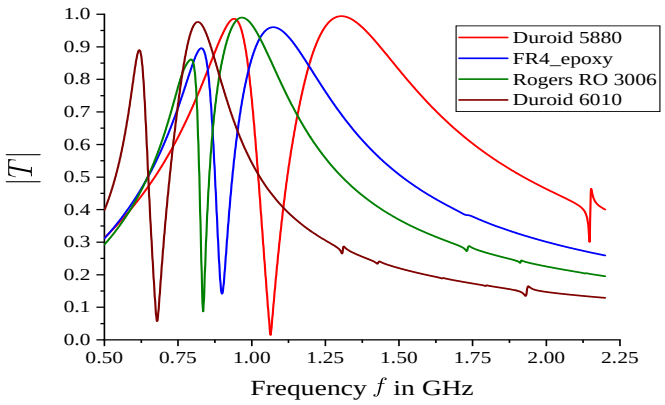

Figure 3.15 Amplitude of the transmission coefficient of an infinite planar array of concentric double circular slots versus frequency. (The unit-cell size is 79mm. The dimensions of the circular slots are kept constant.)

3.9 Full-wave simulation and measurement for a periodic array of concentric double rings

In this section, simulation results for the array of double ring structure and the array of double slot structure are compared with measurements. The manufactured arrays of concentric double rings and concentric double slots are shown in Figs. 3.16 and 3.17. The copper arrays are placed on FR4 substrate. The thickness of the substrate is 2 mm. The length of the unit cell is 20 mm. The outer and inner radii of the outer ring are 9.8 mm and 8.3 mm, respectively. The outer and inner radii of the inner ring are 5.1 mm and 4.6 mm, respectively. The thickness of the rings are 50 μm. The frequency range is between 1 GHz and 20 GHz. The length of the vacuumbox between two ports is 80 mm.

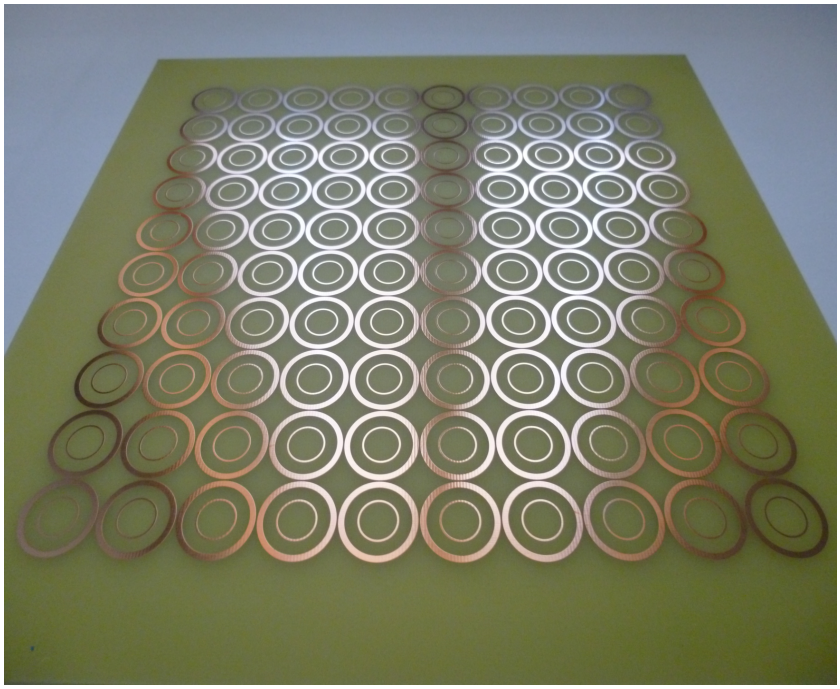

Figure 3.16 Concentric double rings on an FR4 substrate.

In Figs. 3.18 and 3.19, there is a good match between the results from the measurement and the full-wave simulation. The simulation setup for the infinite periodic planar layer which is explained in Section 3.5, is used in this section. Interpolating sweep, iterative solver and auto meshing model are chosen in the simulation setup. In the full-wave simulation, normal incident plane wave and linear polarization are considered.

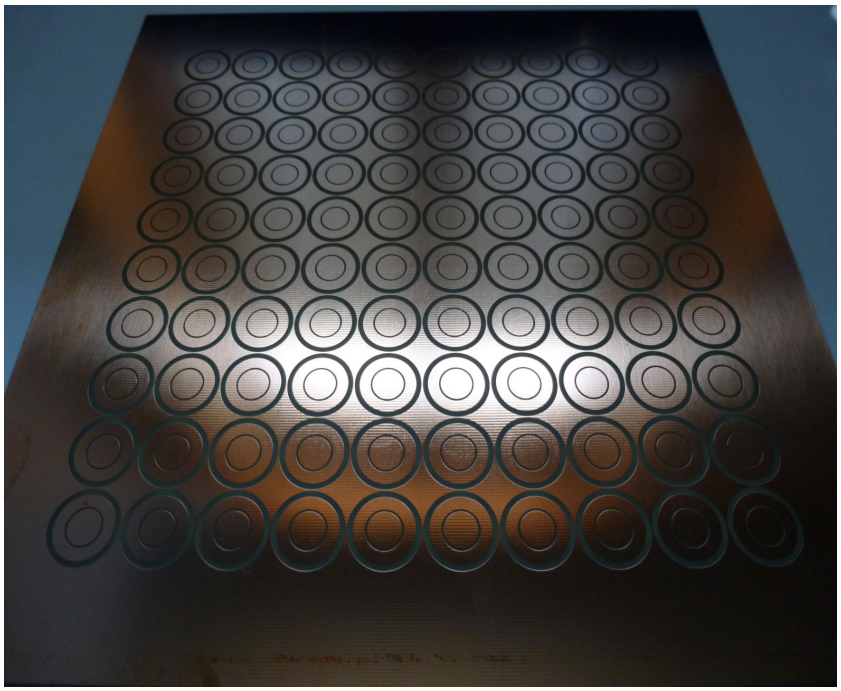

Figure 3.17 Concentric double circular slots on an FR4 substrate.

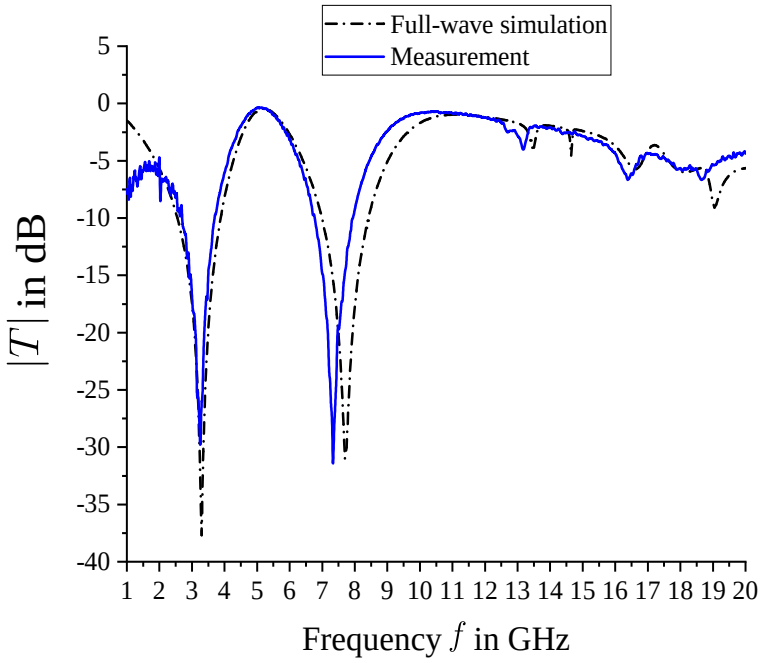

Figure 3.18 Comparison of measured and full-wave simulation results for transmission through an array of concentric double rings on an FR4 substrate.

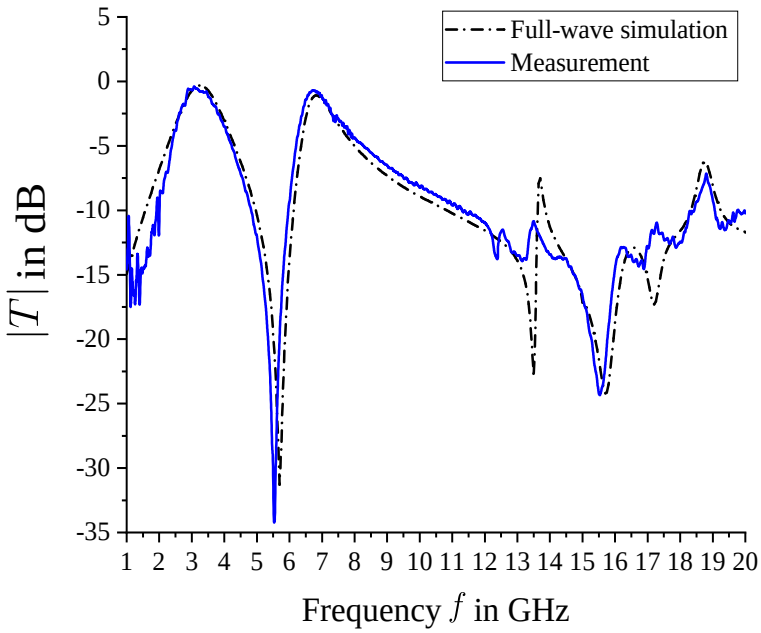

Figure 3.19 The same as in Fig. 3.18 but for an array of concentric double circular slots in a metal screen backed by an FR4 substrate.

The electromagnetic response of the array of concentric double metal rings shows a band-stop behavior at two frequencies. The electromagnetic response of the array of concentric double circular slots in a metal screen shows the resonance points where the transmission has the highest value. It shows band-pass behavior at two frequencies.

Chapter 4

Equivalent Circuit Modelling of Metasheets

4.1 Approximation for the transmission of an array of circular rings without substrate

The transmission line approach is helpful for analyzing the properties of one-dimensional propagation. Waves propagate only in one direction if the length of the uniform transmission line is infinite. The line is infinitely long so there are no reflections from a non-existent end. Suppose there is a load at the far end of the cable whose impedance matches the characteristic impedance of the transmission line. Then regardless of the transmission line length, there will be no reflections. There are forward and backward propagating waves if the transmission line is shunted with an inductance, capacitance or resistance. Such lumped elements are a discontinuity on a transmission line so a propagating wave cannot simultaneously satisfy the boundary conditions.

In this study, metasheet structures are represented by LC circuits (Fig. 4.1). Consider, for example, a plane wave which goes in the $+z$ direction, through a conducting metal ring, placed between a pair of infinitely thin perfectly conducting plates. The plane wave has no components of the electric and magnetic field along the propagation direction. Therefore, the xy-plane can be considered as equiphase. TEM transmission lines are shown graphically as parallel lines and their characteristic impedance Z_0 is presented in Fig. 4.1. The characteristic impedance of the transmission line is equal to the free space impedance Z_0. If the dimensions of the planar resonator are smaller than the wavelength of the operational frequency, then the conducting planar rings can be represented by an equivalent impedance.The thickness of rings has a constant

value as 18 μm. The width of the rings are between 0.1 mm and 0.2 mm. The thickness of the ring is neglected in the following analysis.

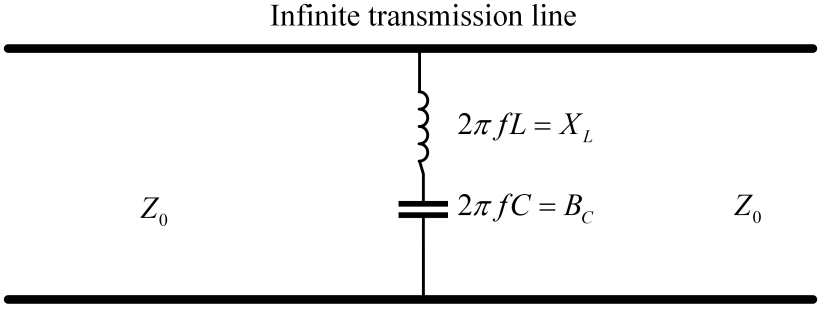

Figure 4.1 Shunted transmission line with an equivalent impedance.

The input impedance, which has inductive reactance $X_L = 2\pi f L$ and capacitive susceptance $B_C = 2\pi f C$, can be written in terms of a complex reactance X_g [And75]. The expression for X_g in terms of capacitive reactance and inductive reactance can be written as [And75]

$$X_g = X_L + X_C = 2\pi f L - \frac{1}{2\pi f C}. \tag{4.1}$$

Normalizing (4.1) to the free-space impedance gives

$$X_{nor} = \frac{2\pi f L}{Z_0} - \frac{1}{Z_0 2\pi f C}. \tag{4.2}$$

The input impedance Z_i normalized to Z_0 is calculated according to the equivalent circuit in Fig. 4.2 as

$$Z_i = \frac{jX_{nor}}{1 + jX_{nor}}. \tag{4.3}$$

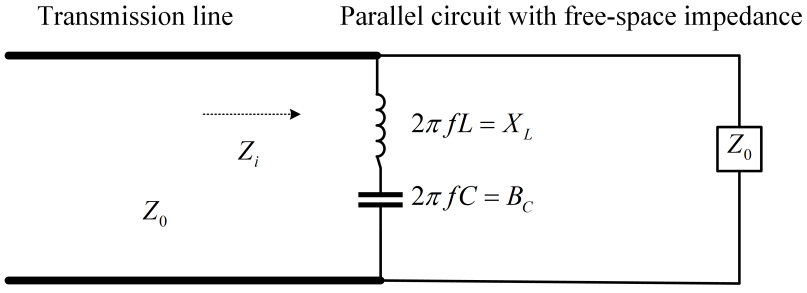

Figure 4.2 Transmission line from Fig. 4.1 as a parallel circuit with free-space impedance.

In the lossless case, the transmission coefficient T is related to the reflection coefficient R as

$$1 + R = T. \tag{4.4}$$

The reflection coefficient in terms of the input impedance is

$$R = \frac{Z_i - 1}{Z_i + 1}. \tag{4.5}$$

It gives the transmission coefficient as

$$1 + \frac{Z_i - 1}{Z_i + 1} = T \tag{4.6}$$

$$T = \frac{2Z_i}{Z_i + 1}. \tag{4.7}$$

Inserting (4.3) in (4.7) results in

$$T = \frac{4X_{nor}^2 + j2X_{nor}}{1 + 4X_{nor}^2}. \tag{4.8}$$

Real and imaginary parts of the transmission coefficient can be expressed through the normalized reactance as

$$T_{real} = \frac{4X_{nor}^2}{1 + 4X_{nor}^2} \tag{4.9}$$

and

$$T_{im} = \frac{2X_{nor}}{1 + 4X_{nor}^2}. \tag{4.10}$$

The frequency f is written in terms of propagation constant k_0 and speed of light c in free space as

$$f = \frac{k_0 c}{2\pi} \tag{4.11}$$

and inserting (4.11) in (4.2) gives

$$X_{nor} = \frac{2\pi \frac{k_0 c}{2\pi} L}{Z_0} - \frac{1}{Z_0 2\pi \frac{k_0 c}{2\pi} C}. \tag{4.12}$$

Writing Z_0 in terms of dielectric constant ε_0 and speed of light c as

$$Z_0 = \frac{1}{\varepsilon_0 c} \tag{4.13}$$

and inserting (4.13) in (4.12) gives

$$X_{nor} = k_0 \varepsilon_0 c^2 L - \frac{\varepsilon_0}{k_0 C}. \tag{4.14}$$

and, k_0 is replaced by $\frac{k_0 p}{p}$, then $k_0 p = k_{nor}$. X_{nor} can be expressed in terms of k_{nor} to give

$$X_{nor} = \frac{k_0 p}{p} \varepsilon_0 c^2 L - \frac{\varepsilon_0}{\frac{k_0 p}{p} C}. \tag{4.15}$$

For right-angled inclusions like Jerusalem-crosses, square rings and cut-wires, it is possible to express the circuit parameters L and C through their dimensions [And75], [Mun00]. Because of the rounded shape of circular rings, the inductive reactance and capacitive susceptance cannot be written directly in terms of their dimensions. Therefore, the equivalent impedance X_{nor} is expressed through two unknown functions which define the inductive and capacitive effects in the circuit. Terms $(\varepsilon_0 c^2 L)/p$ and $(p\varepsilon_0)/C$ in (4.15) in terms of functions F_1 and F_2 are written as

$$X_{nor} = k_{nor} F_1(r_{nor}) - \frac{1}{k_{nor}} F_2(r_{nor}), \tag{4.16}$$

where F_1 and F_2 are unit-less functions of r_{nor} which is the normalized average radius $\frac{r_{av}}{p} = r_{nor}$ is calculated by the arithmetic average of the outer and inner radii of the rings.

For calculating the transmission coefficient, (4.16) is inserted into (4.9) and (4.10), which results:

$$T_{real}(r_{nor}, k_{nor}) = \frac{4(k_{nor}^2 F_1 - F_2)^2}{k_{nor}^2 + 4(k_{nor}^2 F_1 - F_2)^2}, \tag{4.17}$$

$$T_{im}(r_{nor}, k_{nor}) = \frac{2k_{nor}^3 F_1 - 2k_{nor} F_2}{4k_{nor}^4 F_1^2 + k_{nor}^2(1 - 8F_1F_2) + 4F_2^2}. \tag{4.18}$$

In these equations, suitable approximations will be used for the functions F_1 and F_2. To determine the coefficients of the approximations, curve fitting is applied. This process is applied in MATLAB by using the fitting toolbox with the Levenberg-Marquardt, and Trust-Region methods. The Levenberg-Marquardt method is a well known algorithm to solve nonlinear least square problems by fitting a parametrized function to a set of available data by minimizing the sum of the squares of the errors between the data and the function [Gaved]. The trust region algorithm computes a trial step by solving a subset of the region of the model function. If the approximated solution matches the original problem well, then the trust region is expanded. Otherwise, the trust region should be downsized [Mated], [Yua15].

Depending on the chosen method, the values of the coefficients in the fitting function can be changed. These values are not unique. The most important thing is that the proper coefficient values are found. Another advantage is that this semianalytical approach can be extended to more than two variables in the algorithm which is used for fitting.

The amplitude and the phase of the transmission coefficient can be calculated as

$$|T| = \sqrt{T_{real}^2 + T_{im}^2}, \tag{4.19}$$

$$\tan(\theta_T) = \frac{T_{im}}{T_{real}}. \tag{4.20}$$

The analytical expressions in (4.17) and (4.18) represent the complex transmission coefficient as a function of k_{nor} normalized propagation constant according to the periodicity p which is the unit-cell length as shown in Fig. 3.2. A resonance occurs when both the real and imaginary parts in (4.17) and (4.18) become zero, when [zOE18]

$$k_{nor}^2 = \frac{F_2}{F_1}. \tag{4.21}$$

Thus, the resonance frequency depends only on the ratio of F_2 and F_1.

The transmission coefficients in (4.17) and (4.18) depend only on the normalized wavenumber and the free parameters F_1 and F_2. In order to determine these free parameters, the absolute value of the transmission coefficient as given in (4.19) will be fitted to full-wave simulations for seven different values of the ring radii with one constant periodicity (12 mm). The length of the vacuumbox between the two Floquet ports for the simulation is 120 mm. To eliminate the effect of the vacuumbox which causes the oscillation in the phase, the simulation data is multiplied by $e^{jk_0\ell}$, where ℓ is the distance between the two ports in the simulation setup in Section (3.5). In the full-wave simulation setup, mixed order basis functions and the direct solver were chosen. The frequency range is between 3 GHz and 30 GHz. Fitting (4.19) in the MATLAB curve fitting

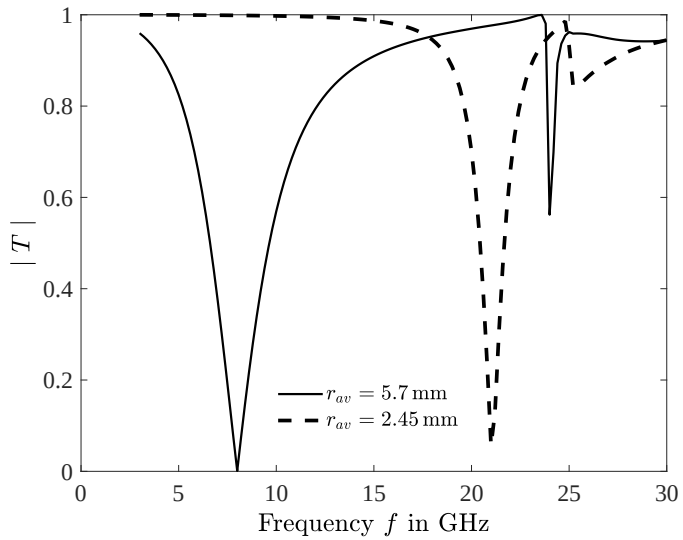

Figure 4.3 Full-wave simulated amplitude of the transmission coefficient of an array of circular rings in free space for the largest and smallest radius values [zOE18] [reproduced figure courtesy of The Electromagnetics Academy].

tool to the numerical data shown in Fig. 4.3 yields the values of F_1 and F_2 in dependence on the normalized r_{av} in Table 4.1. The dependence of F_1 and F_2 on r_{av} suggests an exponential

approximation

$$F_1(r_{nor}) = a_1 e^{(b_1 r_{nor})} + c_1 e^{(d_1 r_{nor})}$$
$$F_2(r_{nor}) = a_2 e^{(b_2 r_{nor})} + c_2 e^{(d_2 r_{nor})}. \tag{4.22}$$

Table 4.1 Curve fitting of the amplitude of the transmission coefficient on the full-wave simulation data for several radius values [zOE18] [reproduced table courtesy of The Electromagnetics Academy].

r_{av} in mm	F_1	F_2
2.45	0.9104	25.490
2.70	0.7232	17.670
3.50	0.5422	8.342
3.90	0.4872	6.031
4.45	0.5096	4.551
4.90	0.4134	2.976
5.70	0.3826	1.541

By fitting (4.22) to the data from Table 4.1, the coefficients a, b, c and d can be obtained as shown in Table 4.2. The curves plotted in Figs. 4.4 and 4.5 show a good quality of the approximations (4.22).

Table 4.2 Coefficients of the exponential approximation in (4.22) [zOE18] [reproduced table courtesy of The Electromagnetics Academy].

Coefficients	F_1	F_2
a	1347	1.015×10^5
b	-41.47	-46.32
c	0.9106	103.6
d	-1.826	-8.694

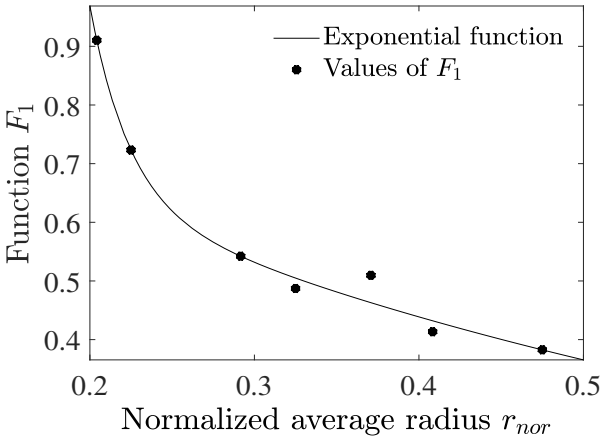

Figure 4.4 Fitting quality of the exponential approximation at the specific values of F_1 [zOE18] [reproduced figure courtesy of The Electromagnetics Academy].

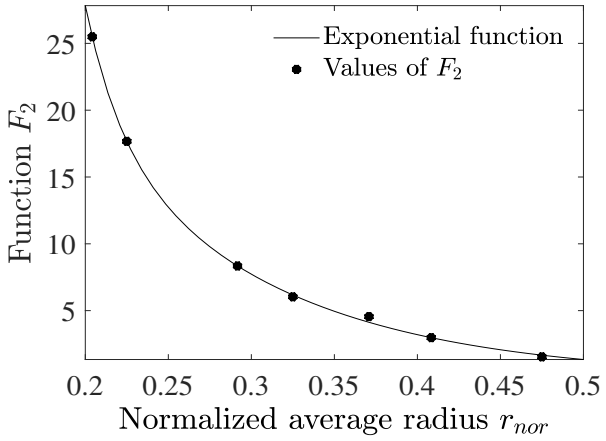

Figure 4.5 The same as in Fig. 4.4 but for F_2 [zOE18] [reproduced figure courtesy of The Electromagnetics Academy].

4.2 Semianalytical approach versus full-wave simulation for arrays of rings in free space

The results of the full-wave simulation and the semianalytical approach in Section 4.1 are compared for arrays of differently sized circular rings. A radius value from the interval $2.45 \leq r_{av} \leq 5.7$, see Table 4.1, is chosen. As it is seen from Figs. 4.6 and 4.7, there is a good match between the semianalytical approach and the full-wave simulation.

The relation (4.21) plays an important role in adjusting the resonance frequency. It follows from (4.21) that the value of k_{nor}, at which the transmission coefficient is at minimum, does not change if all geometrical dimensions of the structure are scaled with a proper factor. Figure 4.8

shows that the resonances (blockage frequencies) of the transmission coefficients for the arrays of the circular rings with different radii and periodicity values are located at the same value of the normalized wavenumber $k_{nor}^2 = 7.2942$ [zOE18], as expected. In the simulation setup, the length of the vacuumbox between the Floquet ports is 150 mm. The mixed-order basis functions, an iterative solver and interpolating sweep have been used in the full-wave simulation.

As an intermediate conclusion, it can be said that the semianalytical model for arrays of PEC rings without substrate matches very well with full-wave simulation results.

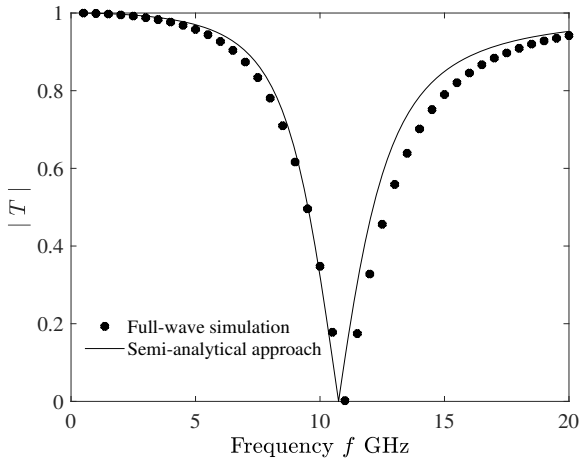

Figure 4.6 Amplitude of the transmission coefficient for the array of rings ($r_{out} = 4.9$mm, $r_{in} = 4.7$mm and $p = 12$mm) without substrate [zOE18] [reproduced figure courtesy of The Electromagnetics Academy].

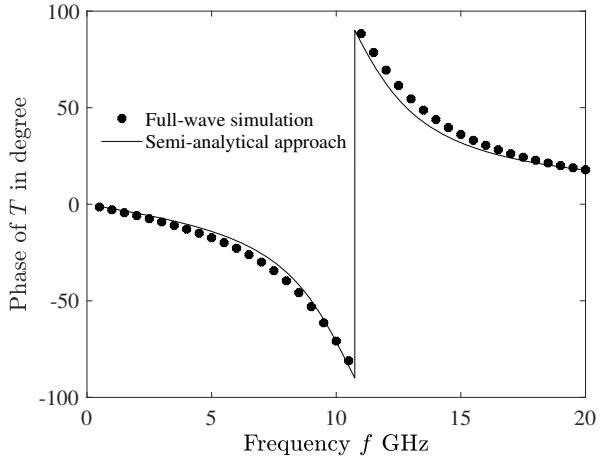

Figure 4.7 Phase of the transmission coefficient for the array of rings ($r_{out} = 4.9$mm, $r_{in} = 4.7$mm and $p = 12$mm) without substrate [zOE18] [reproduced figure courtesy of The Electromagnetics Academy].

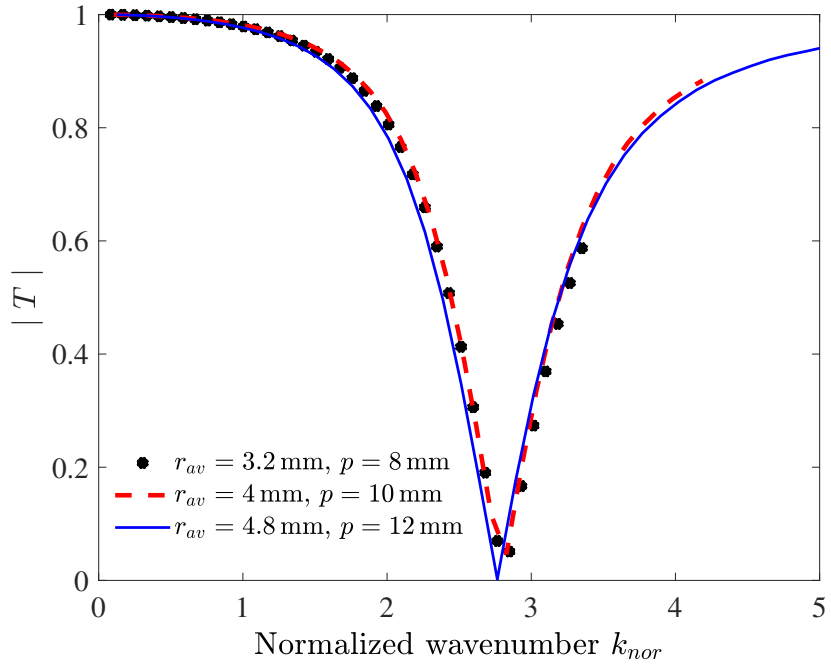

Figure 4.8 Full-wave simulated transmission coefficient with different radii and periodicities of the array of circular rings in free space (normalized radius is 0.4) [zOE18] [reproduced figure courtesy of The Electromagnetics Academy]

4.3 Semianalytical approach to the planar array of circular slots in a metal screen

According to the Babinet's principle, the transmission coefficient of the planar array of circular slots in a thin planar PEC screen is equal to the reflection coefficient of the array of thin PEC rings in free space. The semianalytical approach is used to calculate the amplitude of the reflection coefficient.

The results of this approach will be compared with full-wave simulation results for infinite periodic arrays of circular slots. The unit-cell length is 12 mm. A normally incident plane wave is considered. The length of the vacuumbox between the Floquet ports is 60 mm. The direct solver and the mixed-order basis functions have been used. The lambda target for refining the mesh was chosen as 0.2. The classic mesh model and discrete sweep were chosen.

As it is seen from Figs. 4.9, 4.10 and 4.11, there is a good match between the semianalytical approach and full-wave simulation. The Babinet's principle worked well even if the structure has a constant thickness.

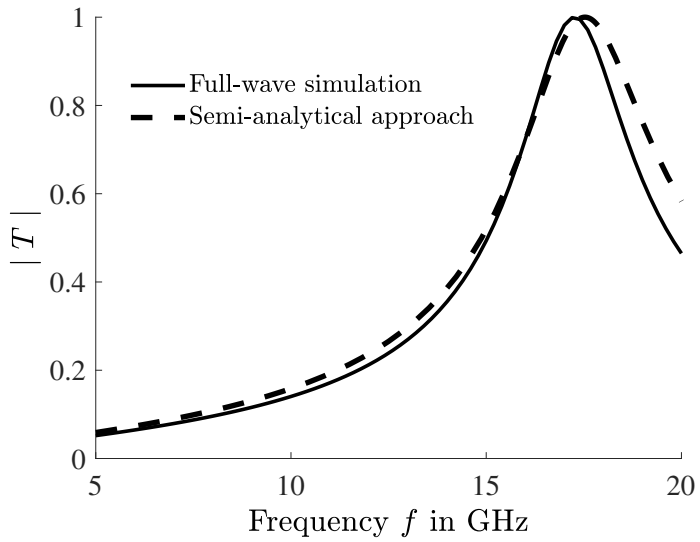

Figure 4.9 Amplitude of the transmission coefficient for the array of circular slots with $r_{out} =$ 3.2 mm and $r_{in} = 3$ mm in a metal screen without substrate.

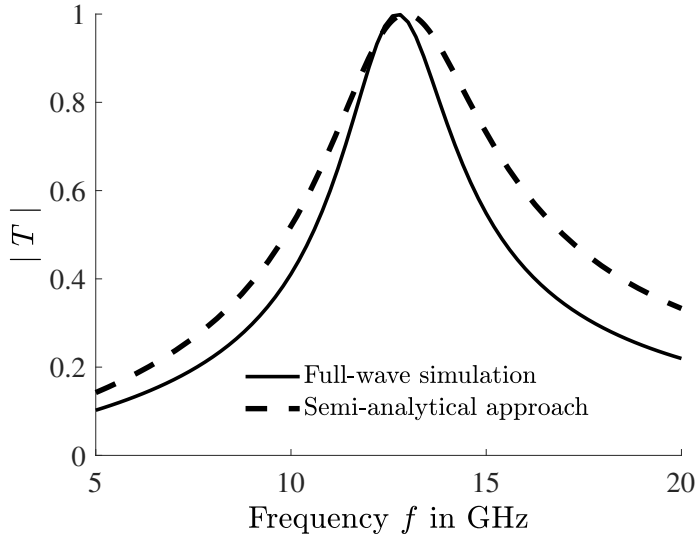

Figure 4.10 Amplitude of the transmission coefficient for the array of circular slots with $r_{out} =$ 4.2 mm and $r_{in} = 4.1$ mm in a metal screen without substrate.

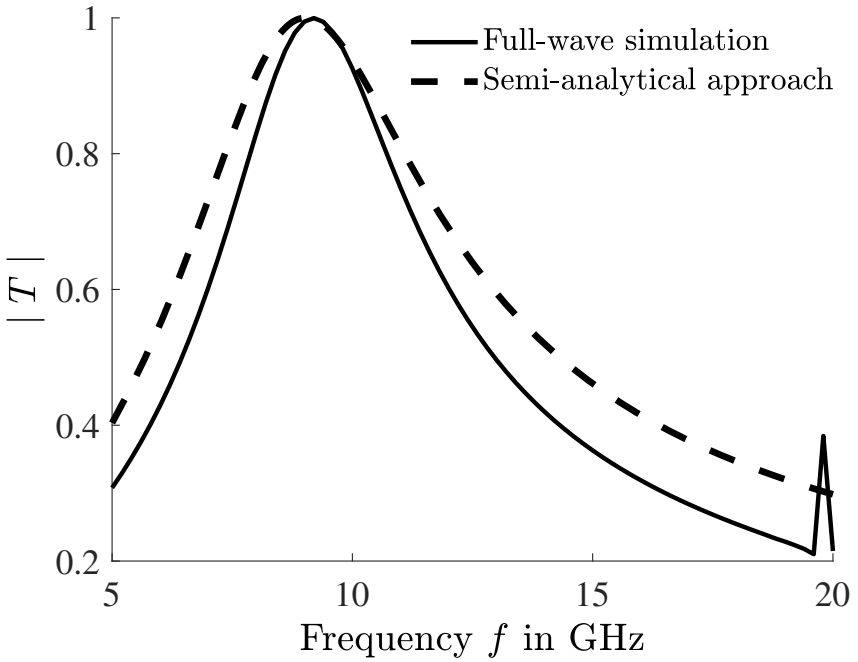

Figure 4.11 Amplitude of the transmission coefficient for the array of circular slots with $r_{out} =$ 5.5 mm and $r_{in} = 5.32$ mm in a metal screen without substrate.

4.4 Array of double rings in free space

As shown in Section 3.7, two concentric rings (Fig. 3.7) create two resonance frequencies, at which the amplitude of the transmission coefficient is the lowest. For concentric rings in free space, the same coefficients of the exponential approximations (4.22), which are calculated for a single ring, are used. The radius values of the concentric rings should be in the range of the radius values that were used in the fitting process in Section 4.1. Therefore, there is no need to repeat the fitting for concentric rings in free space. If the concentric rings are supported by a dielectric substrate, then the fitting needs to be redone because the dielectric substrate changes the impedance of the rings.

The equivalent circuit should be accordingly adjusted. It is now a band-stop filter at two frequencies. A series LC circuit, which is shunted across the transmission line, creates one resonance frequency. For having a second resonance frequency, another series LC circuit is connected in parallel to the first one as it is shown in Figs. 4.12 and 4.13.

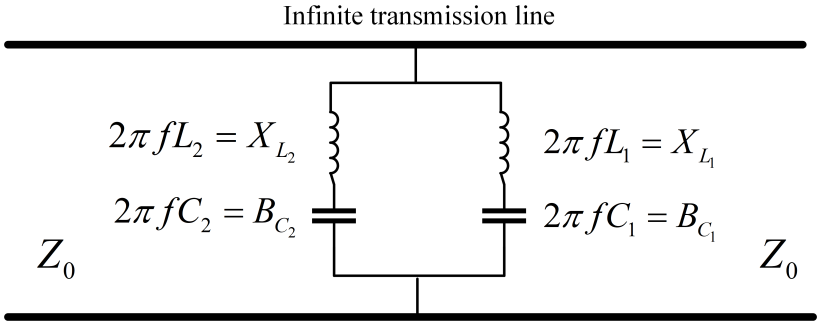

Figure 4.12 Equivalent circuit for double rings in free space.

The complex impedances in each series circuit are written as

$$X_{g_1} = X_{L_1} + X_{C_1} = 2\pi f L_1 - \frac{1}{2\pi f C_1} \tag{4.23}$$

$$X_{g_2} = X_{L_2} + X_{C_2} = 2\pi f L_2 - \frac{1}{2\pi f C_2}. \tag{4.24}$$

The reactances in (4.23) and (4.24) are normalized by Z_0. The equivalent reactance is expressed in terms of the normalized complex reactances $X_{g_1}^{nor}$ and $X_{g_2}^{nor}$ as

$$X_D^{nor} = \frac{X_{g_1}^{nor} X_{g_2}^{nor}}{(X_{g_1}^{nor} + X_{g_2}^{nor})}. \tag{4.25}$$

then, X_D^{nor} is inserted in (4.9) and (4.10). The coefficients from Table 4.2 are used for the exponential approximations in (4.22) which are separately calculated for every ring. For the calculation of the transmission coefficient, (4.7) is used.

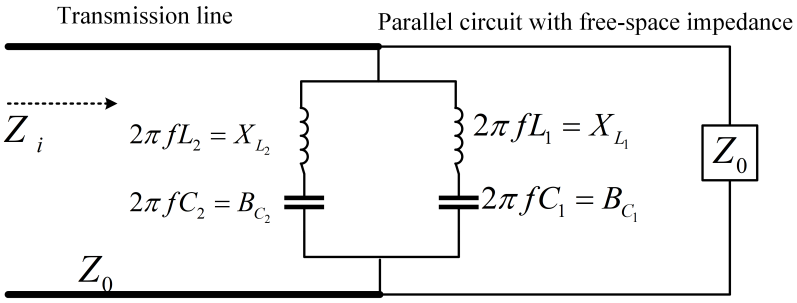

Figure 4.13 Equivalent circuit for an array of double rings in free space as a parallel circuit with free-space impedance.

4.5 Semianalytical approach for an array of double concentric rings in free space

In this section, the semianalytical and full-wave simulation results for an array of differently sized double concentric rings are compared. A distinct radius value from the interval $2.45 \leq r_{av} \leq 5.7$ (Table 4.1) is chosen. As it is seen in Figs. 4.14, 4.15, 4.16, 4.17, 4.18 and 4.19, there is a good match between the semianalytical approach and the full-wave simulation.

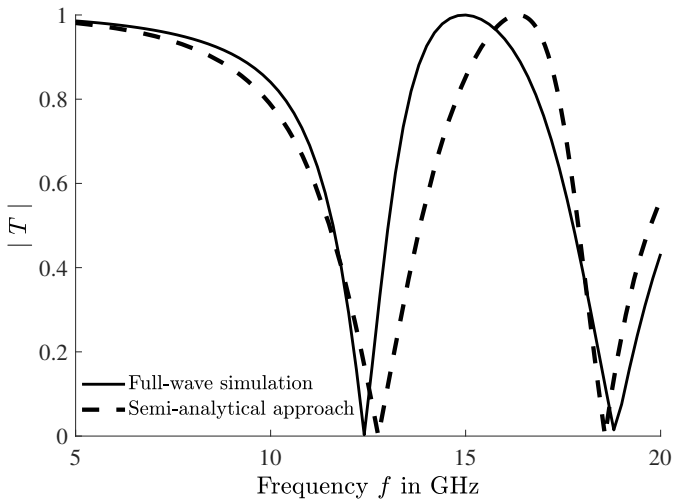

Figure 4.14 Amplitude of the transmission coefficient for an array of double rings. Outer ring: $r_{out} = 4.3$ mm and $r_{in} = 4.1$ mm; inner ring: $r_{out} = 3$ mm and $r_{in} = 2.8$ mm.

In the simulation setup, the length of the vacuumbox between the two Floquet ports is 90 mm. The iterative solver, interpolating sweep and classic mesh options are chosen in the simulation.

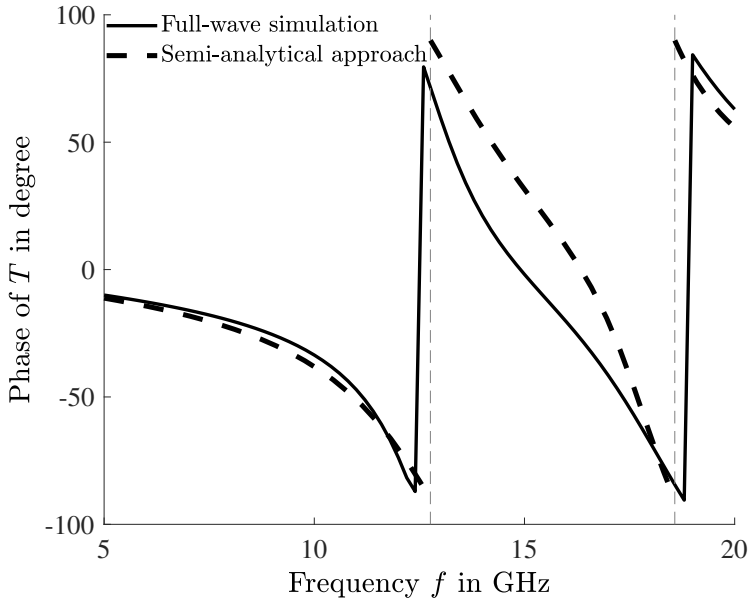

Figure 4.15 Phase of the transmission coefficient for an array of double rings. Outer ring: $r_{out} =$ 4.3 mm and $r_{in} = 4.1$ mm; inner ring: $r_{out} = 3$ mm and $r_{in} = 2.8$ mm.

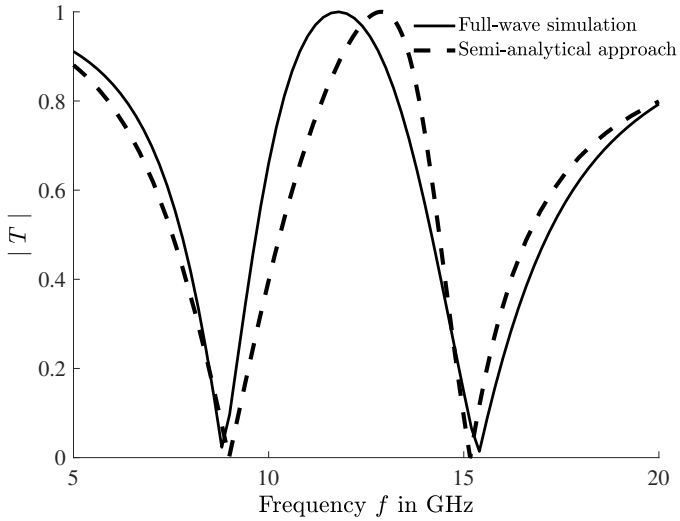

Figure 4.16 Amplitude of the transmission coefficient for an array of double rings. Outer ring: $r_{out} = 5.5$ mm and $r_{in} = 5.35$ mm; inner ring: $r_{out} = 3.7$ mm and $r_{in} = 3.5$ mm.

According to the results, it is not necessary to repeat the curve fitting to calculate the functions F_1 and F_2 and there is no need for additional full-wave simulations.

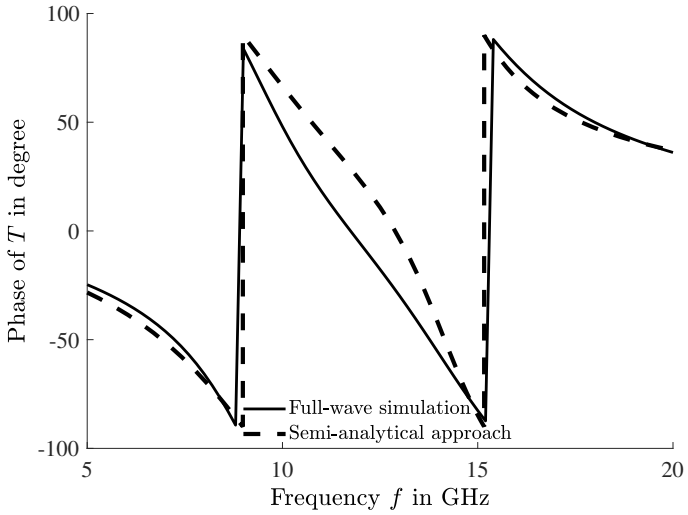

Figure 4.17 Phase of the transmission coefficient for an array of double rings. Outer ring: r_{out} = 5.5 mm and r_{in} = 5.35 mm; inner ring: r_{out} = 3.7 mm and r_{in} = 3.5 mm.

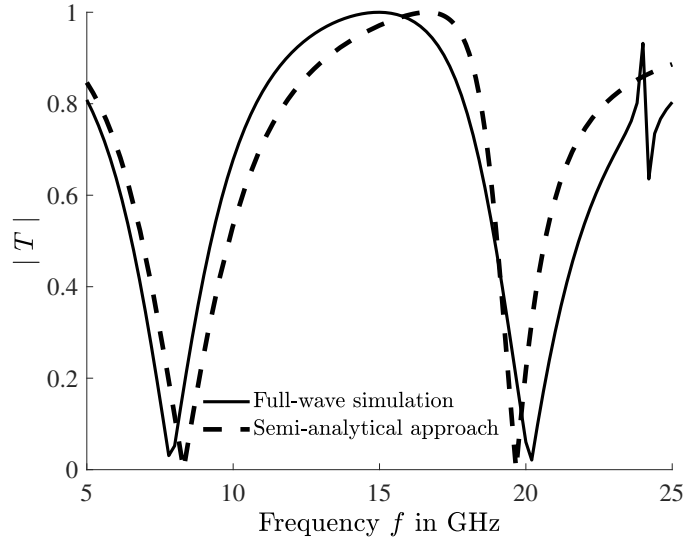

Figure 4.18 Amplitude of the transmission coefficient for an array of double rings. Outer ring: r_{out} = 5.8 mm and r_{in} = 5.6 mm; inner ring: r_{out} = 2.8 mm and r_{in} = 2.6 mm.

The estimation of the transmission coefficient is sufficiently accurate with the semianalytical approach. It is observed that the values should be in the range of radius values used in the fitting for the single ring.

When Figs. 4.14, 4.16 and 4.18 are compared, the bandwidth of the passband can be expanded by adjusting the radii of the inner and outer rings. Adjusting the radius values can also shift the position of the passband.

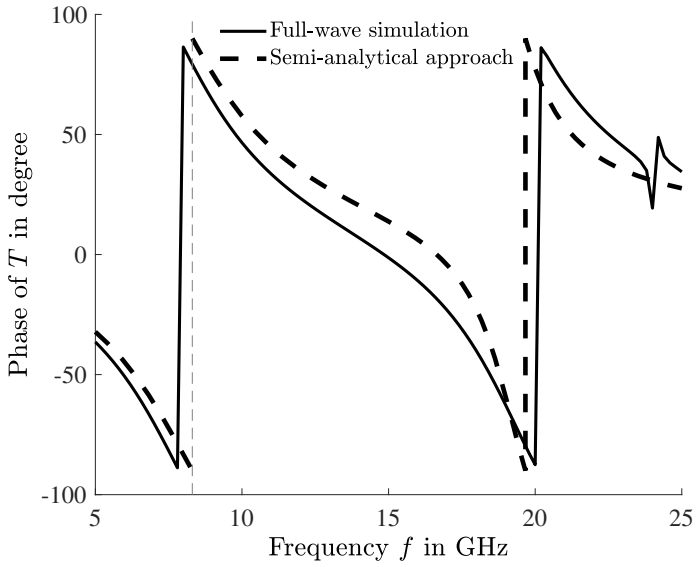

Figure 4.19 Phase of the transmission coefficient for an array of double rings. Outer ring: $r_{out} =$ 5.8 mm and $r_{in} = 5.6$ mm; inner ring: $r_{out} = 2.8$ mm and $r_{in} = 2.6$ mm.

4.6 Semianalytical approach for an array of double circular slots in a metal screen

By applying Babinet's principle, the amplitude of the transmission coefficient for the planar array of double concentric circular slots can be calculated from the amplitude of the reflection coefficient of the planar array of double concentric circular rings. The semianalytical approach described in Sections 4.1, 4.4 and 4.5 can be used to calculate the amplitude of the reflection coefficient. The result will be compared with full-wave simulation results for the infinite periodic array of double circular slots in a metal screen. The unit-cell length is 12 mm. A normally incident plane wave is considered. The length of the vacuumbox between the Floquet ports is 90 mm. The iterative solver, first-order basis functions and iterative sweep options were used.

The highest transmission through the slot array takes place at the blockage frequencies of the array of rings. By changing the radius of inner and outer rings, the position of the stopband (where the transmission is low) can be changed. The bandwidth of the stopband can be adjusted by changing the radius values as show in Figs. 4.20 and 4.21.

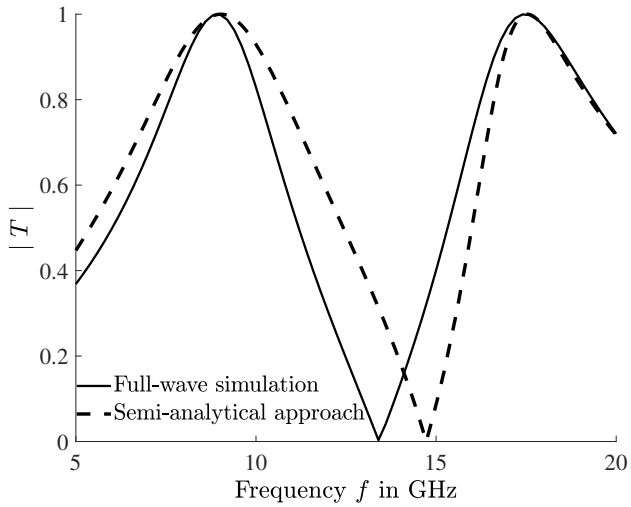

Figure 4.20 Amplitude of the transmission coefficient for the array of double circular slots. Outer ring: $r_{out} = 5.5$ mm and $r_{in} = 5.32$ mm; inner ring: $r_{out} = 3.2$ mm and $r_{in} = 3$ mm.

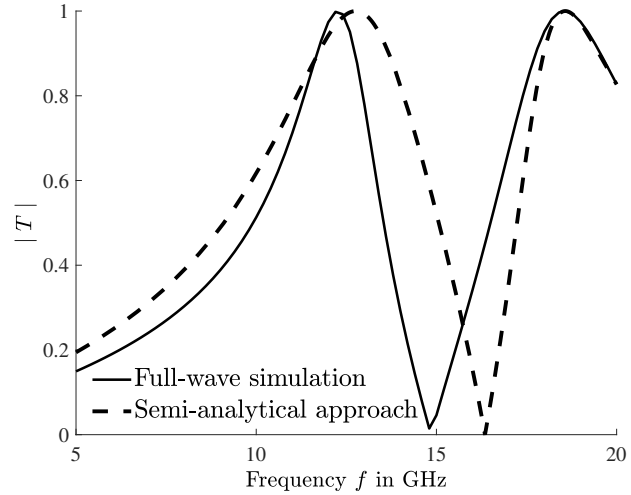

Figure 4.21 Amplitude of the transmission coefficient for the array of double circular slots. Outer ring: $r_{out} = 4.3$ mm and $r_{in} = 4.1$ mm; inner ring: $r_{out} = 3$ mm and $r_{in} = 2.8$ mm.

4.7 Transmission coefficient of an array of PEC rings on a substrate

A realistic metasheet is obtained by placing metal particles on a substrate as shown in Fig. 4.22. In this section, a corresponding extension of the semianalytical approximation is described. In the derivation, a layer of Rogers material RO3203 with the relative permittivity 3.02 and dielectric loss tangent $\tan(\delta)$ equal to 0.0016 are chosen as the substrate. This material, which has a low dielectric loss and a high mechanical stability, is suitable for high-level microwave applications

[Coredb],[Agued]. The presented approach is generic and can be used for any dielectric substrate with or without losses.

The thickness of the substrate (ℓ_2) is chosen to be 3mm. As in the Section 4.1, thin metal rings with the width between 0.1mm and 0.2mm are used, and the periodicity of the rings is 12mm. The frequency range is between 0.5 GHz and 20 GHz.

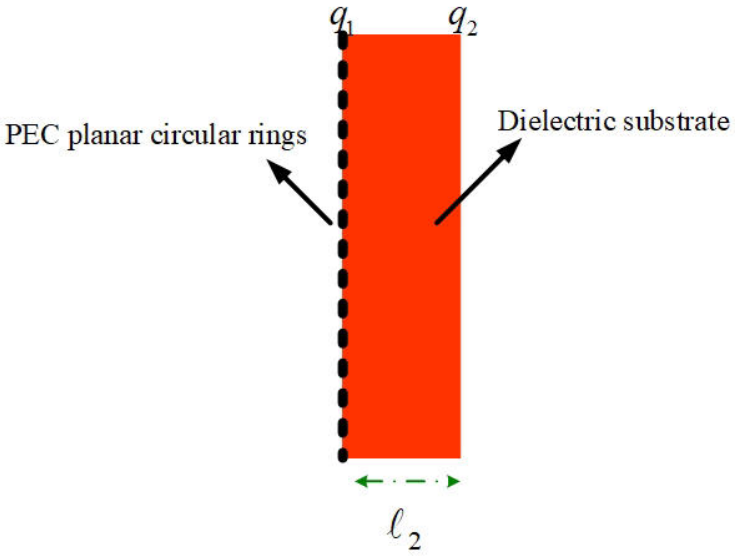

Figure 4.22 An array of planar circular rings on a dielectric substrate [zOE18] [reproduced figure courtesy of The Electromagnetics Academy].

In this study, the losses in the substrate are assumed to be small. The losses affect the propagation constant. The material of the rings is assumed to be PEC. The intrinsic impedance normalized to the free space impedance is given as

$$Z_d^{nor} = \frac{1}{\sqrt{\varepsilon_r' - j\varepsilon_r' \tan\delta}}. \tag{4.26}$$

The transmission coefficient for the structure in Fig. 4.22 can be represented as

$$T = \frac{(q_1+1)(q_2+1)e^{-k_0\ell_2(\alpha+j(\beta-1))}}{1+q_1q_2e^{-2k_0\ell_2(\alpha+j\beta)}}, \tag{4.27}$$

where $\alpha = \frac{\sqrt{\varepsilon_r'}\tan(\delta)}{2}$, and $\beta = \sqrt{\varepsilon_r'}$ [Col92], [Orfed]. The parameters q_1 and q_2 are the internal reflection coefficients at the interfaces between the array of rings and the dielectric layer and between the dielectric layer and vacuum [Col92]:

$$q_1 = \frac{Z_i - Z_d^{nor}}{Z_i + Z_d^{nor}}, \tag{4.28}$$

$$q_2 = \frac{Z_d^{nor} - 1}{Z_d^{nor} + 1}. \tag{4.29}$$

The transmission of plane waves through an infinite periodic sheet of metal rings can be described in the transmission line model by a parallel circuit of the free-space impedance Z_0 and a reactance X_g. The impedance Z_i of the equivalent circuit describes the behaviour of the plane wave in vacuum and an infinite periodic array of metal rings. Thus, there are only two transitions left, into the dielectric layer of finite thickness and into free-space. Equation (4.27) converts into (4.7) when the thickness of the dielectric substrate becomes 0. The lumped elements of the same type as in Section 4.1 are used to describe the equivalent impedance Z_i of the infinite periodic planar array of circular rings on the dielectric substrate. Full-wave simulations have been conducted for 5 different radius values shown in Table 4.3. The same simulation setup as in Section 3.5 is applied here. The length of the vacuumbox between the two Floquet ports for the simulation is 150 mm. The direct solver, mixed order basis functions, and interpolating sweep were used. In one of the simulations, the iterative solver was used.

In Fig. 4.23, the full-wave simulation results for the amplitude of the transmission coefficient for the largest (5.7 mm) and the smallest (2.7 mm) radius values are shown. The free parameters F_1 and F_2 in (4.16) are fitted to the full-wave simulation results for the amplitude of the transmission coefficient in (4.27). This yields the values for F_1 and F_2 as given in Table 4.3.

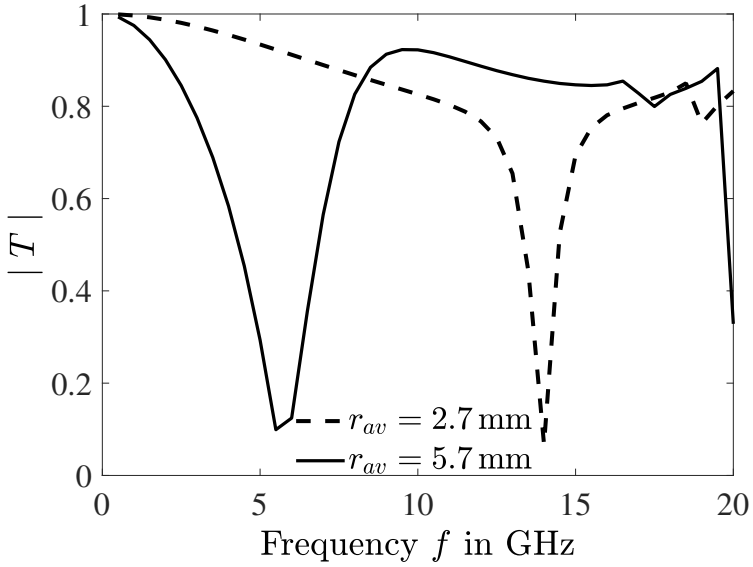

Figure 4.23 Full-wave simulated amplitude of the transmission coefficient of an array of circular rings on RO3203 substrate for the largest and smallest radius values [zOE18] [reproduced figure courtesy of The Electromagnetics Academy].

Table 4.3 Curve fitting for arrays of circular rings on RO3203 substrate [zOE18] [reproduced table courtesy of The Electromagnetics Academy].

r_{av} in mm	F_1	F_2	$F_3 = \frac{F_2}{F_1}$
2.7	0.6958	8.546	12.2823
3.5	0.4683	3.617	7.7237
4.45	0.427	1.915	4.4848
4.9	0.3804	1.385	3.6409
5.7	0.3923	0.8109	2.0670

The presence of the substrate leads to a higher sensitivity of the resonance frequency with respect to the parameters F_1 and F_2. By analyzing (4.27), the same relation as in (4.21) holds for the resonance (blockage) frequency

$$k_{nor}^2 = \frac{F_2}{F_1}. \tag{4.30}$$

A new parameter F_3 defined by

$$F_3 = \frac{F_2}{F_1} \tag{4.31}$$

is introduced to make sure that deviations in the following fitting process affect the resonance frequency to a minimal extend. By looking at the calculated values of the functions F_1 and F_3 in Figs. 4.24 and 4.25, the exponential approximations can be proposed.

$$\begin{aligned} F_1(r_{nor}) &= a_1 e^{(b_1 r_{nor})} + c_1 e^{(d_1 r_{nor})} \\ F_3(r_{nor}) &= a_3 e^{(b_3 r_{nor})} + c_3 e^{(d_3 r_{nor})}, \end{aligned} \tag{4.32}$$

A fitting with (4.32) in the Matlab curve fitting tool is done on the data in Table 4.3 to yield the values of the free coefficients a, b, c, and d as given in Table 4.4. F_2 can then be calculated from (4.31).

The susceptance, which is affected by the dielectric substrate, causes the change of the resonance frequency of the array of metal planar particles and the change of the bandwidth of the stop-band region [CPL91]. If the material and/or thickness of the substrate change, fitting should be repeated.

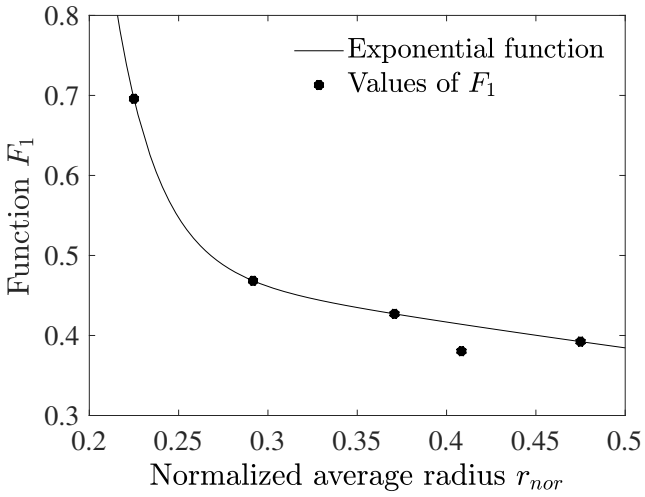

Figure 4.24 Fitting quality of the exponential function at the specific values of F_1 [zOE18] [reproduced figure courtesy of The Electromagnetics Academy].

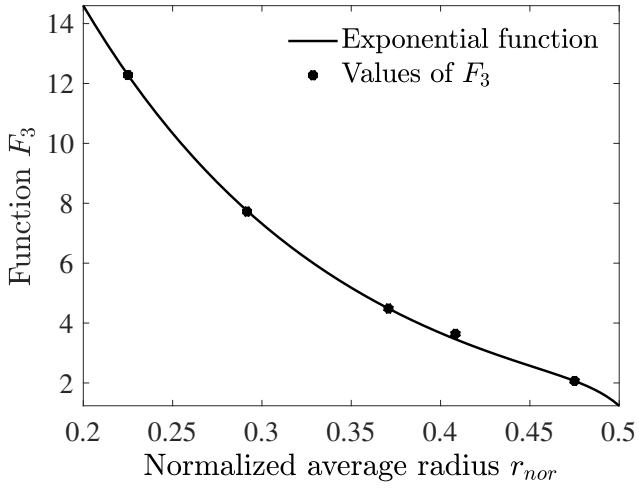

Figure 4.25 Fitting quality of the exponential function at the specific values of F_3 [zOE18] [reproduced figure courtesy of The Electromagnetics Academy].

Table 4.4 Coefficients in the exponential function [zOE18] [reproduced table courtesy of The Electromagnetics Academy].

Coefficients	F_1	F_3
a	2298	58.12
b	-41.2	-6.908
c	0.5742	-3.963×10^{-15}
d	-0.8019	65.3

4.8 Semianalytical approach and full-wave simulations for an array of rings on substrate

The substrate RO3203 with thickness 3 mm is used. The thickness of the rings is 18 μm. The unit-cell length is equal to 12 mm. The radius values are chosen in the range $2.7\,\text{mm} \leq r_{av} \leq 5.7\,\text{mm}$ as given in Table 4.3.

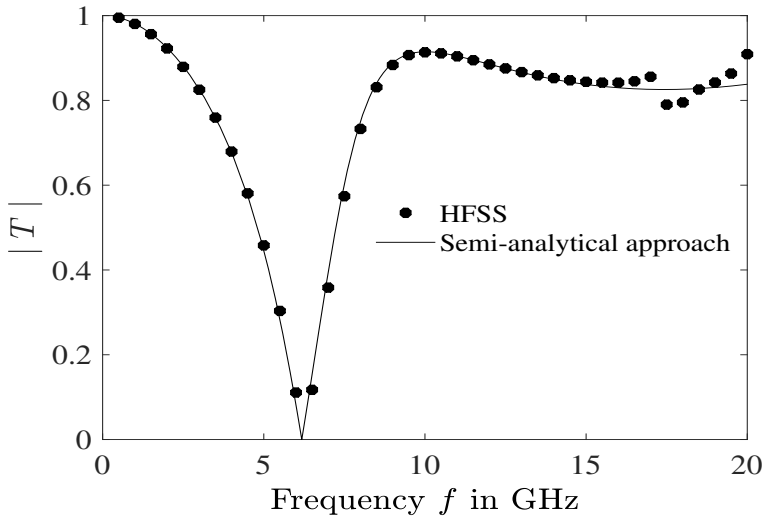

Figure 4.26 Amplitude of transmission coefficient of an array of copper rings ($r_{out} = 5.6\,\text{mm}$, $r_{in} = 5.4\,\text{mm}$ and $p = 12\,\text{mm}$) on the substrate.

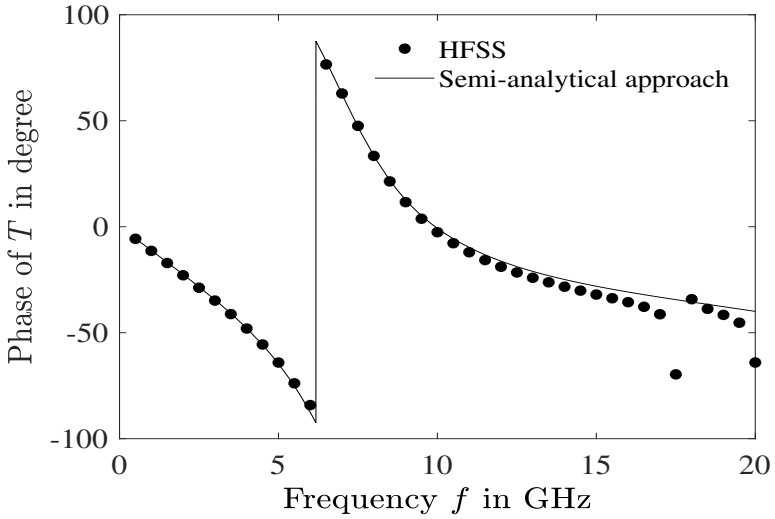

Figure 4.27 The same as in Fig. 4.26 but for the phase.

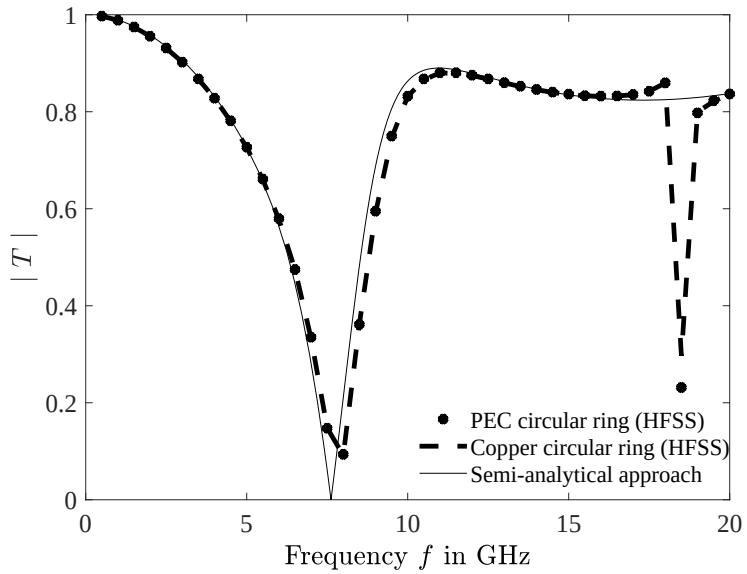

Figure 4.28 Amplitude of the transmission coefficient of an array of rings ($r_{out} = 4.9$mm, $r_{in} = 4.7$mm and $p = 12$mm) on the substrate [zOE18] [reproduced figure courtesy of The Electromagnetics Academy].

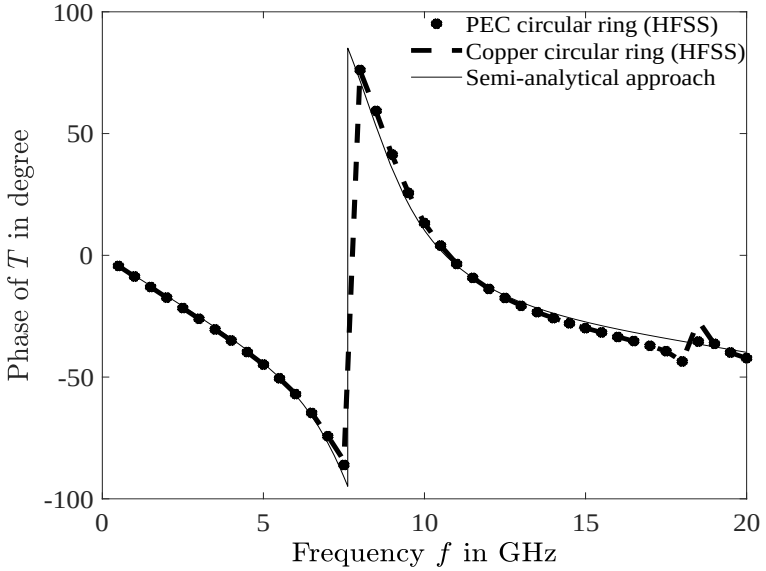

Figure 4.29 The same as in Fig. 4.28 but for the phase [zOE18] [reproduced figure courtesy of The Electromagnetics Academy].

The radius values should be in the range where the fitting is done. When the radius values are increased, the resonance frequency decreases. The shift of the resonance frequency is observed in the results. It is seen that using copper instead of PEC for the rings does not make any difference

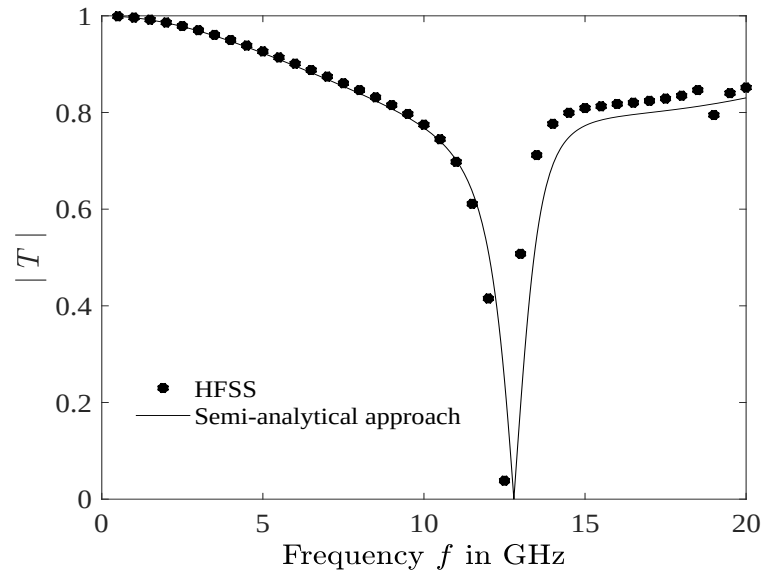

Figure 4.30 Amplitude of transmission coefficient of array of copper rings ($r_{out} = 3.05\,\text{mm}$, $r_{in} = 2.95\,\text{mm}$ and $p = 12\,\text{mm}$) on the substrate [zOE18] [reproduced figure courtesy of The Electromagnetics Academy].

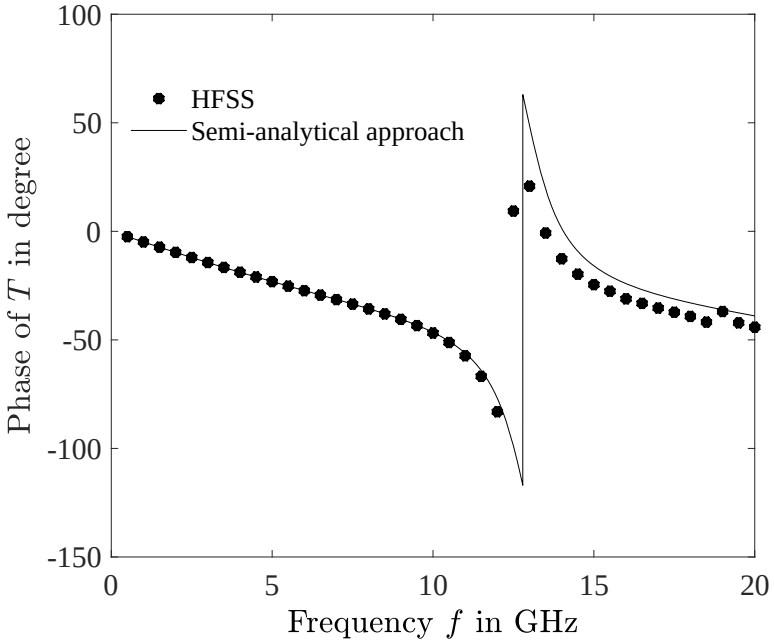

Figure 4.31 The same as in Fig. 4.30 but for the phase [zOE18] [reproduced figure courtesy of The Electromagnetics Academy].

in the simulation results Figs. 4.28 and 4.31. There is a good match in the calculated and full-wave simulated results from Fig. 4.26 to Fig. 4.31.

4.9 Comparison of the results of the semianalytical approach with measurements

In this section, measurement and semianalytical approach results are compared for two metasheets both based on FR4 epoxy with two different copper ring sizes. A predefined value $\varepsilon_r = 4.4$ from the HFSS list of material parameters was used. A normally incident plane wave is considered [zOE18]. Table 4.5 shows the obtained coefficients by semianalytical approach. The manufactured metasheets are shown in Figs. 4.32 and 4.33. The periodicity is 12 mm, the thickness of the substrate is 2 mm and the thickness of the ring is 0.018 mm.

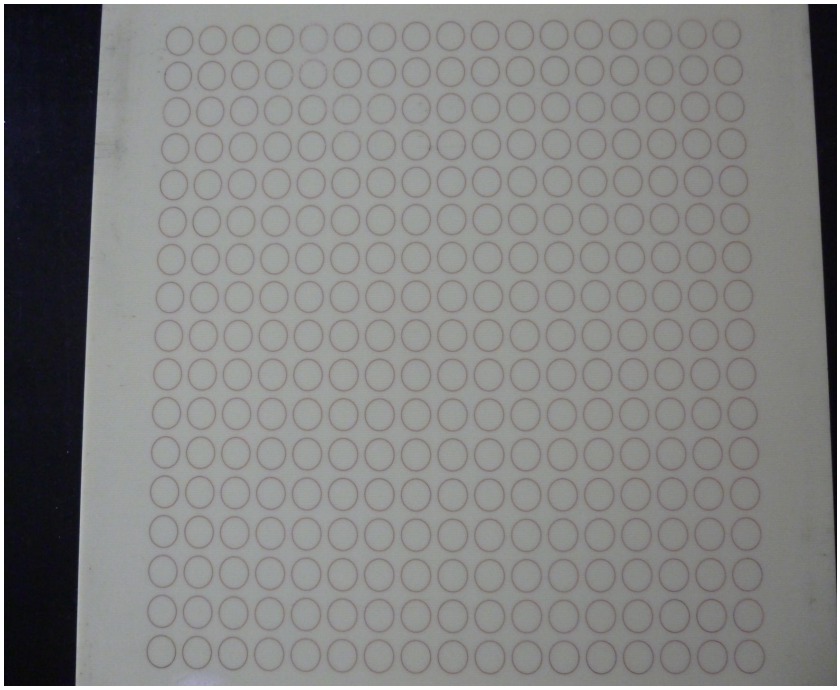

Figure 4.32 Manufactured metasheet: copper rings with $r_{out} = 4.9$ mm, $r_{in} = 4.7$ mm on an FR4 plate of the size 250 mm×250 mm.

The transmission coefficient was measured in a free-space measurement facility shown in Fig. 4.34. The metasheet platine whose size is 25 cm × 25cm, is positioned between the transmit and receive antennas. The amplitude and phase of S_{21} are measured. The electronic equipments to do this measurements are a vector network analyzer (VNA) Anritsu, a controller (Huber) and computer (PC).

FR4-epoxy is a cheaper material than RO3203 and thus used more frequently. FR4 has a higher dissipation factor in comparison with other high frequency laminates [Coo11]. High-frequency laminates typically have a stable dissipation factor characteristic. In applications, where losses

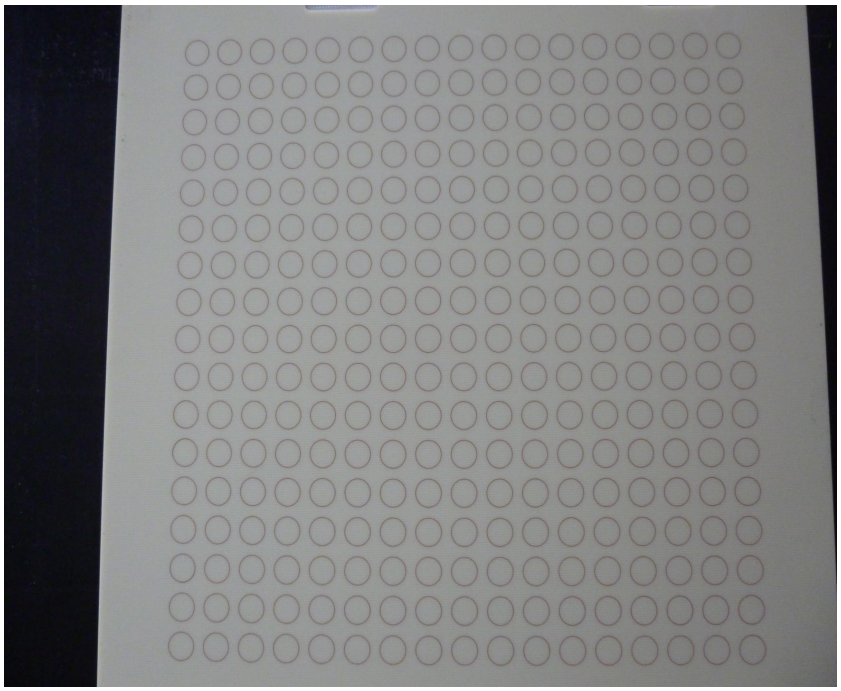

Figure 4.33 Manufactured metasheet: copper rings with $r_{out} = 4.42\,\text{mm}$, $r_{in} = 4.26\,\text{mm}$ on an FR4 of the size 250 mm×250 mm.

are not critical, FR4 can be preferred and it also has a good reliability characteristic. FR4 materials, which are well proven and their performance is well known, are used generally in many PCB applications [Coo11]. The same fitting process, what is explained in Section 4.7, is applied. The substrate is different from Section 4.7, so the fitting must be repeated. The coefficients for the functions F_1 and F_3 in (4.32) are calculated by fitting.

The values of r_{av} used in the fitting are 2.7mm, 3.5mm, 4.45mm, 4.9mm, 5.7mm. The results of the simulations are presented in Figs. 4.35- 4.38. A good match is observed between the measurements and the semianalytical approach. With this, the relative error for the ring with $r_{out} = 4.9\,\text{mm}$ and $r_{in} = 4.7\,\text{mm}$ is found to be 2.4% and for the ring with $r_{out} = 4.42\,\text{mm}$ and $r_{in} = 4.26\,\text{mm}$, to be 3.25%. The relative error in the resonance frequency can be estimated as

$$Error = \frac{|f_{measurement} - f_{semianalytical}|}{f_{measurement}} \cdot 100\%. \tag{4.33}$$

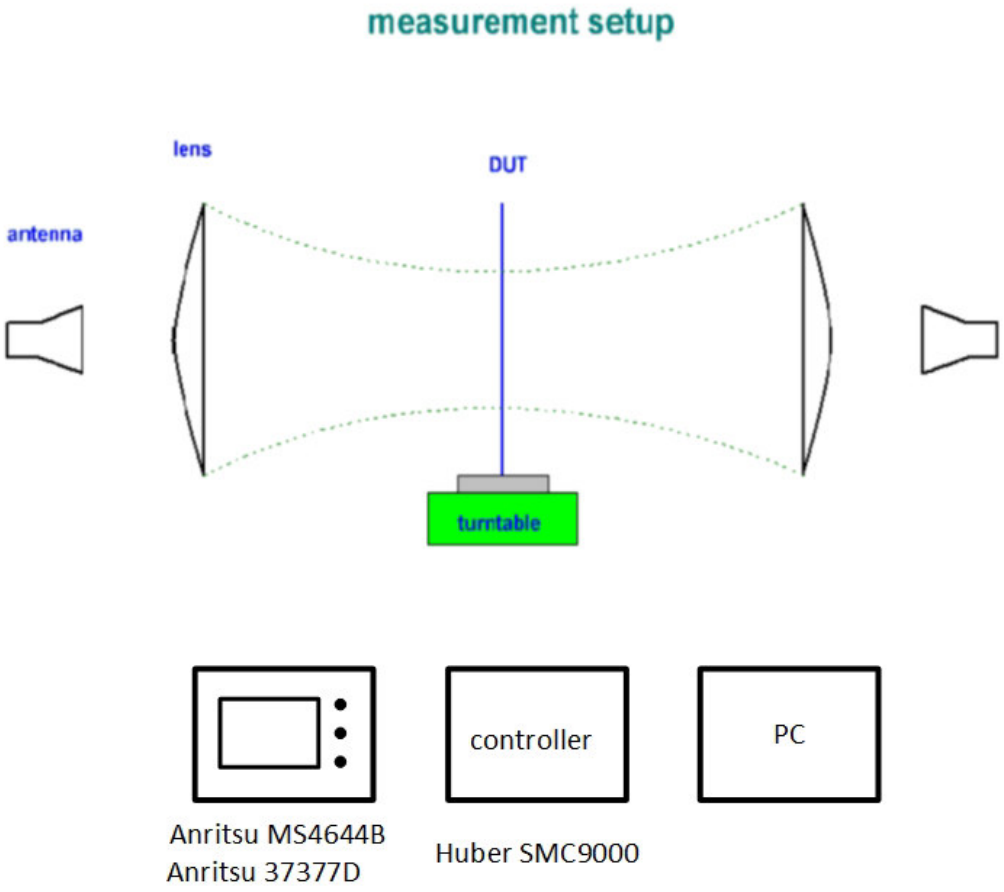

Figure 4.34 Free-space transmission measurement setup (DLR Techlab)

Table 4.5 Coefficients in exponential approximations [zOE18] [reproduced table courtesy of The Electromagnetics Academy].

Coefficients	F_1	F_3
a	1.074	43.3
b	-2.383	-6.758
c	0	0
d	-150.5	-107.5

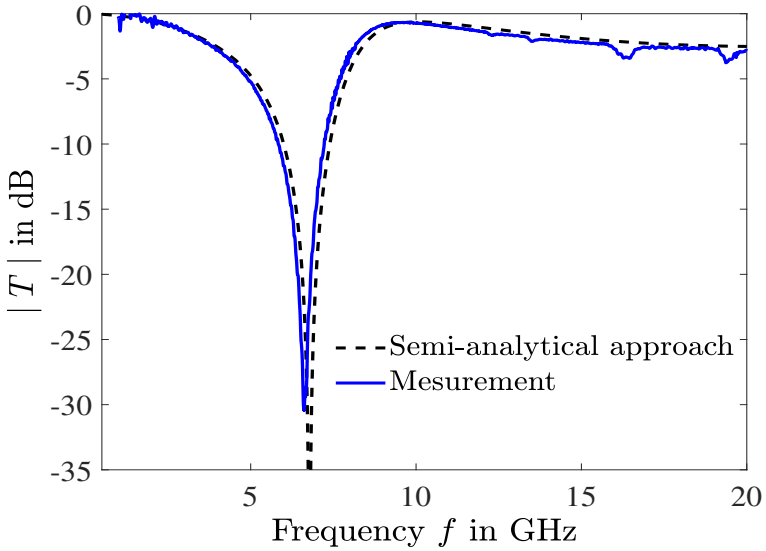

Figure 4.35 Comparison of semianalytical and measurement results for the ring size $r_{out} = 4.9\,\text{mm}$, $r_{in} = 4.7\,\text{mm}$ [zOE18] [reproduced figure courtesy of The Electromagnetics Academy].

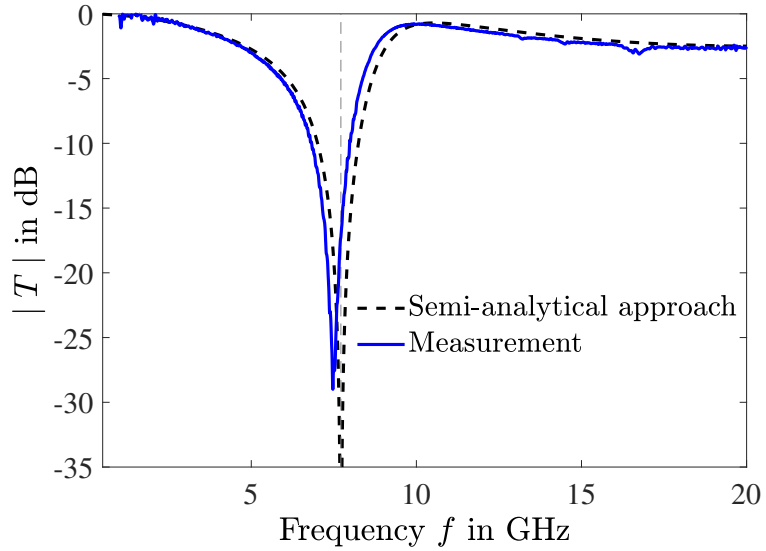

Figure 4.36 The same as Fig. 4.35 for the ring size $r_{out} = 4.42\,\text{mm}$, $r_{in} = 4.26\,\text{mm}$ [zOE18] [reproduced figure courtesy of The Electromagnetics Academy].

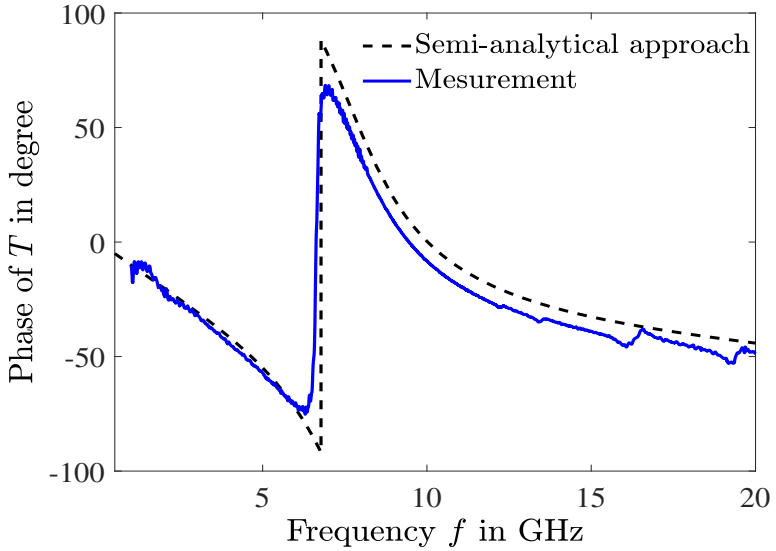

Figure 4.37 The same as Fig. 4.35 but for the phase [zOE18] [reproduced figure courtesy of The Electromagnetics Academy].

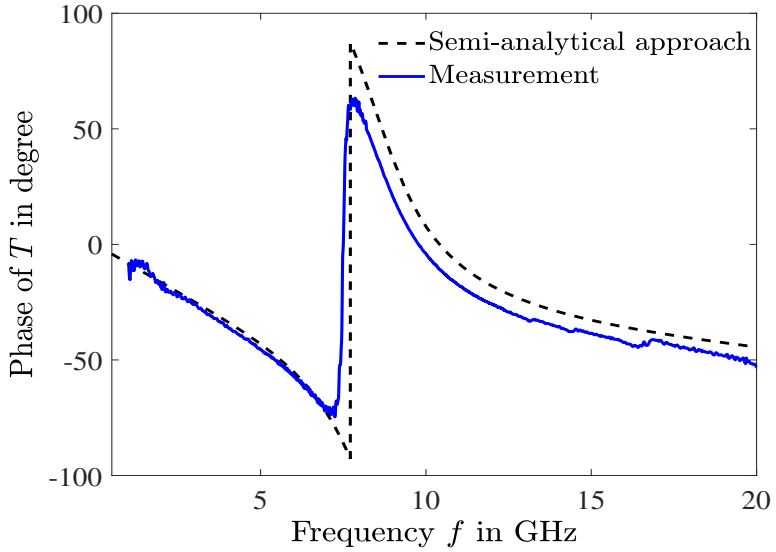

Figure 4.38 The same as Fig. 4.37 for the ring size $r_{out} = 4.42\,\text{mm}$, $r_{in} = 4.26\,\text{mm}$ [zOE18] [reproduced figure courtesy of The Electromagnetics Academy].

4.10 Extended semianalytical approach for an array of circular rings on substrate

In this section, the semianalytical approach is extended to include two parameters (outer radius and width) of the rings Fig. 3.2. The approach will be used to design the metalens for a hemispheric radome in Section 6.8. The same process as in Section 4.7 is followed but for calculating the coefficients of the exponential functions F_1 and F_3, surface fitting is done. To include an additional parameter, the exponential functions F_1 and F_3 in (4.32) should be modified by assuming that the coefficients b_1, d_1, b_3, d_3 are not constant.

The dielectric substrate is Megtron6. The frequency range is between 18 GHz and 46 GHz. A normally incident linearly polarized plane wave is considered. To have a better information about the relative permittivity of the substrate, the sample was characterized with the waveguide transmission/reflection method in the material characterization facilities in the DLR Techlab in Oberpfaffenhofen and it is observed that the relative permittivity is changing between 3.6 and 3.8 at different positions on the dielectric substrate. This shows that there is a microstructural heterogeneity, and the size of inhomogeneous parts on the substrate come closer to the wavelength when the frequency increases. To analyze this unstable behavior more deeply, another Megtron 6 with thickness 2 mm has been ordered and its reflection coefficient has been measured in the free space measurement facility (Techlab, DLR, Oberpfaffenhofen)(the relative permittivity is determined from the measured reflection coefficient). Then, the infinite periodic planar dielectric substrate simulation is done in HFSS.

The best match between the simulated and measured reflection coefficient is achieved with relative permittivity 4.33 and loss tangent 0.006 (Fig. 4.39). This value of permittivity is used in the extended semianalytical approach.

The width of a ring is normalized to the unit-cell size as

$$w_{nor} = \frac{w}{p} \tag{4.34}$$

These coefficients are written in terms of the functions [zOE20]

$$\begin{aligned} F_1(r_{nor}, w_{nor}) &= a_1 e^{(b_1(w_{nor})r_{nor})} + c_1 e^{(d_1(w_{nor})r_{nor})} \\ F_3(r_{nor}, w_{nor}) &= a_3 e^{(b_3(w_{nor})r_{nor})} + c_3 e^{(d_3(w_{nor})r_{nor})}. \end{aligned} \tag{4.35}$$

The parameters b_1, d_1, b_3 and d_3 in (4.35) are expanded in Taylor series with respect to w_{nor}. The approximation should be kept as simple as possible. Therefore, higher orders of the Taylor series

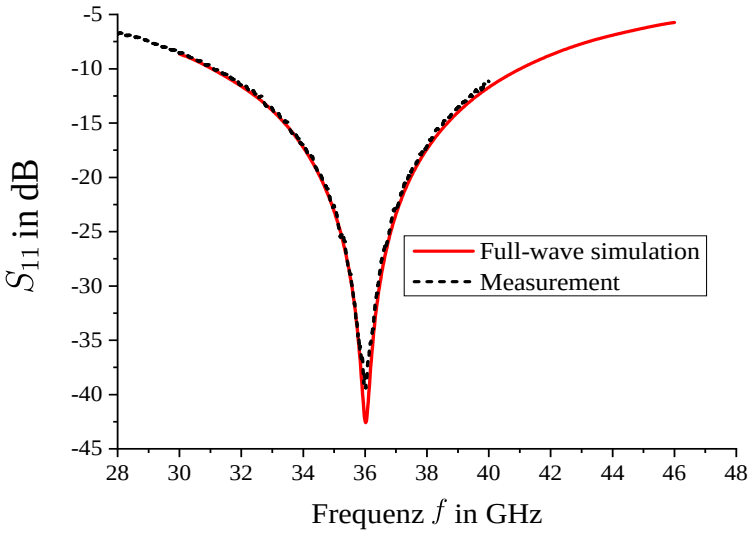

Figure 4.39 Reflection coefficient of the Megtron 6 substrate: free-space measurement vs. full-wave simulation.

are not used in order to reduce the complexity of the calculation. It will be seen that keeping first two terms in the Taylor series provides enough accuracy. Upon the Taylor series approximation, (4.35) becomes [zOE20]

$$F_1(r_{nor}, w_{nor}) = a_1 e^{(b_{11} r_{nor} + b_{12} r_{nor} w_{nor})} + c_1 e^{(d_{11} r_{nor} + d_{12} r_{nor} w_{nor})}$$
$$F_3(r_{nor}, w_{nor}) = a_3 e^{(b_{31} r_{nor} + b_{32} r_{nor} w_{nor})} + c_3 e^{(d_{31} r_{nor} + d_{32} r_{nor} w_{nor})}, \tag{4.36}$$

where b_{11}, b_{12}, d_{11}, d_{12}, b_{31}, b_{32}, d_{31}, d_{32} are coefficients of the modified exponential approximation. To determine the coefficients, four different width values 0.1 mm, 0.13 mm, 0.16 mm and 0.19 mm are chosen. For each width value, the same outer radius values 0.9 mm, 1 mm, 1.1 mm, 1.2 mm and 1.3 mm are used. According to the different width values, the inner radii of the rings are changed. The unit-cell length is 3 mm. The thickness of the ring and the thickness of the substrate are 0.018 mm and 2 mm, respectively. The width of the rings is between 0.1 mm and 0.19 mm. The vacuumbox length for the simulation of the infinite periodic array of the rings on the substrate is 50 mm. In the simulation setup, first order basis functions, iterative solver, interpolating sweep and classic mesh model were chosen.

For the calculation of F_1 and F_2 for each radius, line fitting is done on the full-wave simulated amplitude of transmission coefficient. The results are shown in the Tables from 4.6 to 4.9.

Table 4.6 F_1 and F_2 for each value of the radius of the ring with the width 0.1 mm [zOE20] [reproduced table courtesy of The Electromagnetics Academy].

r_{in} in mm	F_1	F_2
1.2	0.3151	0.8407
1.1	0.334	1.126
1	0.3653	1.531
0.9	0.4067	2.099
0.8	0.4668	2.952

Table 4.7 F_1 and F_2 for each value of the radius of the ring with the width 0.13 mm [zOE20] [reproduced table courtesy of The Electromagnetics Academy].

r_{in} in mm	F_1	F_2
1.17	0.2936	0.8261
1.07	0.313	1.109
0.97	0.3415	1.507
0.87	0.3809	2.065
0.77	0.4375	2.892

Table 4.8 F_1 and F_2 for each value of the radius of the ring with the width 0.16 mm [zOE20] [reproduced table courtesy of The Electromagnetics Academy].

r_{in} in mm	F_1	F_2
1.14	0.2749	0.806
1.04	0.2936	1.093
0.94	0.3205	1.484
0.84	0.3587	2.036
0.74	0.4135	2.859

Table 4.9 F_1 and F_2 for each value of the radius of the ring with the width 0.19 mm [zOE20] [reproduced table courtesy of The Electromagnetics Academy].

r_{in} in mm	F_1	F_2
1.11	0.2588	0.7958
1.01	0.2777	1.086
0.91	0.3018	1.466
0.81	0.3397	2.022
0.71	0.3918	2.83

The values of F_3 are calculated from the values of F_1 and F_2 by using the ratio in (4.31). The values of F_1 and F_3 are written as matrix, then surface fitting is done on these two matrices as shown in Fig. 4.40 and 4.41 to calculate the coefficients in (4.36).

As it is observed in Figs. 4.40 and 4.41, the result of surface fitting is accurate enough. The calculated coefficients in (4.36) are shown in Tables 4.10 and 4.11.

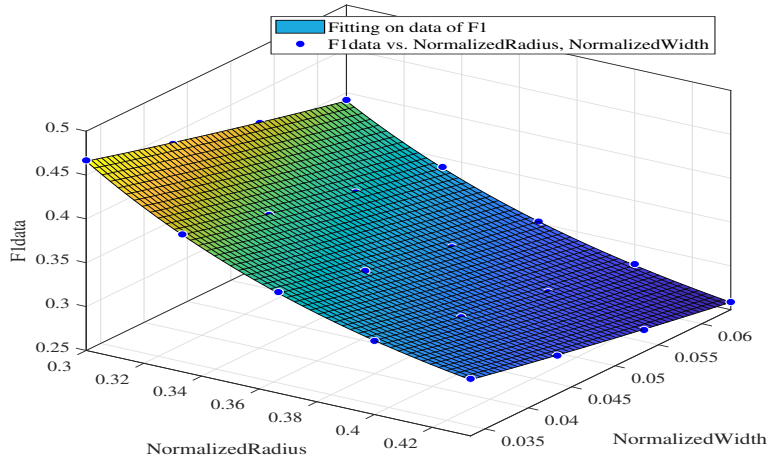

Figure 4.40 Surface fitting (WidthN - the normalized width, RoutN - the normalized outer radius) on the F_1 matrix [zOE20] [reproduced figure courtesy of The Electromagnetics Academy].

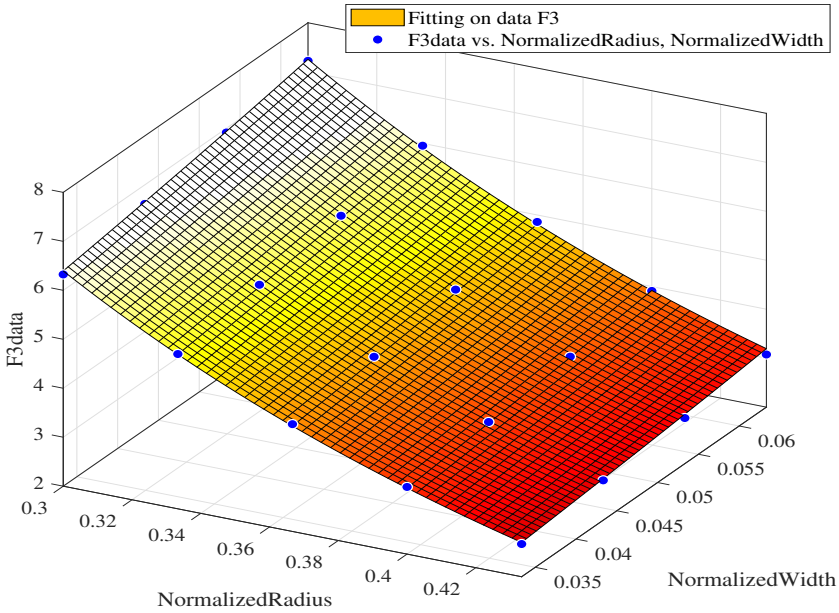

Figure 4.41 Surface fitting (WidthN - the normalized width, RoutN - the normalized outer radius) on the F_3 matrix [zOE20] [reproduced figure courtesy of The Electromagnetics Academy].

Table 4.10 Calculated coefficients of F_1 function by applying surface fitting [zOE20] [reproduced table courtesy of The Electromagnetics Academy].

Coefficients	F_1
a_1	0.1991
c_1	4.064
b_{11}	0.9071
b_{12}	−11.92
d_{11}	−8.595
d_{12}	−27.69

Table 4.11 Calculated coefficients of F_3 function by applying surface fitting [zOE20] [reproduced table courtesy of The Electromagnetics Academy].

Coefficients	F_3
a_3	43.19
c_3	3.754
b_{31}	−6.789
b_{32}	11.41
d_{31}	−17.06
d_{32}	128.1

4.11 Extended semianalytical approach vs. full-wave simulations for an array of rings

Four different width values are chosen. For the results presented in Figs. 4.42 to 4.45, the width values that are not used in the fitting, the outer radius values that are used in the fitting are chosen. In Figs. 4.46 and 4.49, both the width and outer radius values are chosen which are not used in the fitting. It is evident that the simulated and calculated results match well. It is observed that the transmission coefficient can be estimated better by including the width as a dimensional parameter.

When the radius values increase, the resonance frequency decreases or vice versa. The shift of the resonance frequency is clearly seen by comparing Figs. 4.42 and 4.44. The radius value in Fig. 4.48 is between the radius values in Fig 4.42 and 4.44; therefore the resonance frequencies

are positioned accordingly. The fine tuning of the resonance frequency can be done by including the combination of the width and the radius.

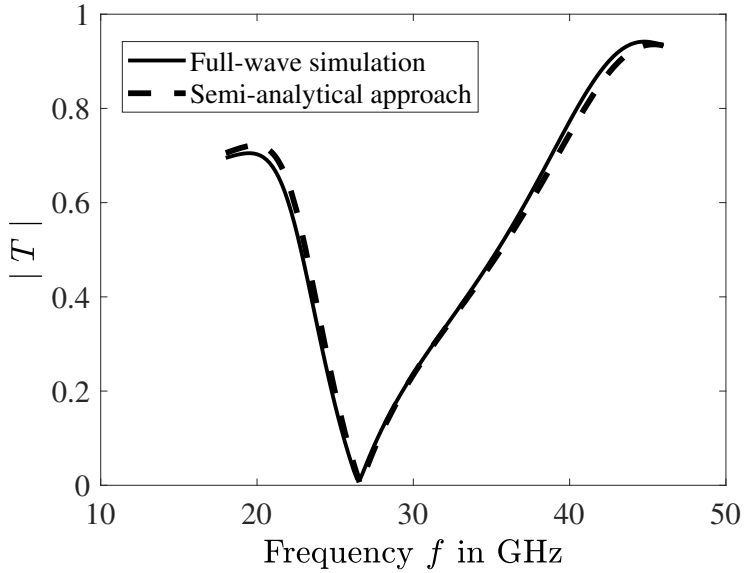

Figure 4.42 Amplitude of the transmission coefficient of an array of rings ($r_{out} = 1.3$mm, $r_{in} = 1.18$mm and $p = 3$mm) on the substrate.

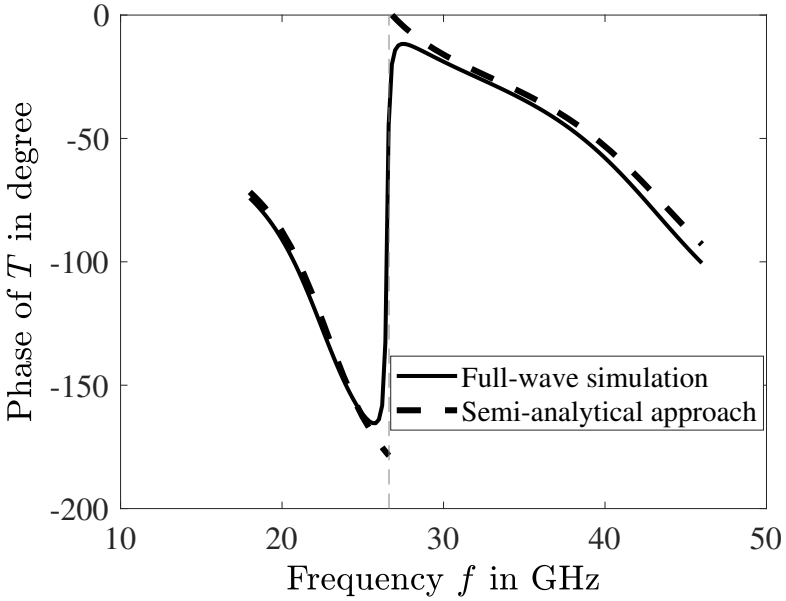

Figure 4.43 The same as in Fig. 4.42 but for the phase.

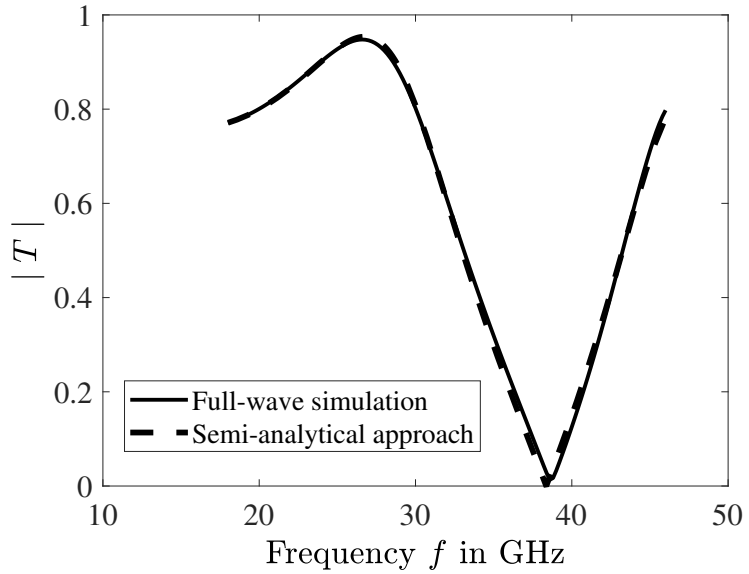

Figure 4.44 Amplitude of the transmission coefficient of an array of rings ($r_{out} = 1\,\text{mm}$, $r_{in} = 0.82\,\text{mm}$ and $p = 3\,\text{mm}$) on the substrate.

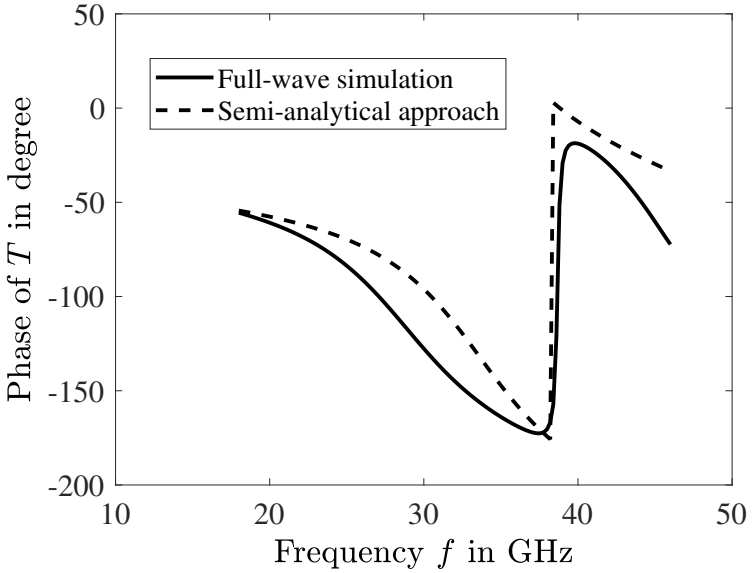

Figure 4.45 The same as in Fig. 4.44 but for the phase.

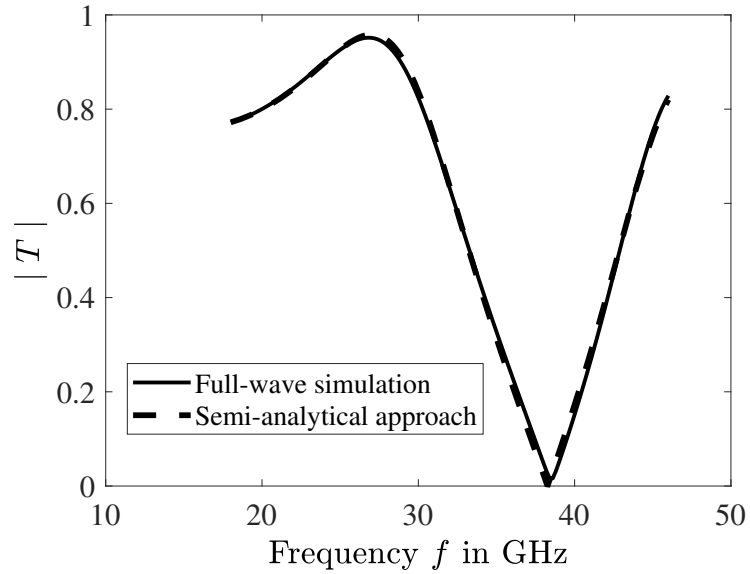

Figure 4.46 Amplitude of the transmission coefficient of array of rings ($r_{out} = 0.98$mm, $r_{in} = 0.83$mm, and $p = 3$mm) on the substrate.

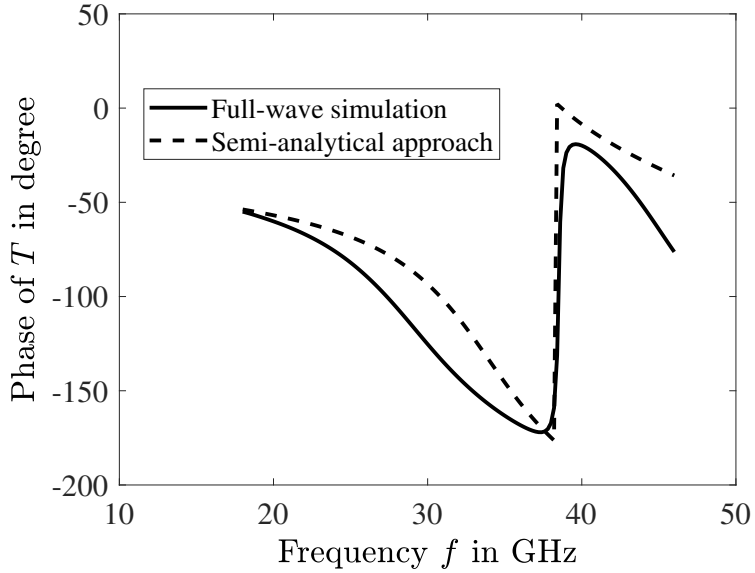

Figure 4.47 The same as in Fig. 4.46 but for the phase.

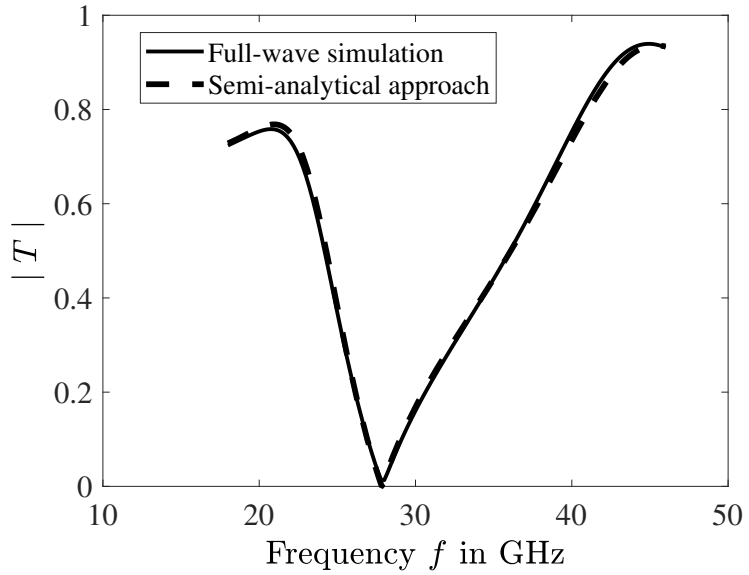

Figure 4.48 Amplitude of the transmission coefficient of an array of rings ($r_{out} = 1.25\,\text{mm}$, $r_{in} = 1.14\,\text{mm}$ and $p = 3\,\text{mm}$) on the substrate.

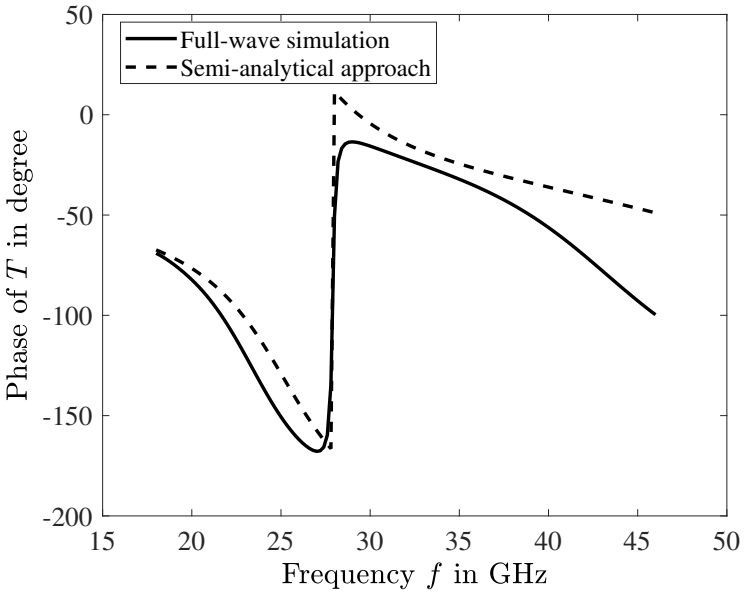

Figure 4.49 The same as in Fig. 4.48 but for the phase.

Chapter 5

Physical Optics for Transmission through Electrically Large Planar Metasheets

5.1 Concept of Physical Optics

Physical Optics (PO) is a well known high-frequency approach to calculate the radiated and scattered electromagnetic fields at an arbitrary observation point. This method is an approximation because it assumes that the scattered field can be calculated by integration of a simplified current distribution (deduced by application of geometrical optics) over the scattering surface. The radiated field can be found from the distribution of electric and magnetic currents. In the estimation of the magnitude of the backscattered field or the level of the main lobe in the directivity diagram of an antenna, the PO approach is useful and convenient [OT17], [Ufi08]. The electromagnetic version of the PO method was introduced by MacDonald in his study of scattering for perfectly absorbing bodies [Mac12].

The computational cost of PO calculations mainly depends on the electrical size of the scatterer. When the size of the scatterer increases, the computational cost becomes heavier. The other reasons for the computational cost are the number of observation points and frequency sampling points [KA13]. For decreasing the computational cost, Fast Physical Optics and Multilevel Physical Optics are studied in [Boa04], [BL05a].

The calculation of scattering from electrically large structures is a difficult problem for full-wave simulations with finite-element methods. For having an acceptable accuracy in the calculation, meshing should be dense and the number of unknowns becomes high. High-frequency approximation algorithms are adequate and applicable to electrically large structures. The available full-wave simulations are mainly utilized for electromagnetic scattering problems.

The available numerical methods for full-wave simulations are insufficient when the size of the scatterer increases, due to the fact that their computational complexity grows as fast as $O(N^2)$, where N shows the total number of facets on the scatterer [LG17]. Therefore, alternative methods are needed to calculate the scattered field. Physical Optics can be an alternative method. The accuracy of PO grows when the size of the scatterer is increased. The electrically or magnetically conducting scatterers, dielectric materials and scatterers with surface impedance can be analyzed. With PO, the main difficulty in the calculation can be the approximation of the induced currents when there are several reflections or when the curvature of the scatterer increases [HLW]. The induced currents on the surface of the scatterer in PO calculations are approximately computed by using boundary conditions and Fresnel formulas [LG17], [Pat88].

With growing frequency, the PO integral oscillates stronger and the rate of oscillations increases.The vector fields can be computed with this approach. In PO calculation, the surface is assumed to be locally planar then the reflection and transmission are calculated as determined by Geometrical Optics (GO) [HLW].

For the calculation of the scattered field, the integration of the induced currents on the electrically large surface is necessary and the induced currents cannot be calculated exactly; therefore, induced currents on the surface should be replaced by equivalent currents [Col60]. The equivalent currents are defined by tangential electric and magnetic field components on the surface. PO calculates the equivalent currents according to GO rules. As a result, Physical Optics becomes a combination of GO and the field equivalence principle.

5.2 Geometrical Optics

Geometrical Optics is a high-frequency approximation which assumes energy propagating in tubes of infinitesimal cross section, or rays [BW99], [Han64], [Sam84]. In Geometrical Optics, equiphase surfaces and rays are considered. If permittivity and permeability of a medium are not functions of position, the medium is named as homogeneous. If the material parameters depend on position, then the medium is non-homogeneous. In a homogeneous medium, every ray is a straight line. In a non-homogeneous medium, the rays become curved. When a ray moves into a medium with a higher value of the index of refraction, it bends toward that region [Cha88]. The gradient of the phase is directed along the ray, and the polarization of the field is conserved along a ray. The Luneberg-Kline series is considered as the foundation of Geometrical Optics [Lah16]. The series can be constructed by Maxwell's equations. The ray can be defined by a path between the source and the observation point. The amplitude and phase along the path are calculated by

using the laws of Geometrical Optics. A ray incident on a material boundary generates a reflected ray and a transmitted ray. Geometrical Optics calculations depend on Snell's law for reflection and transmission at the surface separating two media (Fig. 5.1) [JRM55].

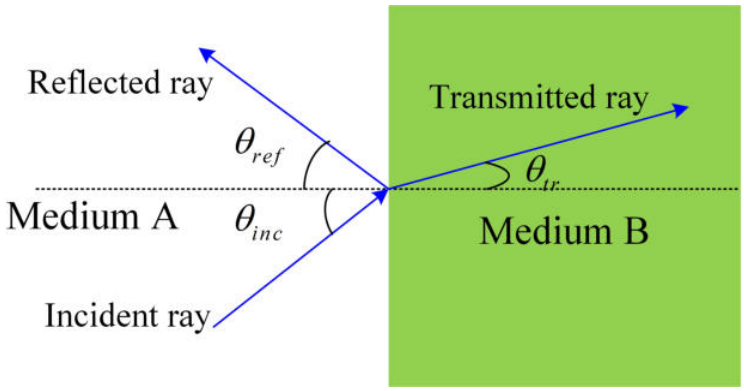

Figure 5.1 Reflection and transmission of a ray at an interface.

At every flat interface, the reflection law holds [Run07], [Som06]

$$\theta_{ref} = \theta_{inc}. \tag{5.1}$$

The amplitudes of the incident and reflected rays are related by

$$A_{ref} = \pm A_{inc} \tag{5.2}$$

with negative sign for Dirichlet condition and positive for Neumann condition. At an interface of two transparent materials, the relation between incident, reflected and transmitted waves are written as [Run07]

$$A_{ref} = RA_{inc} \tag{5.3}$$

$$A_{tr} = TA_{inc} \tag{5.4}$$

where R and T are reflection and transmission coefficients respectively.

A well-known application of Geometrical Optics is the determination of the induced current on a metallic reflector of an antenna. The accurate computation can be done only if the reflector is far enough from the radiation sources for the field to be described in terms of wavefronts and rays. Let the total magnetic field at the reflector be **H**; the surface current density is $J = 2\hat{n} \times \mathbf{H}$ [JRM55], [Cha88]. The scattered or radiated field from this current distribution is computed by the insertion in the PO integral. In this study, the Geometric Optics approximation for the currents is used in a combination with the field equivalence principle to describe the fields transmitted

through electrically large planar meatsheets. In the following section, the PO approximation for the transmitted field is described.

5.3 Transmission of electromagnetic fields through electrically large planar metasheets in PO approximation

In this section, the Physical Optics calculation is used for electrically large circular metasheet. In this calculation, the fields scattered by an object can be calculated by integration of equivalent electric and magnetic currents over a surface enclosing the object [Col60]. The equivalent currents are given by tangential electric and magnetic field components on the integration surface. Since the exact fields are a priory unknown, the GO approximation for the currents is used, assuming that the integration surface is almost flat on the scale of the wavelength (tangent plane approximation). The GO approximation for the equivalent surface currents is [OT17]

$$\mathbf{J}_E(\mathbf{r_1}) \approx \mathbf{J}_E(\mathbf{r_1})^{go} = \hat{n}(\mathbf{r_1}) \times \mathbf{H}^{go}(\mathbf{r_1}) \tag{5.5}$$

$$\mathbf{J}_M(\mathbf{r_1}) \approx \mathbf{J}_M(\mathbf{r_1})^{go} = -\hat{n}(\mathbf{r_1}) \times \mathbf{E}^{go}(\mathbf{r_1}), \tag{5.6}$$

where $\hat{n}$ is the unit normal vector directed into the region where the observer is located (Fig. 5.2). On electrically large surfaces, the edge contribution is a small part of the total induced current on the structure. Except near the edges, Geometrical Optics gives accurate results. In this study, the edge diffraction is described in the PO approximation.

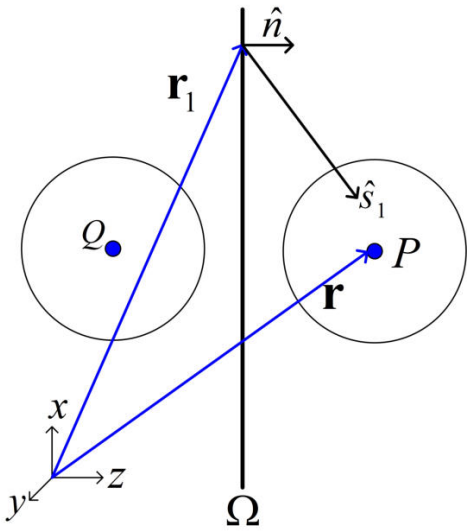

Figure 5.2 Integration surface Ω between the source and observation points.

The electric field transmitted through an infinite planar surface Ω, which separates the source Q and observation point P (Fig. 5.2), can be expressed in terms of equivalence surface currents as [zOE17b]

$$\begin{aligned}\mathbf{E}(\mathbf{r})_{tr} = -\nabla \times \iint_{\Omega} G_1(\mathbf{r},\mathbf{r_1})\mathbf{J}_M(\mathbf{r_1})d\Omega + \\ \frac{1}{j\omega\varepsilon}[k_0^2 + \nabla(\nabla\cdot)]\iint_{\Omega} G_1(\mathbf{r},\mathbf{r_1})\mathbf{J}_E(\mathbf{r_1})d\Omega.\end{aligned} \tag{5.7}$$

Equation (5.7) is applicable at arbitrary distances from the surface. The expression (5.7) can be simplified when the distance between the integration surface and the observation point is larger than a wavelength. By using vector algebra, (5.7) can be simplified as [OT17]

$$[k_0^2 + \nabla(\nabla\cdot)]G_1\mathbf{J}_E \approx [\mathbf{J}_E - (\mathbf{J}_E\cdot\hat{s}_1)\hat{s}_1]k_0^2 G_1 = k_0^2 G_1 \hat{s}_1 \times (\hat{s}_1 \times \mathbf{J}_E) \tag{5.8}$$

$$\nabla \times (G_1\mathbf{J}_M) = \nabla G_1 \times \mathbf{J}_M \approx -jk_0 G_1 \hat{s}_1 \times \mathbf{J}_M. \tag{5.9}$$

Equation (5.7) is written in terms of (5.8) and (5.9) and expressed in a more compact form

$$\mathbf{E}(\mathbf{r})_{tr} = \frac{jk_0}{4\pi}\iint_{\Omega} G_1(\mathbf{r},\mathbf{r_1})\mathbf{c}(\mathbf{r},\mathbf{r_1})d\Omega \tag{5.10}$$

where $\mathbf{c}(\mathbf{r},\mathbf{r_1}) = \hat{s}_1 \times \mathbf{J}_M(\mathbf{r_1}) + Z_0\hat{s}_1 \times \hat{s}_1 \times \mathbf{J}_E(\mathbf{r_1})$, $Z_0 = \sqrt{\frac{\mu_0}{\varepsilon_0}}$ and $\hat{s}_1 = \frac{\mathbf{r}-\mathbf{r_1}}{|\mathbf{r}-\mathbf{r_1}|}$. Let the incident field be a plane wave propagating in the direction $\hat{z}$. The direction of the linear polarization should not change the result, because the polarization-independent metasheets are built from rotationally symmetric particles. If the material of the sheet is fully transparent, the GO approximated currents include only the incident electric field.

In this study, Ω is flat and is positioned ($\hat{n} = \hat{z}$ which is the unit normal vector) at $z = 0$. The surface Ω is chosen to coincide with an interface of a metasheet. The electric field on the metasheet is written in terms of incident electric field and the transmission coefficient as

$$\mathbf{E}_{tr}(x_1, y_1, 0) = T(x_1, y_1)\mathbf{E}_0, \tag{5.11}$$

which permits a simple description of the equivalent currents on the planar metasheet. In this study, the transmission coefficient is obtained from full-wave simulations. The equivalent electric and magnetic currents are written in terms of the transmitted electric field ($\mathbf{E}_{tr}(x_1, y_1, 0)$) and the magnetic field ($\mathbf{H}_{tr}(x_1, y_1, 0)$) on the planar metasheet as [zOE17b]

$$\mathbf{J}_M^{go} \approx -\hat{n} \times \mathbf{E}_{tr}(x_1, y_1, 0) \tag{5.12}$$

$$\mathbf{J}_E^{go} \approx \hat{n} \times \mathbf{H}_{tr}(x_1, y_1, 0). \tag{5.13}$$

For plane waves, the transmitted magnetic field can be written in terms of the transmitted electric field as

$$\mathbf{H}_{tr} = \frac{1}{Z_0} \hat{z} \times \mathbf{E}_{tr}. \tag{5.14}$$

$\mathbf{c}(\mathbf{r}, \mathbf{r_1})$ is written in Cartesian coordinates as

$$\begin{aligned} \mathbf{c}(\mathbf{r}, \mathbf{r_1}) = E_0 T(x_1, y_1) & \frac{z\hat{x} + (x_1 - x)\hat{z}}{\sqrt{(x_1-x)^2 + (y_1-y)^2 + z^2}} \\ & + \frac{((y_1-y)^2 + z^2)\hat{x} - (x_1-x)(y_1-y)\hat{y} + (x_1-x)z\hat{z}}{(x_1-x)^2 + (y_1-y)^2 + z^2}. \end{aligned} \tag{5.15}$$

Direct numerical evaluation can be difficult, particularly when k_0 is large, resulting in rapid oscillations of the integrand over the integration path. The computational cost of direct numerical integration rapidly increases with k_0 [ea16b], [Lud68], [BL05b]. For observation points on the z axis and a circular metasheet, the PO integral (5.10) can be converted to a one-dimensional integral, which can be easily evaluated [zOE17b]. For a circular metasheet of the radius a in free space, the function T can be defined as

$$T(x, y) = \begin{cases} 1 & \text{if } \left|\rho\right| > a \\ T_{sheet} & \text{if } \left|\rho\right| \leq a \end{cases}$$

where ρ is the distance from the z axis. T_{sheet} is the transmission coefficient of the infinite periodic planar array of circular rings. Integrating over the azimuth angle gives the formula [zOE17b]

$$E_{tr}(0,0,z) = E_0 \frac{jk_0}{4\pi} \int_0^{+\infty} e^{-jk_0\sqrt{\rho^2+z^2}} T(\rho_1)(2 + \frac{2z}{\sqrt{\rho^2+z^2}} - \frac{\rho_1^2}{\rho_1^2+z^2}) \frac{\rho_1}{\sqrt{\rho_1^2+z^2}} d\rho_1, \tag{5.16}$$

where $|\mathbf{r} - \mathbf{r_1}| = \sqrt{\rho_1^2 + z^2}$. $T(\rho) = 1$ when $\rho > a$, The transmitted electric field has only one component because the incident field has only one component; therefore, the field becomes a scalar value so the complete transmitted electric field at the observation point is expressed as

$$E_{tr} = E_{tr}^{plate} + E_{tr}^{rim} \tag{5.17}$$

where E_{tr}^{plate} is the field transmitted through the metasheet disc and E_{tr}^{rim} is the field transmitted outside of the metasheet, i.e.,

$$E_{tr}^{plate}(0,0,z) = E_0 \frac{jk_0}{4} \int_0^{a} e^{-jk_0\sqrt{\rho_1^2+z^2}} T_{sheet}(2 + \frac{2z}{\sqrt{\rho_1^2+z^2}} - \frac{\rho_1^2}{\rho_1^2+z^2}) \frac{\rho_1}{\sqrt{\rho^2+z^2}} d\rho_1 \tag{5.18}$$

$$E_{tr}^{rim}(0,0,z) = E_0 \frac{jk_0}{4} \int_a^{+\infty} e^{-jk_0\sqrt{\rho_1^2+z^2}} (2 + \frac{2z}{\sqrt{\rho_1^2+z^2}} - \frac{\rho_1^2}{\rho_1^2+z^2}) \frac{\rho_1}{\sqrt{\rho_1^2+z^2}} d\rho_1 \tag{5.19}$$

Integration by parts is applied, where the derivation is shown in Appendix 2 [Erd56]. The main contribution to the integral comes from the endpoints of the integration interval [zOE17b] and results in

$$E_{tr}^{rim}(0,0,z) = E_0 \frac{1}{4} (2 + \frac{2z}{\sqrt{a^2+z^2}} - \frac{a^2}{a^2+z^2}) e^{-jk_0\sqrt{a^2+z^2}} + O(\frac{1}{k_0}). \tag{5.20}$$

5.4 HFSS simulation setup for finite-size circular metasheet

In this section, the properties of the simulation setup for the finite-size circular metasheet are explained. HFSS is used to calculate the scalar scattered electric field ($E_{sc} = E_{total} - E_{inc}$) metasheet in the Fresnel zone, in the near region, where E_{total} and E_{inc} are the total electric field and the incident electric field, respectively. The metasheet discs are placed in a cylindrical vacuumbox whose material is vacuum (Fig. 5.3). The height of the vacuumbox is 17 mm. The distance between the object and the boundary of the vacuumbox is advised to be at least $\frac{\lambda}{4}$ [Edged], [ANSeda]. A plane linearly polarized wave is the incident wave. The radiation boundary in HFSS (a hybrid region (finite element-boundary integral (FE-BI)) is applied at the whole boundary of the cylindrical vacuumbox. This boundary model is mainly used for electrically large structures, where the mesh truncation increases the speed of the simulation [ANSeda]. This form of the boundary condition is a computationally efficient way of accounting for radiation in electrically large problems. The scattered electric fields along the radiation line which is the positive z axis, are then determined with the combination of the finite element and boundary integral equations methods.

The field is sampled on the z-axis between 0.01 m and 1 m on the right of the discs. The observation line is divided into 1000 points. In HFSS, it is calculated over a normalized distance between 0 and 1.

When the diameter of the disc becomes too large, the simulation takes too long or can not be completed. If the size of unit cells on the metasheet decreases, then their number should increase to cover the surface of electrically large sheet. In this case also, the full-wave simulation can become difficult.

In Fig. 5.4, the metasheet consists of an infinitely thin layer of circular rings on a substrate is shown. The thickness of the substrate is 2 mm. The material of the substrate is FR4. The material of the circular rings is copper, which is defined by a finite conductivity in HFSS. The operation frequency is 10 GHz. A finer mesh is needed for a higher accuracy in the full-wave

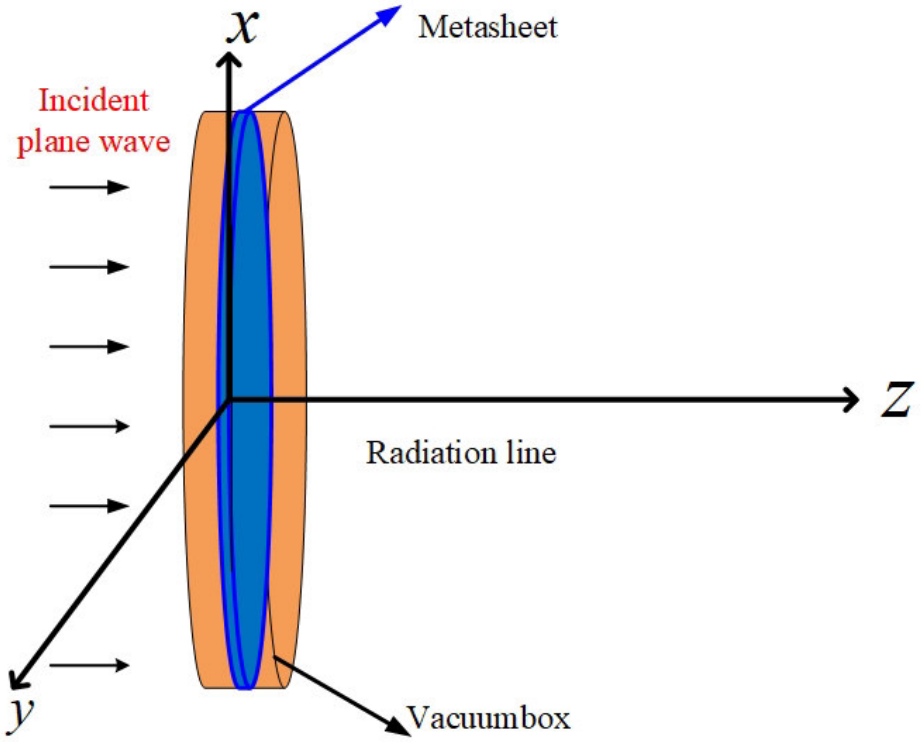

Figure 5.3 Simulation setup for a disk-shaped metasheet.

simulation for decreasing size of the rings. The electrically large metasheet is simulated, and then the results of the PO approach and the full-wave simulation are compared.

5.5 A periodic array of circular rings on a substrate

To derive the transmission coefficient of the metasheet, an infinite periodic planar layer, as explained in Section 3.5 is simulated. In the simulation, auto meshing and slider are used as a mesh model. Direct solver, first-order basis functions and discrete sweep type are chosen. The thickness of the rings is 18 μm. A linearly polarized plane wave is incident normally to the metasheet, and the operation frequency is 10 GHz. The length of the vacuumbox in the HFSS simulation setup is 60 mm. Two differently sized rings have been chosen (Tables 5.1 and 5.2). HFSS version 15.0 has been employed.

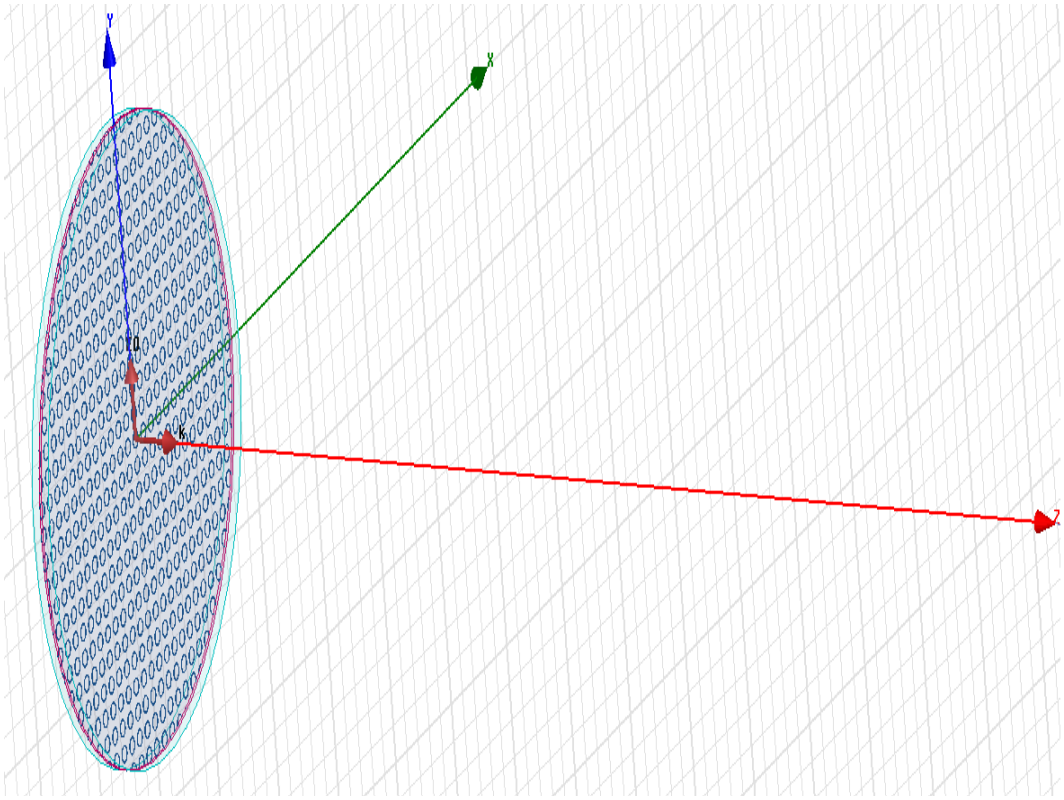

Figure 5.4 The finite circular metasheet in HFSS.

Table 5.1 Dimensional parameters of the circular rings and the unit cell [zOE17b].

r_{out} in mm	r_{in} in mm	Periodicity (p)in mm
1.6	1.44	4.8
4.6	4.14	13.8

Table 5.2 Simulated transmission coefficient for the two differently sized circular rings as described in Table 5.1 [zOE17b].

r_{out} in mm	Phase of T in degree	T in dB
1.6	-42.3	-2.37
4.6	16.3	-1.55

5.6 Full-wave simulation versus PO approximation

In this section, the values of the scattered field on the positive z axis behind the circular metasheet calculated by the full-wave simulation and by the PO method are compared. When the size of the rings becomes smaller, the results of the PO calculation and the full-wave simulation match better as seen from Figs. 5.5 and 5.6. When the size of the rings increases and gets comparable to $\frac{\lambda}{2}$ or greater, the assumption of homogeneity of the metasheet degrades and does not apply anymore. In this situation, PO cannot give accurate results.

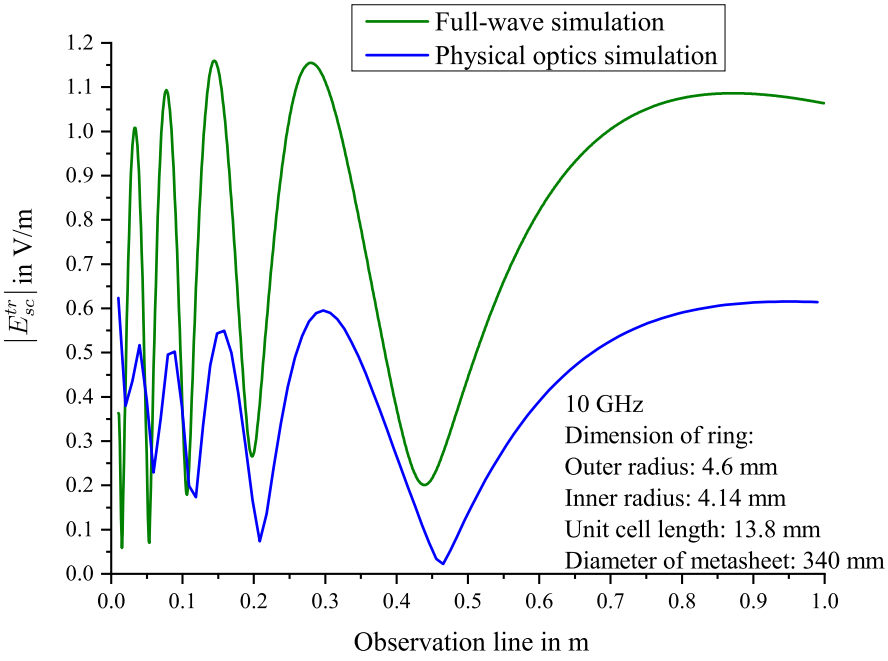

Figure 5.5 Field scattered by a circular metasheet with diameter 340mm along the symmetry axis [zOE17b]. The parameters of the metasheet are given in the diagram.

With the size of the resonators getting smaller, and at the same time, the size of the metasheet increasing, the simulation started to have problems such as long simulation time or the simulation cannot be completed. When the size of the metasheet and resonators are both increased, the scattered field has more oscillations. To increase the accuracy in the PO calculation, the diameter of the metasheet should be as large as possible and the size of the resonators should be much smaller than the operational wavelength.

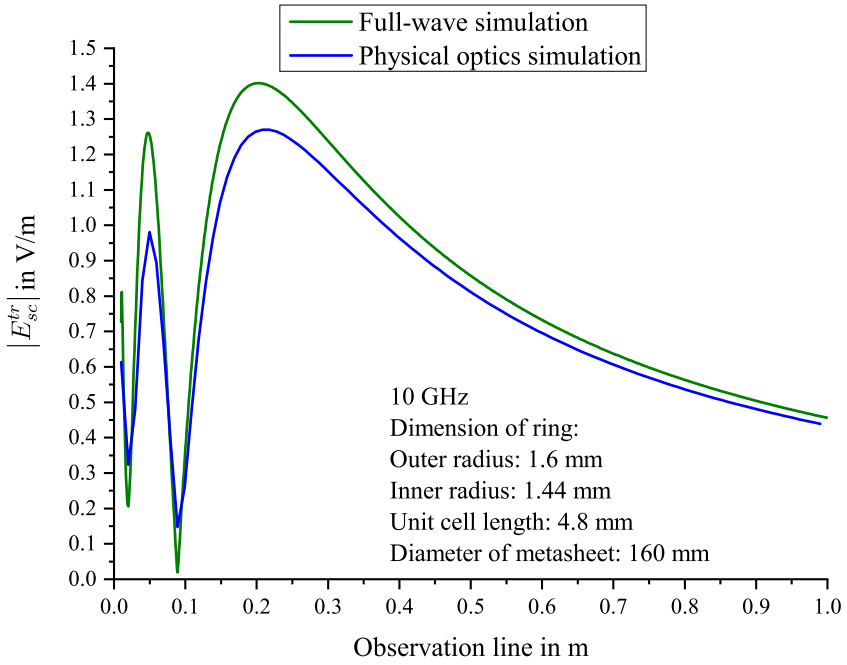

Figure 5.6 The same as in Fig. 5.5 but for the metasheet with diameter 160 mm [zOE17b]. The parameters are given in the diagram.

Chapter 6

Designing a Planar Metalens for a Hemispheric Radome

In this chapter, an application of a specially designed metasheet (metalens) for correction of the phase distortion caused by a dielectric radome is presented. In this study, the metalens is positioned at the basis of the hemispheric radome, and the radome covers the metalens and an antenna (Fig. 6.1). A plane wave is incident perpendicularly to the basis of the radome. Because of the curved surface of the radome, the phase of the wave transmitted through the radome is distorted.

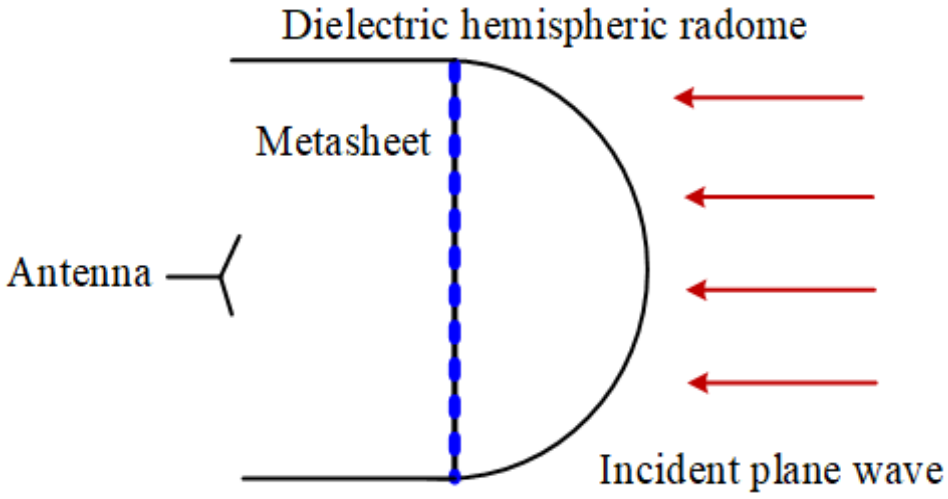

Figure 6.1 Hemispheric radome, a metalens and an antenna.

A metalens can be designed to compensate the phase distortion. Internal reflections in the radome are neglected in the computation. Firstly, the phase of the transmission coefficient is

calculated analytically. The symmetric shape of the radome simplifies the calculation of the phase distribution of the transmitted field. For this calculation, a ray tracing algorithm is used.

After determining the phase distribution over the basis of the radome, a metalens with circular concentric regions will be designed to compensate the phase distortions. Each region of the metalens compensates the phase by a different value.

The metal circular ring as a resonator is chosen to design the metalens, because it is independent of the polarization of the incident wave. Other types of particles (strips, crosses, etc.) have this property partly. In Section 6.1, the dimensional and electrical properties of the radome are addressed. In Section 6.2, the ray tracing algorithm is explained; furthermore, the results of calculation and measurement are compared. In Section 6.3, the setup is described for measuring the phase distribution of a test radome. In Section 6.4, a metasheet with two regions designed as a pre-study for the metalens design is presented. In Section 6.5, a PO solution for the metasheet is explained. In Section 6.6, the setup for measuring the transmission through the metasheet with two regions is described. In Section 6.7, the measured and PO results are compared. In Section 6.8, a design of a metalens for the Ka band is presented. Section 6.9 describes the measurement setup for the radome and the metalens. In Section 6.10, the results of PO calculation and measurements are compared.

6.1 Properties of the hemispheric radome

The hemispheric shape is a special case of the tangent ogive shape. Spherical or hemispheric radomes are suitable for terrestrial radar. The shape is not useful for airbone applications because of a vast aerodynamic drag [Koz10].

A manufactured test radome is shown in Fig. 6.2. The thickness of the radome is 5 mm and its material is polypropylene. Transmission measurements were carried out in the frequency range from 26.5 GHz to 40 GHz (Ka band). The measured values of the relative permittivity are almost frequency independent, so an arithmetic average of the relative permittivity in this frequency range , which is equal to 2.242, is used in the calculations. The radius of the hemisphere is 100 mm, which includes the thickness of the radome. The phase distribution at 28 GHz along the diameter of the radome (190 mm, excluding the thickness of the radome) is calculated.

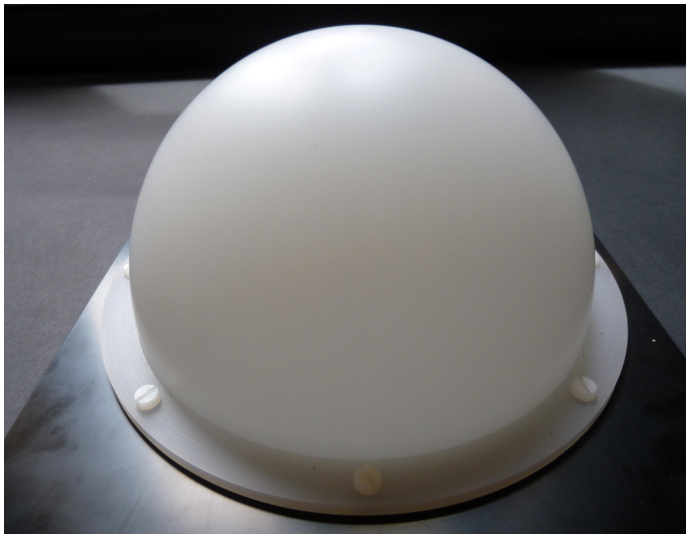

Figure 6.2 Manufactured hemispheric radome.

6.2 Ray tracing simulation of the radome

A ray tracing algorithm is a way of implementing Geometrical Optics solutions. It can create accurate result and be combined with the refraction laws for rays. The computation time can last longer when the structure is electrically large and many rays have to be launched. The parametric representation of the ray is utilized to solve a system of equations yielding the point of intersection.

In the framework of ray tracing, the wavefront is discretized in small flat pieces and every piece is traced independently to the receiver. In Figs. 6.3 and 6.4, the interaction of a ray and the radome is presented. According to Fig. 6.3, a first phase shift comes out when the ray from the radiation source reaches the curved surface because of the change of the distance between the incident wave front and the curved surface of the radome. A second phase shift occurs, while the ray goes through the wall of the radome and then, a third phase shift happens when the ray leaves the radome inner surface and reaches the basis of the radome.

Let θ_1, θ_2, θ_3 be the incident angle as at the outer surface, the incident angle at the inner surface and the refractive angle at the inner surface of the radome, respectively. Because of the curvature, the incidence angle θ_1 is different for every ray (Fig. 6.3).

A ray tracing algorithm according to [Gla89] is followed and applied to calculate the transmission coefficient along the radius of the radome. For solving the intersection problem, the ray equation is inserted into the sphere equation.

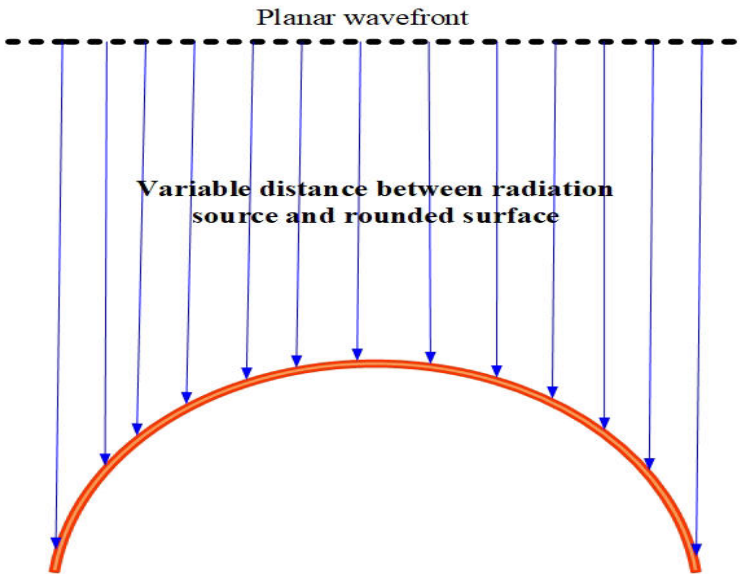

Figure 6.3 Phase shift due to a curved surface.

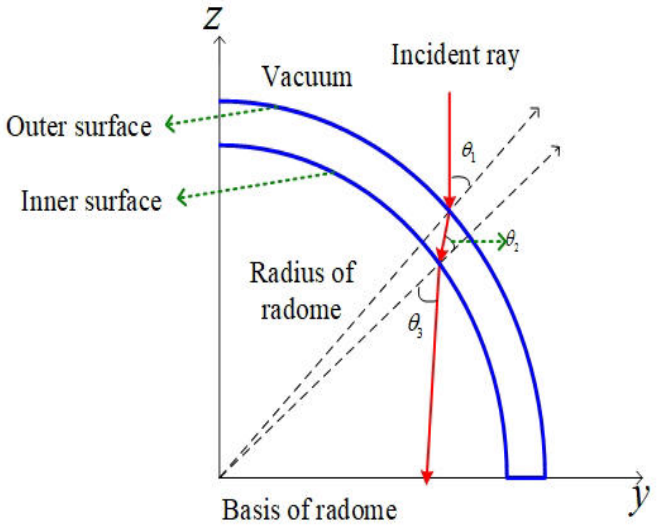

Figure 6.4 Refraction of a ray through a radome wall.

The center of the hemispheric radome is positioned at the origin. The points of intersection of the ray with the outer and inner surfaces (see Fig. 6.4) can be found by using Snell's law. The ray is defined as a parametric structure in the form of a set of points on the line $\mathbf{R}(p) = \mathbf{R}_0 + \mathbf{R}_d p$, where $p > 0$ which is a point on the ray. The ray is defined as

$$\begin{aligned}\mathbf{R}_0 &\equiv [X_0, Y_0, Z_0],\\ \mathbf{R}_d &\equiv [X_d, Y_d, Z_d],\end{aligned} \tag{6.1}$$

where $\mathbf{R}_0$ is the initial position vector of the ray and $\mathbf{R}_d$ is the direction vector. The sphere surface equation is expressed as [Gla89]

$$(X_s - C'_x)^2 + (Y_s - C'_y)^2 + (Z_s - C'_z)^2 = R_a^2, \tag{6.2}$$

where R_a is the radius of the radome, C'_x, C'_y and C'_z are the coordinates of the sphere center and X_s, Y_s, Z_s are the coordinates of points on the spherical surface. The center of the hemisphere is defined by $C'_x = 0, C'_y = 0, C'_z = 0$. The parametric equation for the ray is inserted into (6.2), which results in the equation

$$Ap^2 + Bp + C = 0 \tag{6.3}$$

in terms of p [Gla89] where

$$\begin{aligned}A &= X_d^2 + Y_d^2 + Z_d^2 = 1,\\ B &= 2X_d(X_0 - C'_x) + 2Y_d(Y_0 - C'_y) + 2Z_d(Z_0 - C'_z),\\ C &= (X_0 - C'_x)^2 + (Y_0 - C'_y)^2 + (Z_0 - C'_z)^2 - R_a^2,\end{aligned} \tag{6.4}$$

and $A = 1$ means that the ray direction is a unit vector. The solutions for p of the quadratic equation (6.3) are given by

$$\begin{aligned}p_1 &= \frac{-B - \sqrt{B^2 - 4AC}}{2},\\ p_2 &= \frac{-B + \sqrt{B^2 - 4AC}}{2}.\end{aligned} \tag{6.5}$$

The discriminant in (6.5) should be positive, so that the intersection point is real valued. The smallest, positive root is the closest intersection distance on the ray. When p is found, the coordinates of the intersection point are expressed from the parametric ray equation as [Gla89]

$$\mathbf{r}_{int} = [x_i, y_i, z_i] = [X_0 + X_d p, Y_0 + Y_d p, Z_0 + Z_d p]. \tag{6.6}$$

The unit normal vector at the surface is described as

$$\mathbf{r}_{nor} = \left[\frac{x_i - C'_x}{R_a}, \frac{y_i - C'_y}{R_a}, \frac{z_i - C'_z}{R_a}\right] \tag{6.7}$$

The Snell's law is utilized to calculate the direction vectors of the refracted rays. The Fresnel equations are used to express the local transmission coefficient at each surface at the radome. The refraction of rays should be included in the ray tracing calculation. Let η_1 be the refractive index of vacuum and η_2 the refractive index of the medium of the radome.

The vector **I** is the direction of the incident (incoming) ray which comes from medium 1. **T** is the propagation direction of the transmitted ray which goes through medium 2. The vector **N** is the surface normal. According to Snell's law, the angles of the incident and transmitted rays are related as

$$\frac{\sin\theta_i}{\sin\theta_t} = \frac{\eta_t}{\eta_i} = \eta_{ti}, \tag{6.8}$$

and

$$\eta_{it} = \frac{1}{\eta_{ti}}. \tag{6.9}$$

In vector format, the direction of the transmitted ray is written in terms of the surface normal vector and the incident ray as

$$\mathbf{T} = \Lambda\mathbf{I} + \zeta\mathbf{N}, \tag{6.10}$$

where Λ and ζ are coefficients. The angles of incidence and refraction (θ_i and θ_t) can be expressed as [Gla89]

$$\cos\theta_i = \mathbf{N}\cdot(-\mathbf{I}), \tag{6.11}$$

$$\cos\theta_t = (-\mathbf{N})\cdot(\mathbf{T}). \tag{6.12}$$

The square of (6.8) is written according to the pythagorean identity of sin and cos functions as [Gla89]

$$(1-\cos\theta_i^2)\eta_{it}^2 = 1-\cos\theta_t^2. \tag{6.13}$$

Using (6.12), (6.13) can be written as

$$1-(1-\cos\theta_i^2)\eta_{it}^2 = (\Lambda\cos\theta_i-\zeta)^2. \tag{6.14}$$

Furthermore, since **T** is a unit vector

$$1 = \mathbf{T}\cdot\mathbf{T}, \tag{6.15}$$

inserting (6.10) in (6.15) gives

$$1 = \Lambda^2 - 2\Lambda\zeta\cos\theta_i + \zeta^2. \tag{6.16}$$

The two equations (6.14) and (6.16) are solved together to find the values of Λ and ζ. The four values of Λ and ζ come out but to get the transmitted ray vector, the value of Λ and ζ should be

$$\Lambda = \eta_{it} \tag{6.17}$$

$$\zeta = \eta_{it}\cos\theta_i - \sqrt{(1+\eta_{it}^2(\cos\theta_i^2 - 1))}. \tag{6.18}$$

Equation (6.18) is inserted into (6.10) to give the transmitted ray vector. In a similar way, the refraction at the inner surface of the radome is treated. At the basis of the radome, the distortion due to transmission through the radome can be described by the factor [zOE20]

$$T_{radome} = \frac{E_{inc}(A)e^{jk_0|AB|}T_{12}e^{jk|BC|}T_{21}e^{jk_0|CD|}}{E_{inc}(A)e^{jk_0|AE|}}, \tag{6.19}$$

where T_{12} is the transmission coefficient from medium 1 to medium 2, T_{21} is the transmission coefficient from medium 2 to medium 1, k_0 is the propagation constant in free space and k is the propagation constant in the dielectric medium of the radome. While the amplitude of T_{radome} depends on the polarization, the phase does not depend on the polarization, provided that the losses in the material of the radome are negligible. The attenuation through the radome is not considered.

The multiple reflections in the radome wall and in the interior of the radome are not included in this study. An obliquely incident plane wave transmitted through the radome wall in the interior of the radome can be multiply reflected between the sidewalls of the radome. In this study, the plane wave is incident parallel to the symmetry axis of the radome (Fig. 6.3) and no such reflections occur. Furthermore, multiple reflections take place in the wall of the radome, but for a sufficiently transparent radome these contributions can be neglected. For example, assume that $\varepsilon_r = 2.242$ (polypropylen) and the incidence angle on the outer surface is 24° and refractive angle from vacuum to medium of radome is 16°. Then, the amplitude of the main transmitted ray is $|\tau_1\tau_2| = 0.9594$ and the amplitude of the doubly reflected ray is $\left|\tau_1\tau_2 q_1 q_2\right| = 0.0437$. Here, τ_1, q_1 are transmission and reflection coefficient from vacuum to medium of radome and τ_2, q_2 are transmission and reflection coefficient from medium of radome to vacuum. The ratio of transmission of second ray to main ray is ≈ 0.04555.

In (6.19) and as it is shown in Fig. 6.5, $|AB|$ is the distance from the source to the outer surface of the radome. $|CD|$ is the distance intersection point at the inner surface of the radome to the point, at which the ray intersects the basis of the radome. If the radome is removed, then the ray propagates straightforward without refraction, and $|AE|$ is the distance between the source and the basis plane. $|BC|$ is the distance between the inner and the outer surface of the radome.

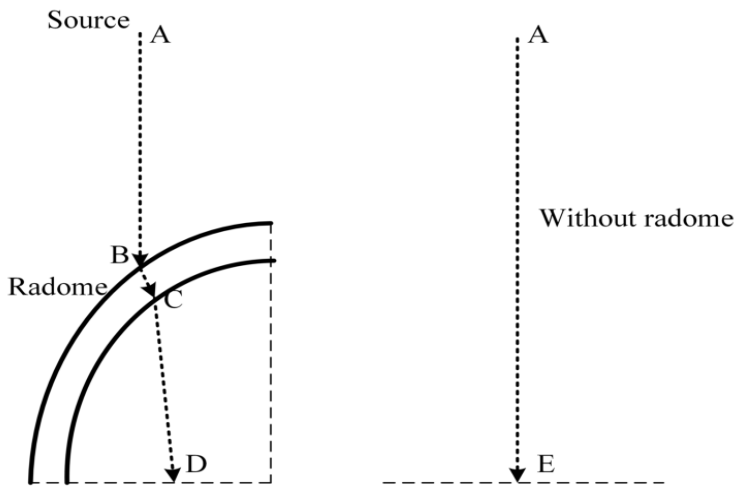

Figure 6.5 The optical path between a source of the incident wave and the ground plane with and without radome.

The diffraction of the incident wave at the edges of the radome is included only in the PO approximation (no edge corrections) in order to reduce the complexity of the computation. The analysis will be limited to the case of axial illumination of the radome, which is sufficient for applications in which the main lobe of antenna is oriented in the axial direction.

6.3 Measurement setup for the test radome

The measurement setup is composed of a corrugated horn as a transmit antenna, an antenna lens and a small open waveguide as a receiving antenna or probe (Fig. 6.6). The test radome is placed in the holder as shown in Fig. 6.7. The distance between the transmit antenna and radome is 400 cm. The distance between the probe and the holder is 10 cm. The copolar polarization is considered. In this measurement, no metasheet is included. The aim of this measurement is the comparison with the ray tracing calculation. The distance between the lens and the horn antenna is 160 cm.

A lens in front of the transmit antenna is used to illuminate the radome with a plane wave. The normalized phase of the measurement at the observation point is expressed as

$$P(E_{dr}) = P(E_R) - P(E_h), \tag{6.20}$$

where $P(E_R)$ is the phase of the electric field transmitted through the radome. $P(E_h)$ is the phase of the electric field transmitted through the holder without radome and metasheet.

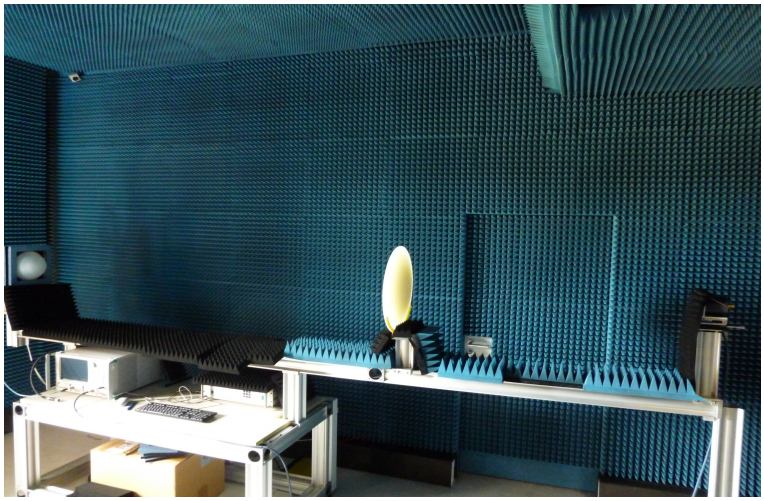

Figure 6.6 Measurement setup with the hemispheric radome (left), an antenna lens (in the middle) and a horn antenna (right).

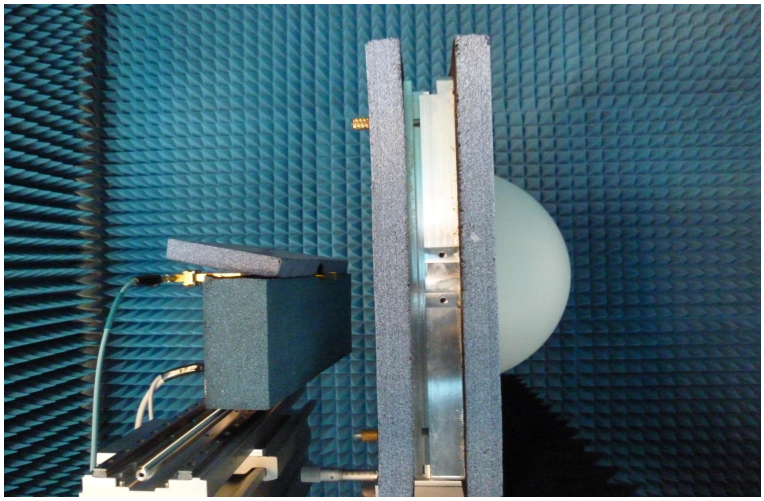

Figure 6.7 A probe and a holder with the radome.

The comparison of the calculated phase and the normalized phase of the measurement of the transmitted signal at the radome basis along the radome diameter at 28 GHz is shown in Fig. 6.8. As it is seen that there is an acceptable match. As it is observed in Fig. 6.8, there is an asymmetry in the measured result even if the radome has a symmetric shape. The asymmetry is caused by a limited precision in positioning the radome and the antennas. Even a positioning error of an order of 0.1 mm results in significant phase distortion.

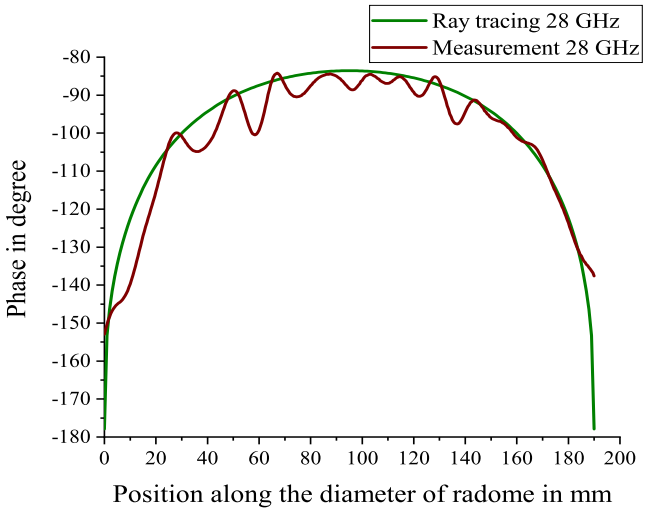

Figure 6.8 Phase distribution along the diameter of the radome at 28 GHz.

6.4 Design of a metasheet with two regions as a pre-study

The aim of the metasheet described in this section is to validate the results of the PO calculations for an inhomogeneous metasheet. This design was also used to analyze the dielectric properties of the available substrate materials in the Ka band.

The full-wave simulations and the semianalytical approach for an infinite periodic planar array are explained in Chapters 3 and 4. The metasheet design under study consists of two regions, such that, at each region the size of the resonators is different (Fig. 6.9). Because of this, the metasheet consists of two zones with different transmission properties. Another goal was to make the measurement setup ready for the metalens in Section 6.8. It is seen from Fig. 6.9, the layer is divided into 2 regions. The dimension of whole plate is 250×250 mm^2. The dimension of the region 1 is 62×62 mm^2. The area of regions 1 and 2 together is 212×212 mm^2. The manufactured metasheet according to these sizes is shown in Fig. 6.11.

A plane wave incident normally to the surface of the metasheet is considered. The size of the unit cell is 4 mm. The material of the dielectric substrate is FR4. The thickness of the dielectric substrate is 2 mm. In the full-wave simulations, a predefined value $\varepsilon_r = 4.4$ from the HFSS list of material parameters was used. The size of the copper rings in the first and second regions are different. The dimensions of the rings in region 1 (inner) and region 2 (outer) are $r_{in} = 1.09$ mm, $r_{out} = 1.19$ mm and $r_{in} = 1.15$ mm, $r_{out} = 1.25$ mm, respectively. The thicknesses of the rings is 0.018 mm. The phase and the amplitude of the transmission coefficient should differ from region 1 to region 2, because of the different dimensions of the rings. So, free-space

transmission measurements were carried out to extract the transmission coefficient for the region1 and compare with the results of the full-wave simulations. The comparison has revealed a mismatch between the results (Fig. 6.10).

In order to match the simulation with the measurement, the full-wave simulation was repeated with slightly different relative permittivities. The best match is achieved with $\varepsilon_r = 4.75$. The values of the transmission coefficient of region 2 in Table 6.1 are calculated by full-wave simulation with new relative permittivity. The values of the transmission coefficient are obtained by multiplication of S_{21} with $e^{jk_0 l}$, where l is the distance between the two Floquet ports in the simulation setup. l is 50 mm. The transmission coefficient for region 1 in Table 6.1 is the measured value. The HFSS simulation setup described in Section 3.5 is applied and the classic mesh, iterative solver and first-order basis functions are used. The model resolution is activated on the dielectric substrate to improve the mesh quality, increase the mesh speed and improve the model convergence [Coreda]. The mesh length is chosen as 0.2 mm.

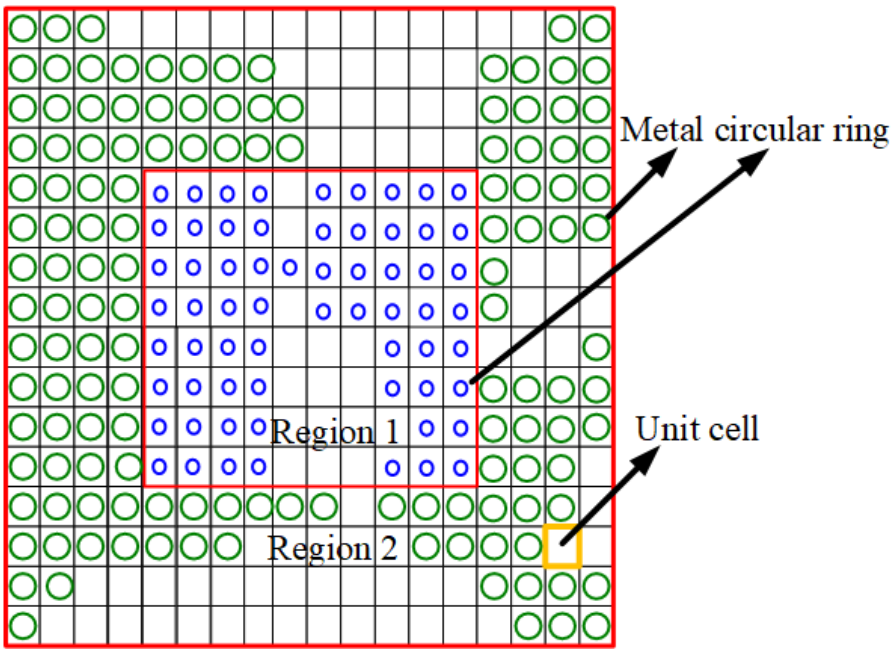

Figure 6.9 Metasheet with two regions filled with variously sized metal rings on an FR4 substrate.

Table 6.1 Transmission coefficients of the regions in the metasheet for three different frequencies.

T of the region 1	T of the region 2	Frequency in GHz
$-0.12619-j0.0679$	$0.0069+j0.0960$	28
$0.0512-j0.0607$	$0.1786+j0.1140$	29
$0.1871-j0.1082$	$0.2678-j0.1586$	30

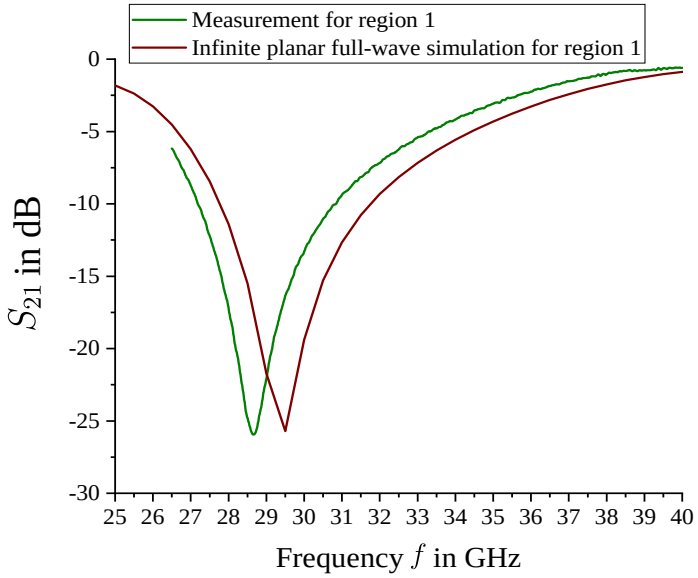

Figure 6.10 Measured transmission coefficient of the inner region of the metasheet in the Ka band.

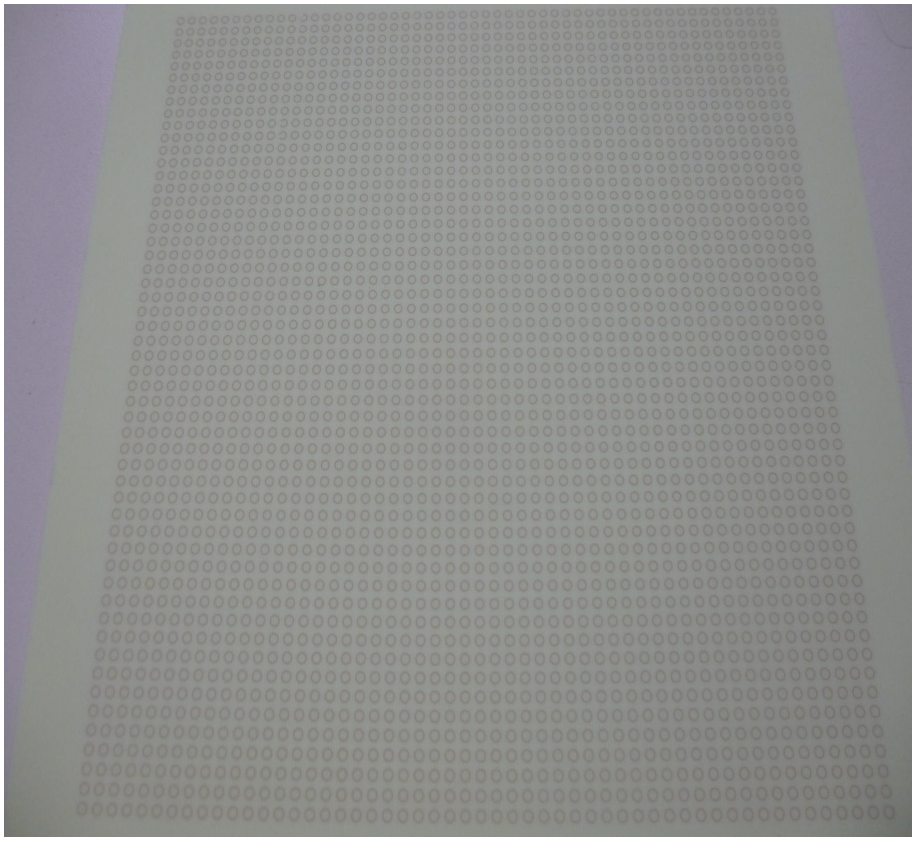

Figure 6.11 Manufactured two-region metasheet.

6.5 PO calculation for the metasheet

The PO method is used to determine the electric field transmitted through the metasheet shown in Figs. 6.9 and 6.11. Equation (5.10) is used in the PO calculation. In Chapter 5, the PO integral was calculated along the z axis. In this section, the observation line is perpendicular to the z axis. The incident electric field is a linearly polarized plane wave propagating in the $-z$ direction with the phase equal to zero at $z=0$, where the metasheet is positioned. The main difficulty in the calculation of the PO integral is that the wavenumber k_0 is large in the exponential part of the Green's function in (5.10) causing rapid oscillations of the integrand function. Therefore, some modifications need to be applied to increase the accuracy.

The modification consists in subdivision of the integration region in smaller pieces, followed by linear approximation of the phase in the exponential factor. For showing this modification better, a similar integrand can be examined [Cra91] according to

$$\int_a^b A(q)e^{-jk_0M(q)}dq. \tag{6.21}$$

When the amplitude factor $A(q)$ is slowly varying on the integration interval, then it can be assumed constant and factored out of the integral. The remaining integral is only applied to the exponential function. If the integration interval is sufficiently small, then the phase term $M(q)$ can be approximated by the first-order polynomial as

$$M(x)=m_1+m_2q, \tag{6.22}$$

which permits analytical evaluation of the integral. In this study, the integration region is two dimensional and a two-dimensional linear approximation of the phase factor is necessary. For this linear approximation, a Taylor series is utilized. The amplitude term $A(q)$ can be assumed constant because it is a slowly varying function compared with the exponent. A similar approach is described in [IH91], [CI94]. The PO integral is calculated by summation. The integration surface can be divided into small triangular or square facets. The equivalent surface currents are assumed to be constant at each element. In this study, the shape of the facets is square. Equation (5.10) can be written as

$$\mathbf{E}(\mathbf{r})_{tr}=\frac{jk_0}{4\pi}\sum_{n=1}\frac{\mathbf{c}(\mathbf{r},\mathbf{r_{cn}})}{|\mathbf{r}-\mathbf{r_{cn}}|}\iint_{\Omega_n}e^{-jk_0|\mathbf{r}-\mathbf{r_1}|}d\Omega \tag{6.23}$$

where $\mathbf{c}(\mathbf{r},\mathbf{r_1})$ is given by (see chapter 5)

$$\mathbf{c}(\mathbf{r},\mathbf{r_1}) = \hat{s}_1 \times \hat{z} \times \mathbf{E}(\mathbf{r_1}) - \hat{s}_1 \times \hat{s}_1 \times \mathbf{E}(\mathbf{r_1}). \tag{6.24}$$

The surface integral (6.23) is calculated over the area of each facet Ω_n. For sufficiently small facets, the Taylor series can be applied to the phase part of the exponential function in (6.23). It can be shown that [zOE20]

$$\iint_{\Omega_n} e^{-jk_0|\mathbf{r}-\mathbf{r_1}|} d\Omega \cong a_n b_n \,\mathrm{sinc}(\frac{k_0}{2}(\mathbf{r_{2n}}-\mathbf{r_{1n}},\hat{s}_{cn}))\mathrm{sinc}(\frac{k_0}{2}(\mathbf{r_{3n}}-\mathbf{r_{2n}},\hat{s}_{cn}))e^{-jk_0|\mathbf{r}-\mathbf{r_{cn}}|}, \tag{6.25}$$

where $\hat{s}_{cn} = \frac{\mathbf{r}-\mathbf{r_{cn}}}{|\mathbf{r}-\mathbf{r_{cn}}|}$ is the propagation unit vector, $\mathbf{r_{cn}} = \frac{1}{4}(\mathbf{r_{1n}}+\mathbf{r_{2n}}+\mathbf{r_{3n}}+\mathbf{r_{4n}})$ is the center of the facet and $\mathbf{r_{1n}}$, $\mathbf{r_{2n}}$, $\mathbf{r_{3n}}$ and $\mathbf{r_{4n}}$ are the corner points of the facet as shown in Fig. 6.12. The derivation of the surface integral (6.25) is explained in the appendix.

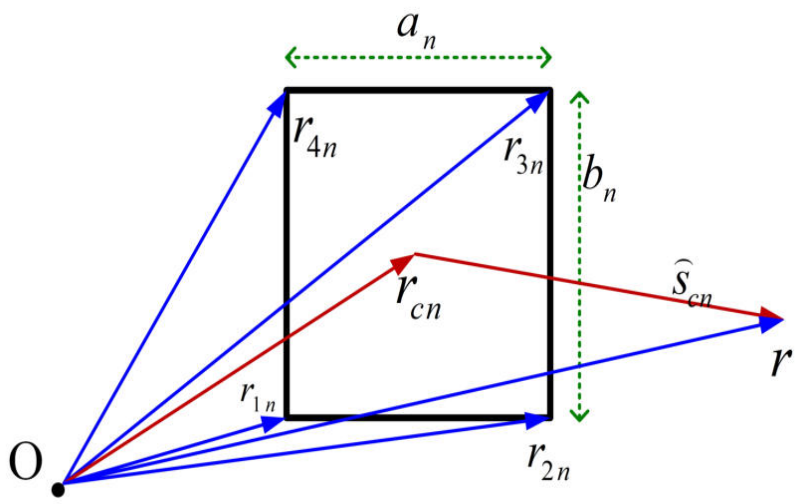

Figure 6.12 A square facet and the points $\mathbf{r_{cn}}$ and $\mathbf{r}$ from (6.25) [zOE20] [reproduced figure courtesy of The Electromagnetics Academy].

The integration region (212 mm × 212 mm) is divided into equal square facets as shown in Fig. 6.13. The calculation is done in Matlab. The metasheet is assumed to be surrounded by an impenetrable absorber, so there is no term similar to E_{tr}^{rim}.

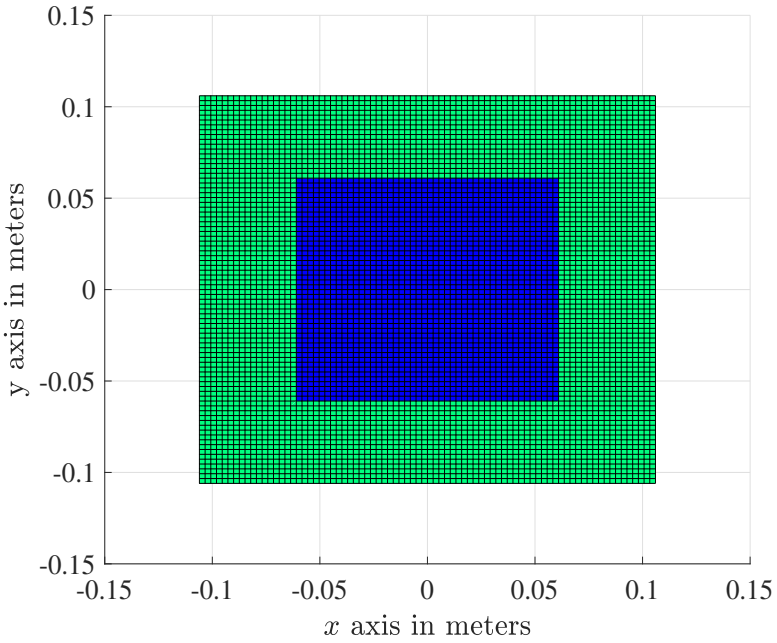

Figure 6.13 Division of the two-region metasheet into facets for the PO calculation.

6.6 Measurement setup for the two-region metasheet

The setup for measuring transmission through the two-region metasheet is shown in Fig. 6.14. A horn antenna is used as a transmit antenna. A lens transforms the radiated wave into a plane wave. The distance between the lens and the transmit antenna is 162 cm. The distance between the lens and the metasheet is 236 cm. An open waveguide (receiving antenna or probe) is positioned at the backside of the metasheet (Fig.6.15). In this study, measurements, for two different distances 4 cm and 6 cm between the metasheet and the probe are used. The distance between the metasheet and the receiving antenna is important because it is aimed to observe the response of each region clearly and separately. The transmitted field was measured along a horizontal line. The measurements were carried out for two different configurations: for the holder alone(calibration) and for the holder with the metasheet. For comparing measured and calculated results, the transmission data were normalized to the calibration data as

$$20\log(|E_d|) = 20\log(|E_{MS}|) - 20\log(|E_h|), \tag{6.26}$$

where E_{MS} is the electric field transmitted through the metasheet fixed in the holder, and E_h is the electric field transmitted only through the holder.

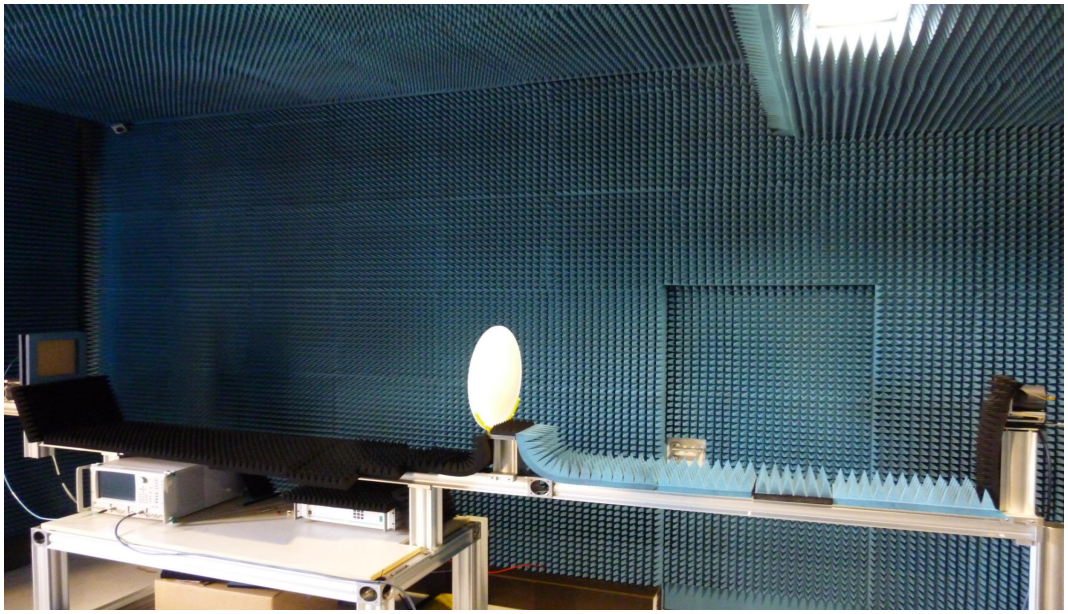

Figure 6.14 Measurement setup for the two-region metasheet.

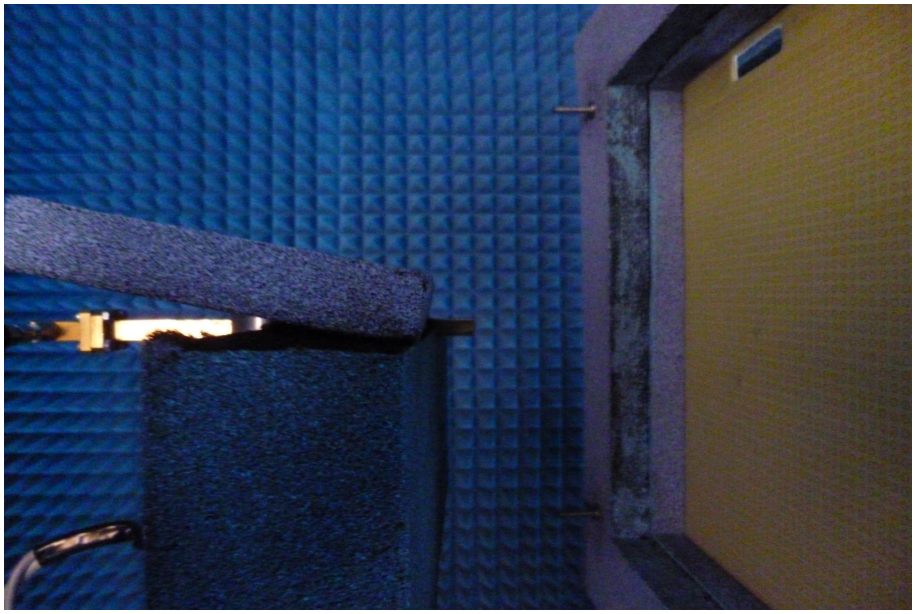

Figure 6.15 An open waveguide (probe) and the backside of the metasheet.

The normalized phase at the observation point is expressed as

$$P(E_d) = P(E_{MS}) - P(E_h). \tag{6.27}$$

When $P(E_d) < -180^o$, then 360^o is added to the phase difference. If $P(E_d) > 180^o$, then 360^o is subtracted from the difference.

6.7 Comparison of the calculated and measured results

The results of measurements and calculations are compared. VV and HH polarization cases are considered. For the frequencies 28 GHz and 29 GHz and the distances 4 cm and 6 cm between metasheet and receiver antenna, the results match well as seen from Fig. 6.17 to 6.26 but for the frequency 30 GHz at 6 cm, the calculated and measured phase results do not overlap completely as seen in Fig. 6.16. The reason can be that the effect of the edges of the layer cannot be ignored in higher frequencies in the measurement for the outer region. The results clearly show the jumps in the amplitude and phase of the transmitted field at the boundaries between the regions on the metasheet. The results of measurement and calculation are compared at the frequencies 28 GHz, 29 GHz and 30 GHz.

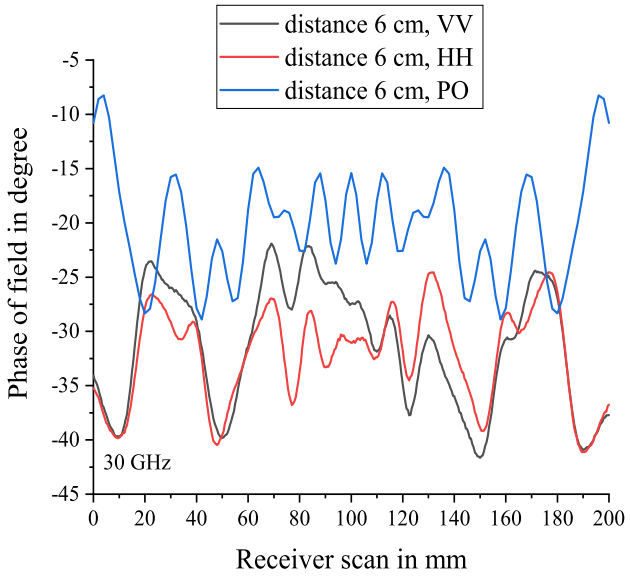

Figure 6.16 PO and measurement results for the phase of the transmitted field at the distance 6 GHz and freqeuncy 30 GHz (HH and VV polarization cases).

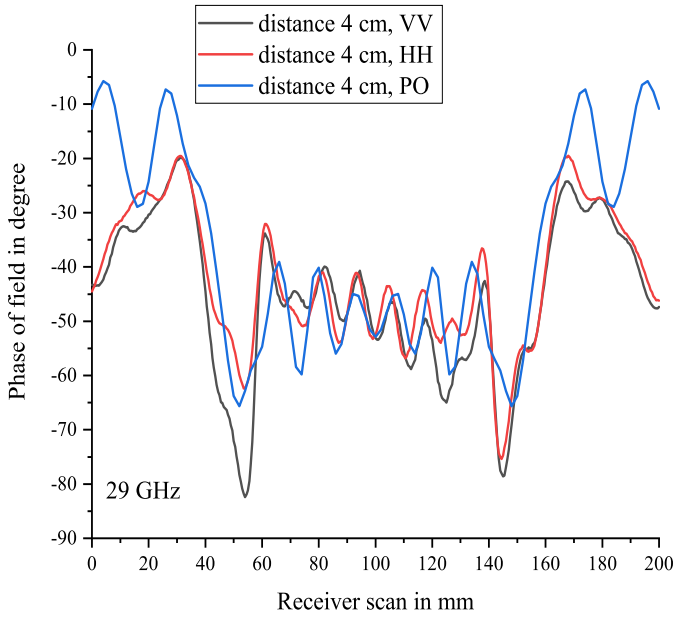

Figure 6.17 The same as in Fig. 6.16 for 29 GHz and 4 cm.

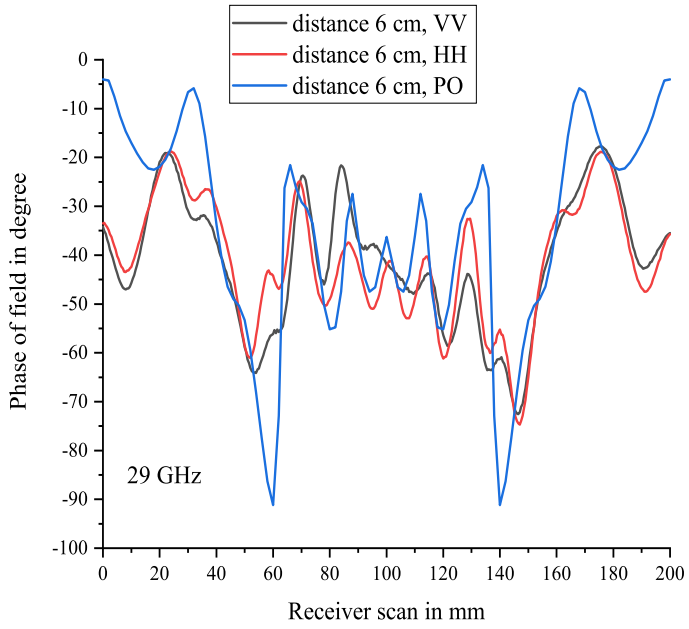

Figure 6.18 The same as in Fig. 6.17 but for the distance 6 cm.

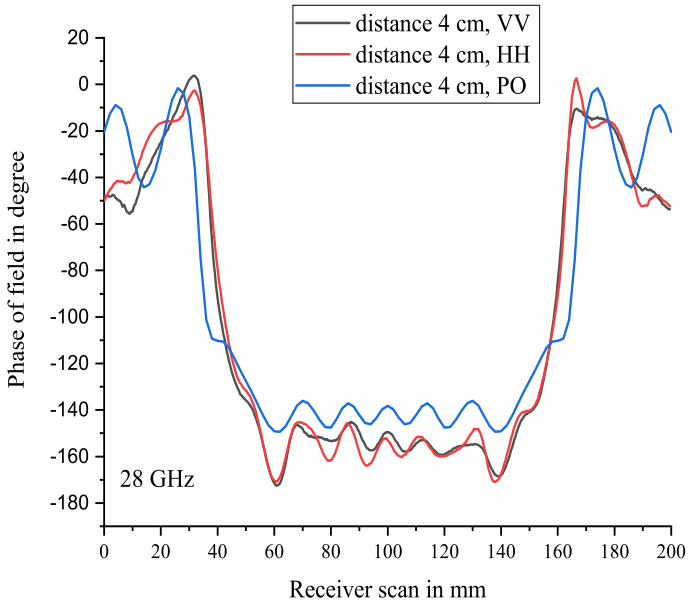

Figure 6.19 The same as in Fig. 6.17 but at 28 GHz for 4 cm.

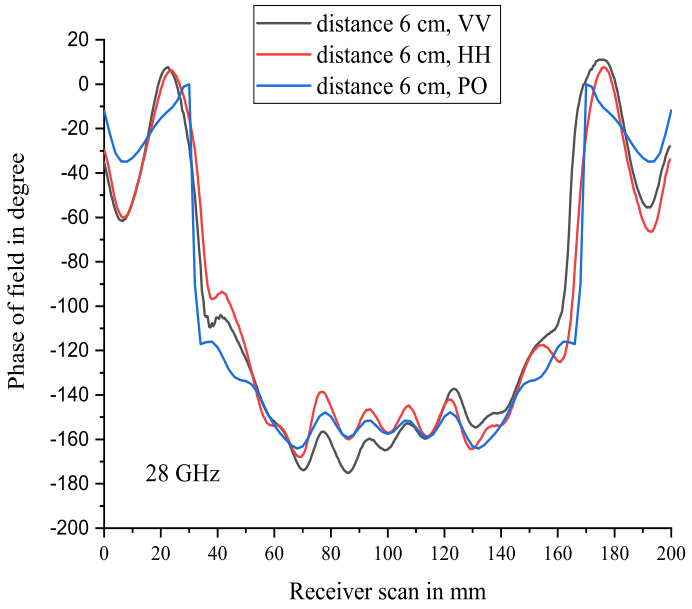

Figure 6.20 The same as in Fig. 6.19 but for the distance 6 cm.

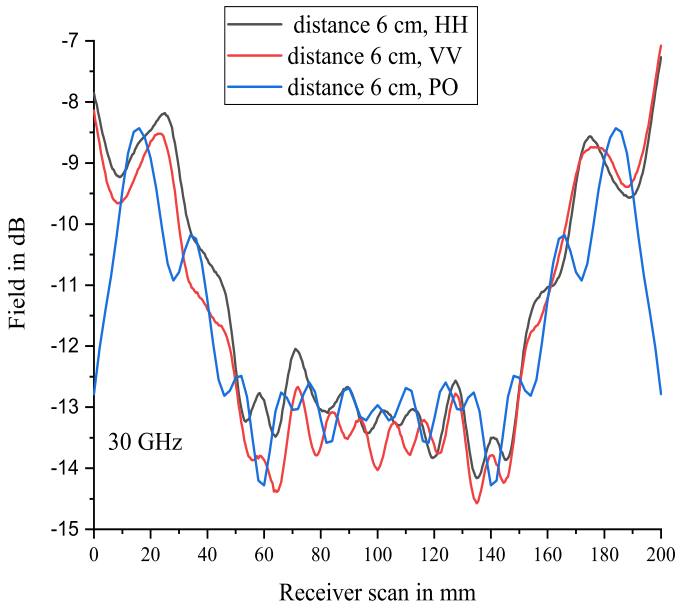

Figure 6.21 The same as in Fig. 6.16 but for amplitude.

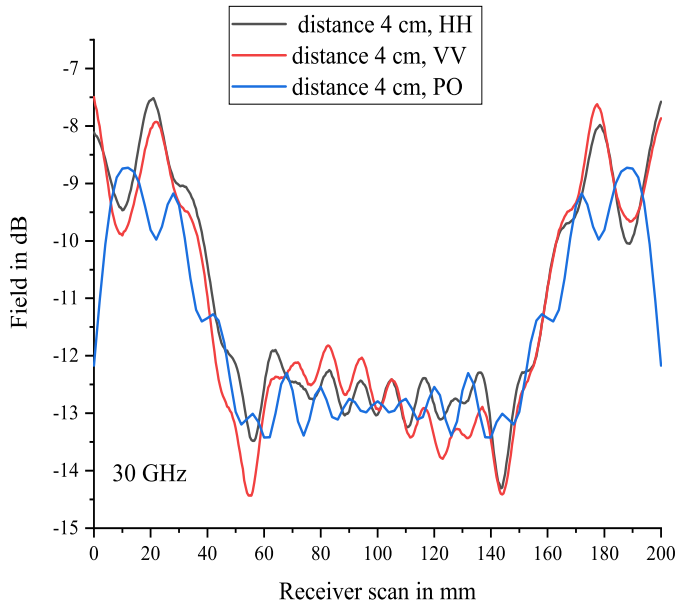

Figure 6.22 The same as in Fig. 6.21 but for the distance 4 cm.

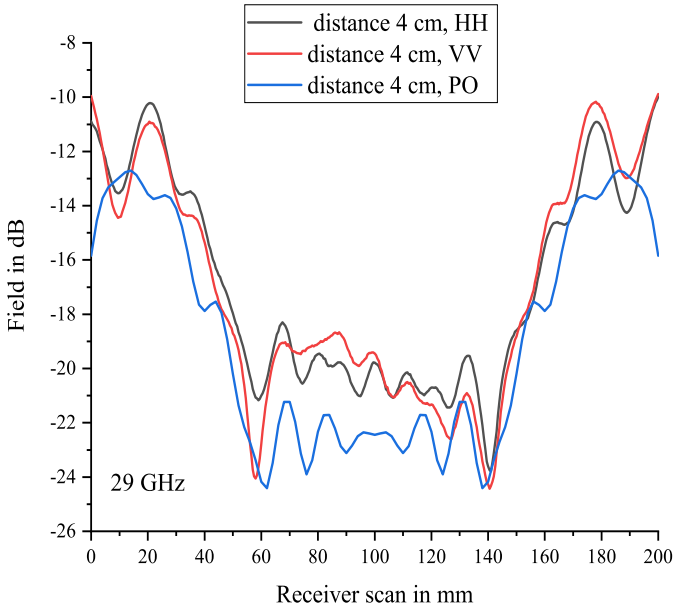

Figure 6.23 The same as in Fig. 6.22 but at 29 GHz.

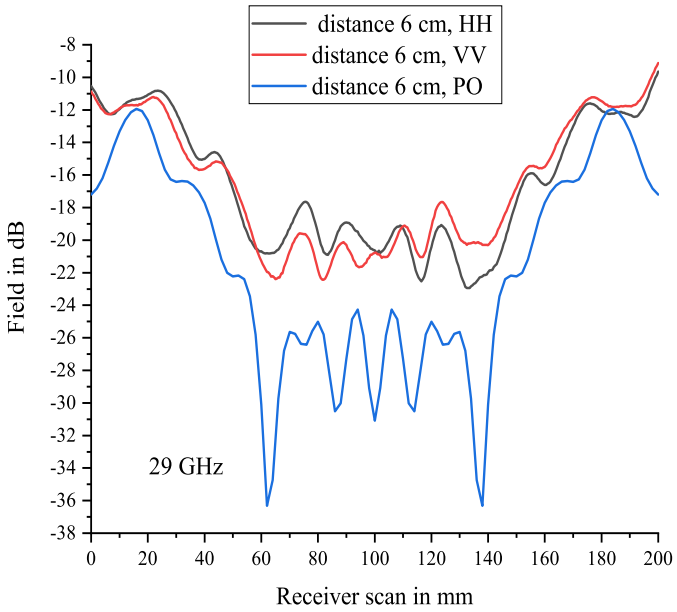

Figure 6.24 The same as in Fig. 6.23 but for 6 cm.

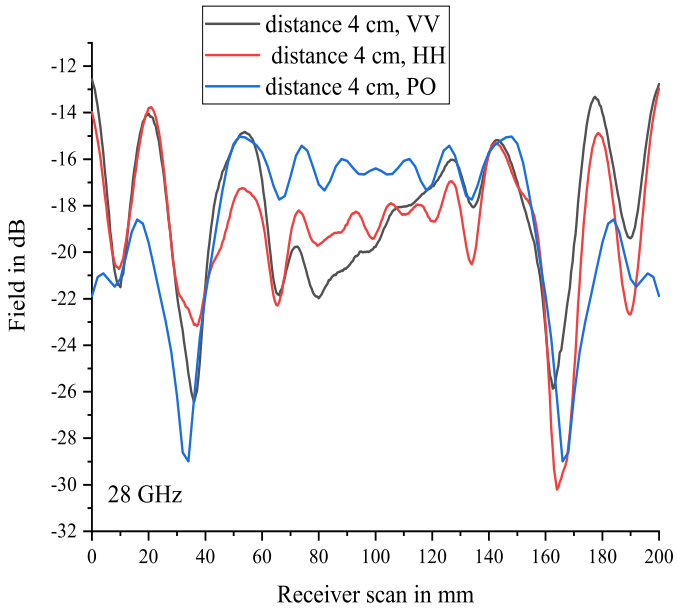

Figure 6.25 The same as in Fig. 6.23 but at 28 GHz.

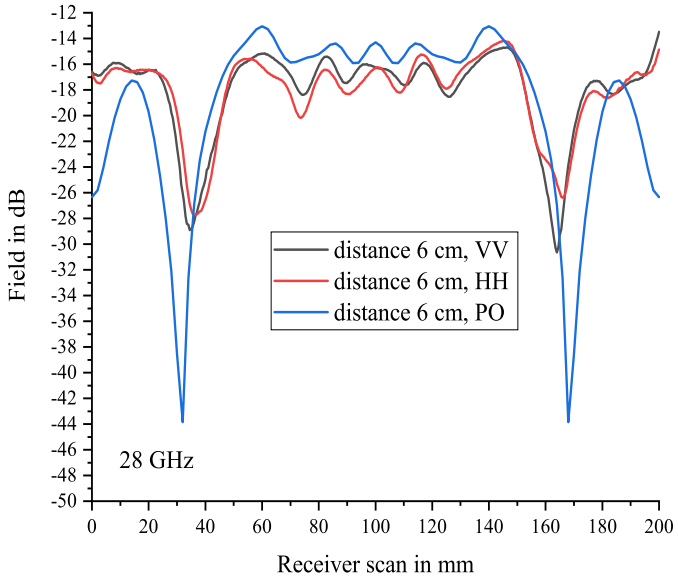

Figure 6.26 The same as in Fig. 6.25 but for 6 cm.

6.8 Design of a metalens with four concentric regions

This section decribes the design of a metalens for correcting the phase distortions of the hemispheric radome (from section 6.1 to 6.3). The metalens is designed as a metasheet divided into four circular concentric regions (Fig. 6.27). As seen from Fig. 6.27, the area of the regions 1 and 2 is greater than that of the region 3. The regions 1 and 2 become the main part of the metalens. These two regions should be as transparent as possible. The transmission coefficient of each region is extracted from the extended semianalytical approach (Chapter 4).

Table 6.2 shows the phase distribution along the diameter in the basis plane of the radome, calculated with GO. After arithmetic averaging is applied to phase values at each region, the constant phase values come out as shown in Table 6.3.

Table 6.2 Phase distribution calculated by ray tracing at observation points along the inner radius of the hemispheric radome at 28 GHz.

Distance from center in mm	Phase (from center) in degree	Phase (to edge) in degree
95 - 56	−83.553	−88.440
55 - 31	−88.719	−99.378
30 - 12	−100.052	−119.002
11 - 0	−120.697	−146.398

Table 6.3 Constant phase values for each region obtained by arithmetic averaging.

Regions	**Phases in degree**
1	$-85.146 \cong -85$
2	$-93.345 \cong -93$
3	$-108.247 \cong -108$
4	$-131.475 \cong -132$

In the design, the phase values between −153° and −178° observed close to the radome wall are not considered. As it is seen from Fig. 6.8, the phase rapidly changes close to the radome wall. To compensate this phase variation, narrow zones on the metalens would be necessary, comparable to the size of the unit cells. Furthermore, the full-wave simulations assume an infinite periodic planar structure, smaller finite width of the regions can decrease the accuracy of the results.

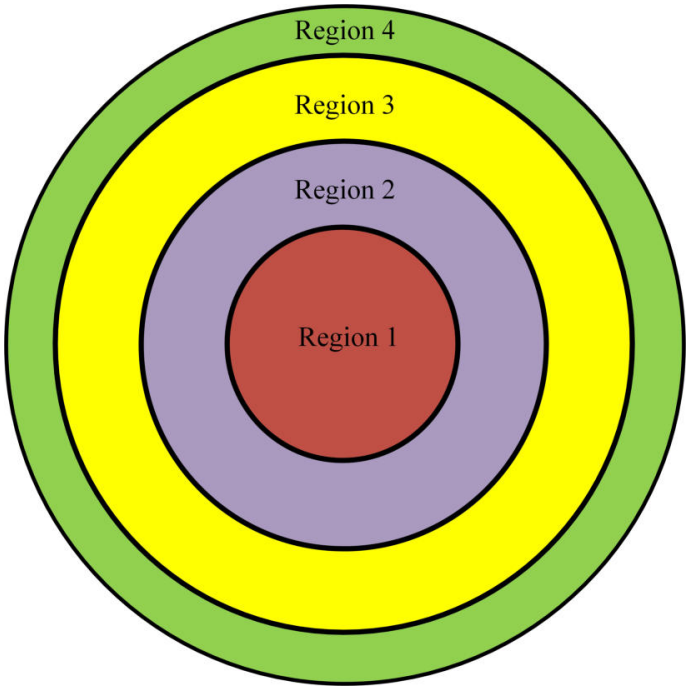

Figure 6.27 Metalens with four concentric regions placed at the basis of the radome [zOE20].

In the metalens design, the results of the extended semianalytical method in Section 4.10 are used. As it is seen in Fig. 6.29, the minimum amplitude of the transmission coefficient appears between 1.2 mm and 1.35 mm of the outer radius values. The outer radius for each region in the metalens should be chosen to give a phase value which is not close to the point where the phase jumps and the amplitude of the transmission coefficient should be as high as possible; therefore, the outer radius is chosen between 0.9 mm and 1.1 mm. As it is seen in Figs. 6.28 and 6.29, when the radius value is getting smaller, the phase and amplitude of the transmission coefficient are only weakly influenced by the value of the width. The radius values in the regions should not be too close to each other in order to simplify manufacturing the metalens. The calculated transmission coefficients are shown in Table 6.4. For correcting the phase distribution at the basis of the radome, the necessary phase values which should be created at each region of the metalens, are defined as shown in Table 6.5. The calculated and simulated values of the transmission coefficient are compared in Table 6.6 for the phase and in Table 6.7 for the amplitude.

In Fig. 6.30, the theoretically expected phase correction is shown. The discrete phase distribution is determined as arithmetic average of the calculated phase distortion by the radome for each region of the metalens. The constant phase value should be −221° after the metalens is combined with the radome.

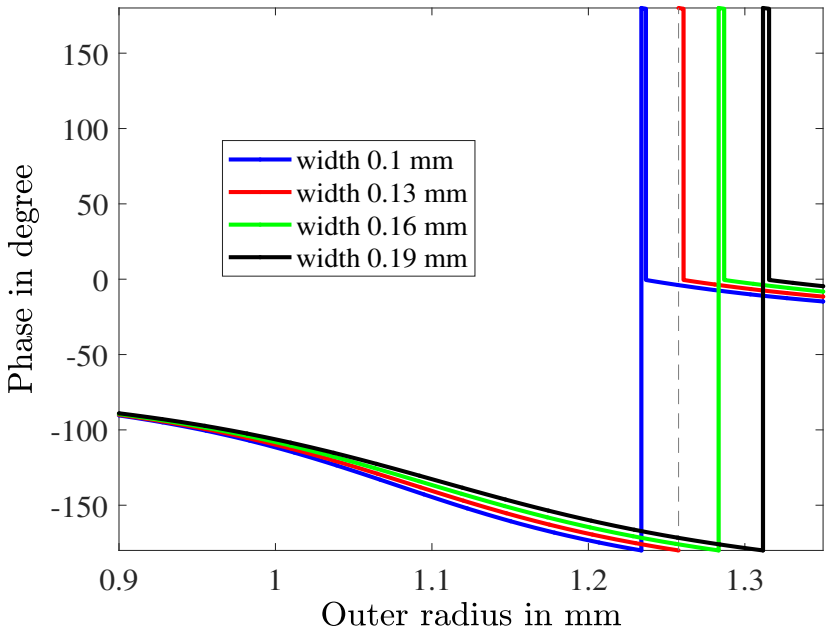

Figure 6.28 Phase of the transmission coefficient calculated with the semianalytical method as a function of the outer radius for different values of the width at 28 GHz.

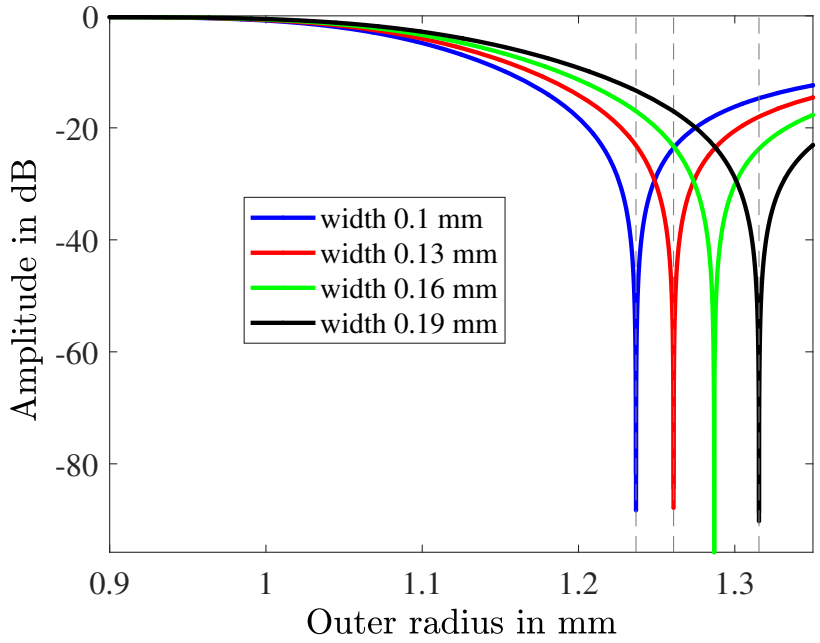

Figure 6.29 The same as in fig 6.28 but for the amplitude.

Table 6.4 Calculated transmission coefficient for each region of the metalens at 28 GHz.

Regions	Calculated complex T
1	$-0.4905-j0.4638$
2	$-0.4727-j0.6190$
3	$-0.3558-j0.8233$
4	$0.0174-j0.9728$

Table 6.5 Calculated phase values depending on the dimensions of the rings at 28 GHz.

Regions	Outer radius mm	Width mm	Phase of T in degree	T in dB
1	1.1	0.16	−136.599	−3.413
2	1.07	0.16	−127.365	−2.171
3	1.03	0.19	−113.371	−0.945
4	0.9	0.19	−88.974	−0.238

Table 6.6 Comparison of the approximate and full-wave simulated phase values of the transmission coefficient for each region of the metalens at 28 GHz.

Regions	Phase of T in degree, semianalytical	Phase of T in degree, full-wave simulation
1	−136.599	−135.983
2	−127.365	−127.394
3	−113.371	−114.630
4	−88.974	−91.493

Table 6.7 Comparison of approximate and full-wave simulated amplitude values of the transmission coefficient for each region of the metalens at 28 GHz.

Regions	Calculated $\|T\|$ in dB	Full-wave simulated $\|T\|$ in dB
1	−3.413	−3.361
2	−2.171	−2.199
3	−0.945	−1.043
4	−0.238	−0.264

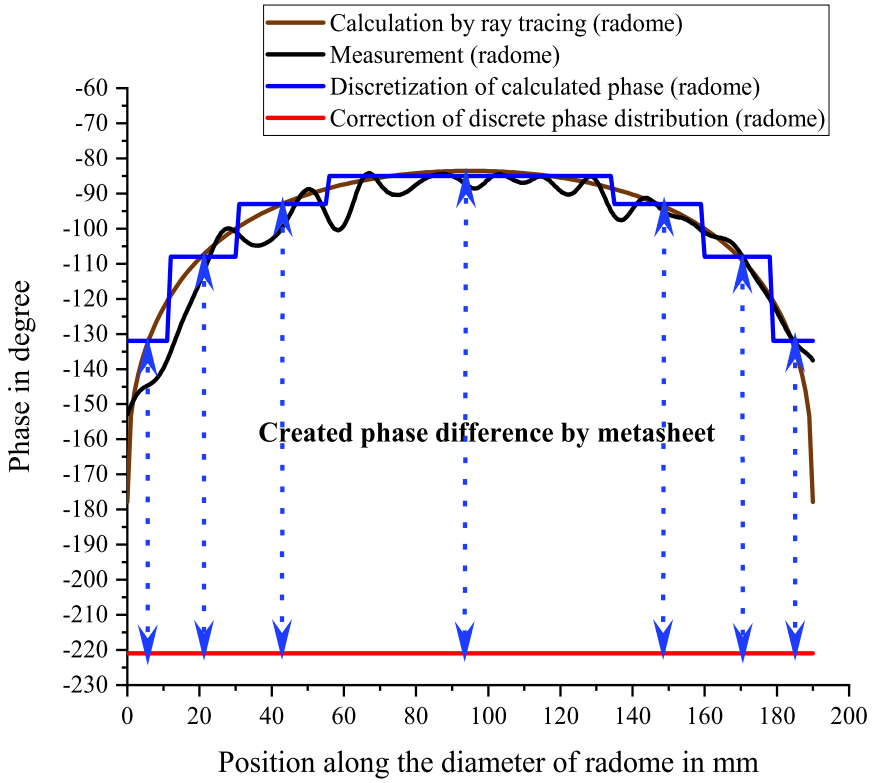

Figure 6.30 Calculated and measured phase values and the expected phase compensation by the metasheet as a function of the position along the diameter of the radome at 28 GHz [zOE20] [reproduced figure courtesy of The Electromagnetics Academy].

6.9 Measurement setup for the radome and the four-region metalens

In this section, the measurement setup is explained. The information about the used equipment is provided. The positions of the radome, holder, lens, transmit and receive antenna are shown in Fig. 6.31. A horn antenna with a lens is used as transmit antenna. The distance between the antenna and the lens is 162 cm. The distance between the holder and the receiving antenna (probe) is 6 cm. The probe moves horizontally along the diameter of the basis of the radome (receiving antenna scan). The distance between the lens and holder is 110 cm. In Fig. 6.34, the horn antenna is the transmit antenna which radiates to the radome through the lens. The lens helps to convert the incident wave into a plane wave. The incident wave is sent parallel to the axis of the radome. The polarization of the antennas is VV.

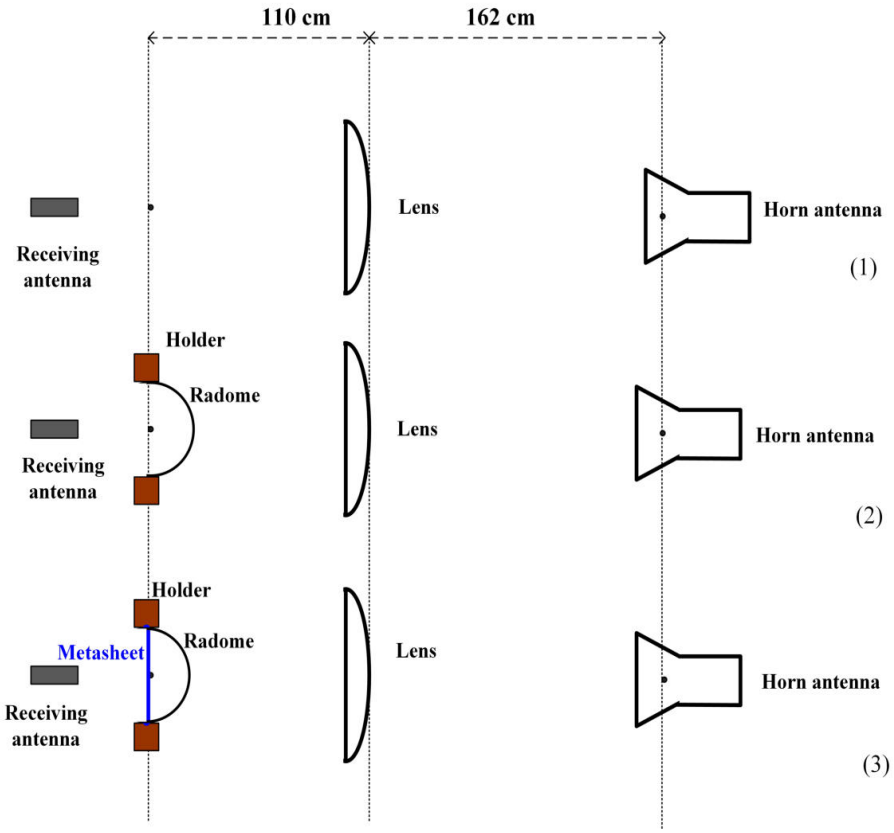

Figure 6.31 Three measurement configurations: (1) transmitting antenna, antenna lens and receiving antenna; (2) as configuration (1) but with radome on the holder; (3) as configuration (2) but with the metalens.

The material of the lens is polypropylene (PP) which is is a thermoplastic “addition polymer” made from the combination of propylene monomers. Polypropylene can be utilized for applica-

tions, where a higher transparency is required. The material is readily available and cheap. It has a relatively slithery surface [Meced]. The metalens is made as PCB (Printed Circuit Board) with the size 25 cm×25 cm. The border region on the plate is filled with the rings as in the fourth circular region (Fig. 6.32). The radome is positioned at the center of the metalens as shown in Fig. 6.33. The radome is positioned at the center of the metalens as shown in Fig. 6.33.

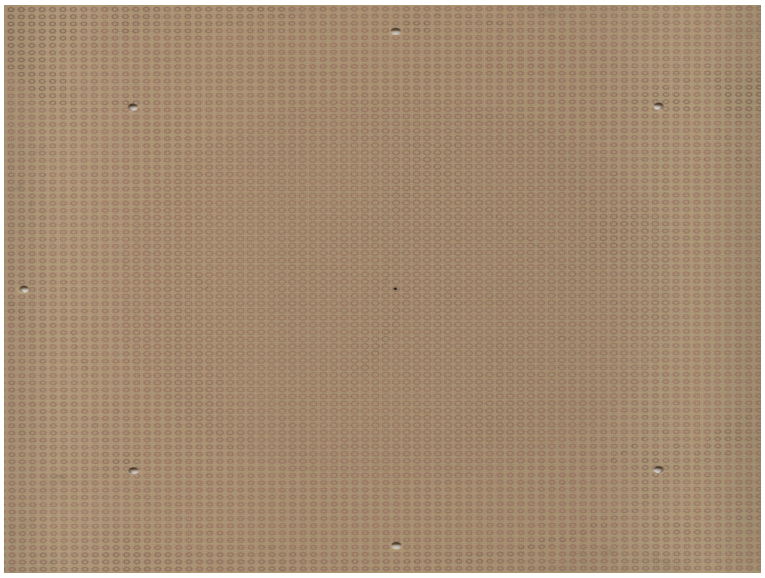

Figure 6.32 Manufactured metalens with four concentric regions filled with differently sized circular rings.

Figure 6.33 Metasheet and radome.

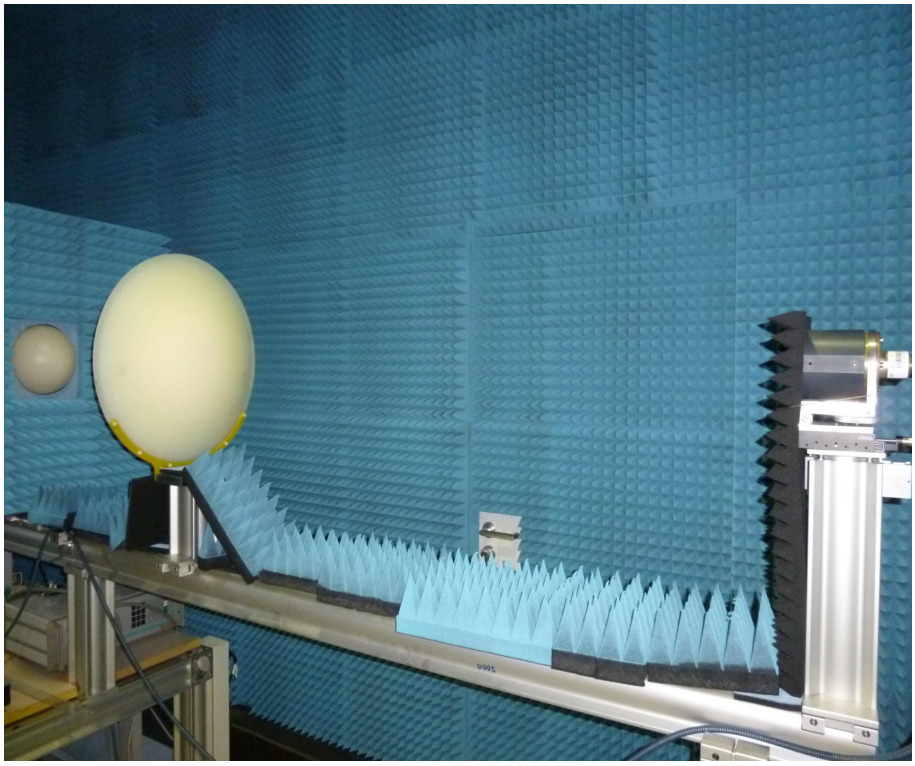

Figure 6.34 Measurement setup with an antenna lens and the radome on a holder.

6.10 Comparison of measured and calculated results for the radome and the metalens

In this section, the measured and calculated results are compared. The PO approach described in Section 6.5 is used for the calculation. The PO solution is derived for the metalens with four regions. In the PO calculation, the holder is modeled as a circular aperture in an impenetrable surface. In this aperture, the radome and metalens are positioned. In the PO solution, the incident electric field with $E_0 = 1$ is multiplied by the transmission coefficient of the radome and by the transmission coefficient of the metalens, from which the equivalent surface currents on the backside of the lens are calculated and inserted in the PO integral. The integration area is subdivided in small square pieces with the side length 5 mm. The amplitudes (in dB) of transmitted fields are normalized to the free-space values as

$$20\log(|E_d|) = 20\log(|E_{MSR}|) - 20\log\left(\left|E_p\right|\right), \tag{6.28}$$

$$20\log(|E_{dr}|) = 20\log(|E_R|) - 20\log\left(\left|E_p\right|\right), \tag{6.29}$$

where E_R is the electric field transmitted through the radome in the absence of the metalens. E_{MSR} is the electric field transmitted through the radome and metalens and E_p is the measured transmitted electric field in free space, i.e. without radome, metalens and holder. The normalization for the phase (in degree) is given

$$P(E_d) = P(E_{MSR}) - P(E_p), \tag{6.30}$$

$$P(E_{dr}) = P(E_R) - P(E_p), \tag{6.31}$$

where $P(E_R)$ is the phase of the electric field transmitted through the radome. $P(T_{MSR})$ is the phase of the electric field transmitted through the radome and metalens. $P(E_p)$ is the phase of transmitted electric field in free space, i.e. without radome, metalens and holder. When $P(E_d) < -180^o$, 360^o is added to the phase value. If $P(E_d) > 180^o$, 360^o is subtracted from the phase value. Additionally, 360^o is subtracted from all phase values $P(E_d)$ at 28, 29 and 29.5 GHz to compare with measured phase values of radome and with theoretically expected constant phase value -221^o easily. The measured and calculated values for the normalized amplitudes and phases are compared. The receiving antenna moves along the diameter of the radome at a distance of 6 cm behind the radome basis with a step used 0.5 mm.

The measured results for several frequencies from 27 GHz to 29.5 GHz are shown in Figs. 6.35 to 6.39. The metalens only slightly decreases the amplitude of the transmitted field but the effect of the metalens cannot be ignored as indicated in Figs. 6.35 and 6.36. Figure 6.37 shows the correction of the phase by the metalens. The corrected phase values are close to the expected theoretical phase value $-221°$ (Fig. 6.30). The bandwidth of the metalens is approximately 2.5 GHz. The oscillations observed in the curves are due to the holder, at which the radome and metalens are positioned in the measurement setup.

Figures 6.40 through 6.43 compare the measured and calculated results for the radome with and without the metalens. The frequency is equal to 28 GHz, the distance between the radome basis and the probe is equal to 6 cm, and the case of vertically polarized transmitting and receiving antennas is considered.

The PO calculation is done by using (6.23), (6.24) and (6.25). In the calculation, the holder effect is also included. A circular aperture in the square area 0.4 m$\times$ 0.4 m is defined.
The radius of the aperture is the same as the radius of the radome. The transmitted field on the aperture depends on the configuration (the presence of the radome and the metalens) and on the position on the aperture. The transmission coefficient for the part of the square area outside the radome basis is zero. In the PO calculation, the transmission coefficient of the metalens and the

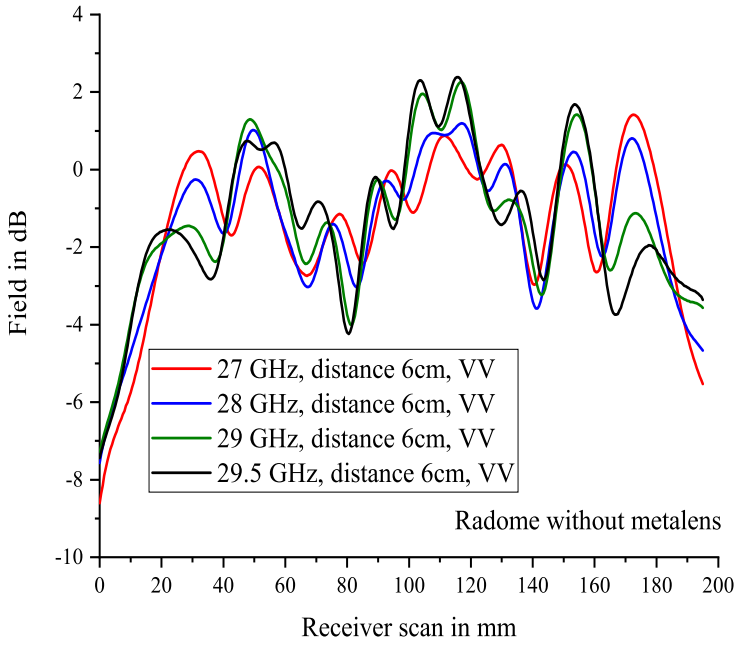

Figure 6.35 Measured amplitude of the field transmitted through the radome for the frequencies 27 GHz, 28 GHz, 29 GHz and 29.5 GHz.

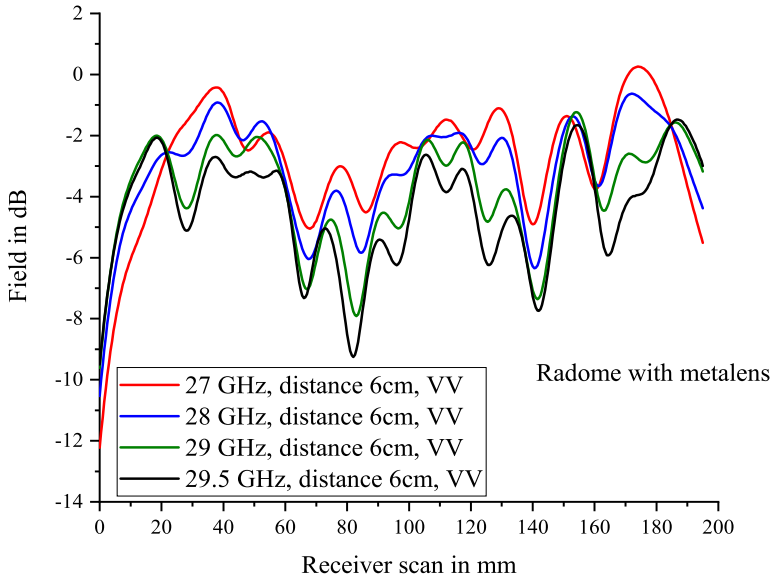

Figure 6.36 The same as in Fig. 6.35 but for the radome with metalens.

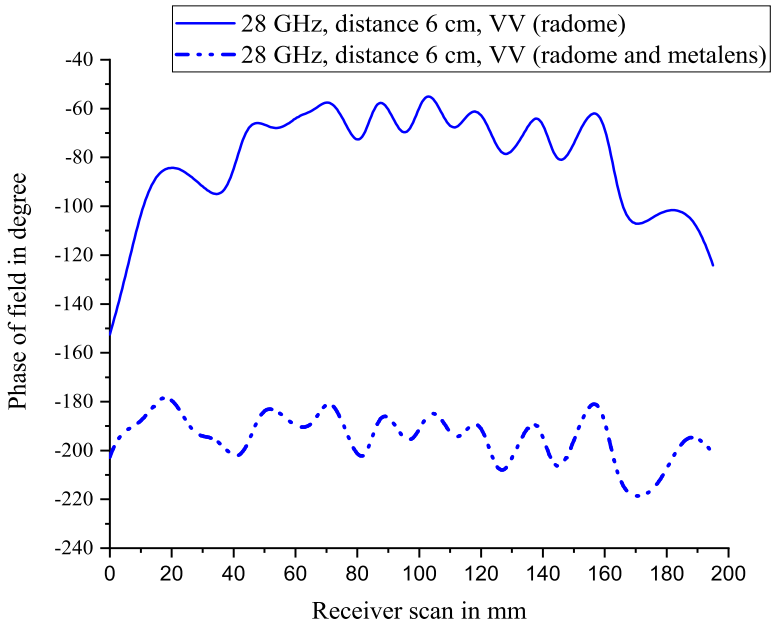

Figure 6.37 Measured phase of the field transmitted through the radome and metalens at the observation points at 28 GHz.

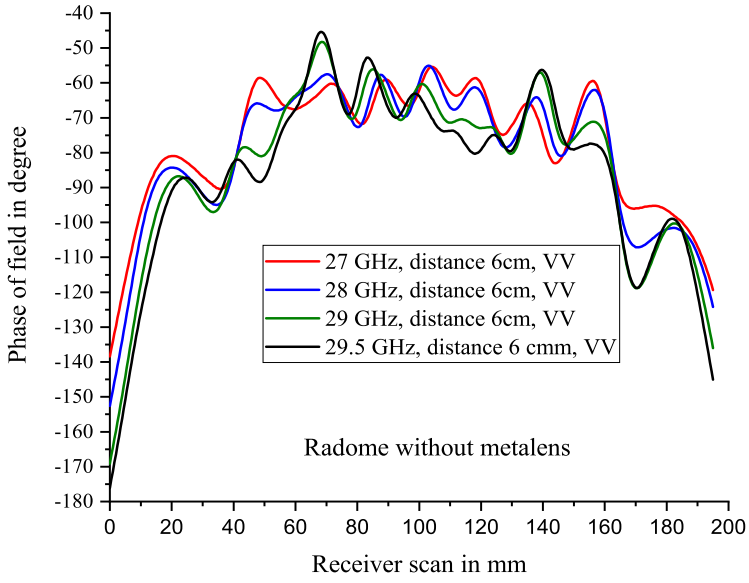

Figure 6.38 The same as in Fig. 6.35 but for the phase.

radome is defined for each facet. The transmitted field on the radome basis is calculated by ray

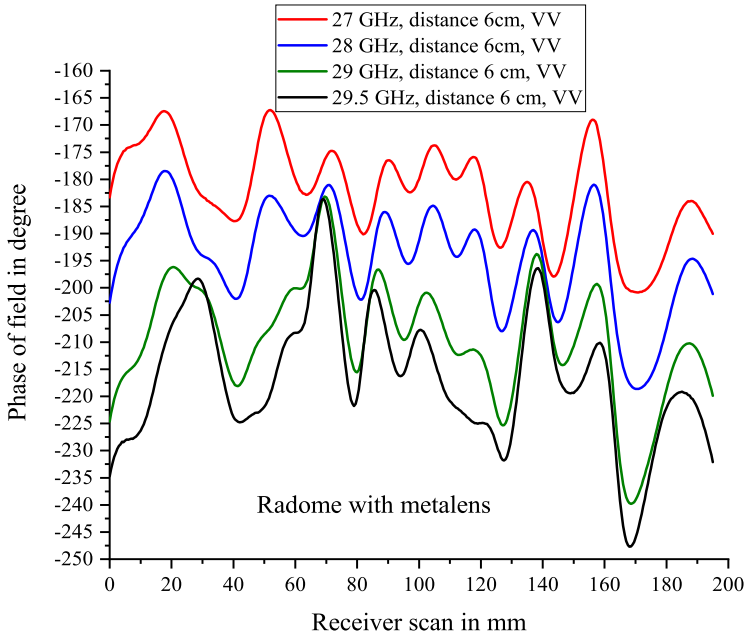

Figure 6.39 The same as in Fig. 6.38 but for the radome with metalens.

tracing along the radius of the basis of the radome. Ray tracing gives the transmission coefficient for a set of discrete points along the radius of the base of the radome. For the PO calculation, the transmission coefficient is needed at the center point of each facet in Fig. 6.12. The Matlab interpolation function is utilized to calculate the field transmitted through the radome at each facet over the basis of the radome. A spline interpolation function is chosen. As rotational symmetry is assumed throughout this calculation, only the distance between the facet's center and the origin is necessary to determine the transmitted field at every point on the radome basis with spline interpolation. The transmission coefficient of each region of the metalens, which is used in PO, is calculated by the extended semianalytical method. As it is seen from Figs. 6.40 to 6.43, there is a good match between the calculated and measured results.

Geometrical Optics can only be used to calculate the electric field close to the metalens. For calculation of the electric field at an observation point, which is further away from the metalens (Fresnel and Fraunhofer regions), PO should be used.

The Taylor series approximation can cause a decrease in the accuracy of the employed PO solution. The incident wave is also assumed as plane wave for simplification in the calculation. Adding higher-order terms to the Taylor series can increase the accuracy, but the surface integral for each facet cannot be calculated analytically. Another source of the errors in the PO solution are the jumps in material properties between the rings on the metalens, which result in deviation of the

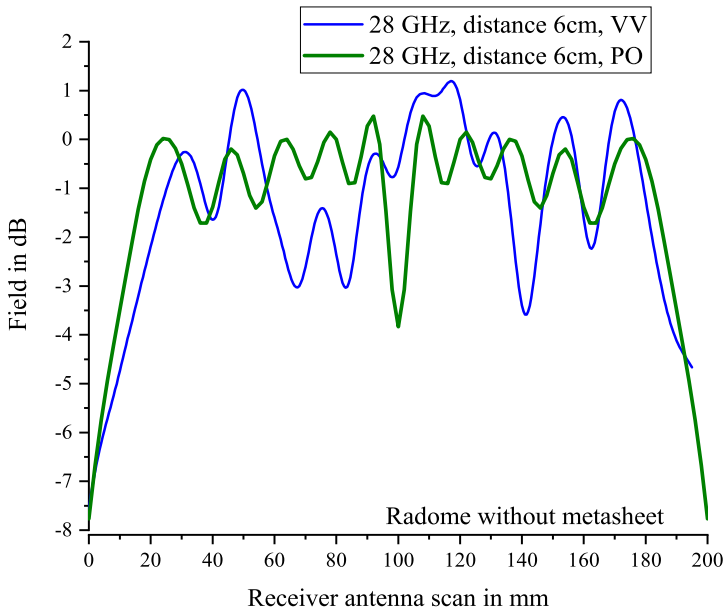

Figure 6.40 Comparison of calculated and measured field amplitudes for the radome without metalens.

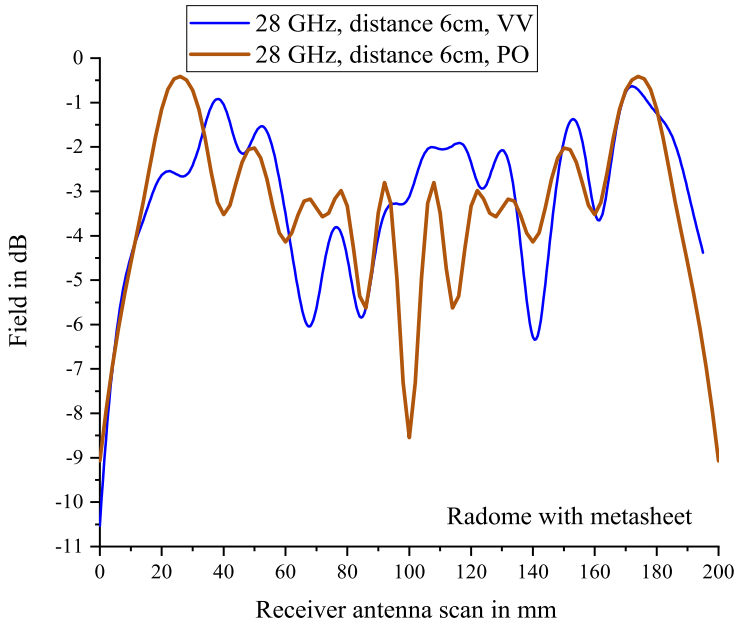

Figure 6.41 The same as in Fig. 6.40 but for the radome with metalens [zOE20] [reproduced figure courtesy of The Electromagnetics Academy].

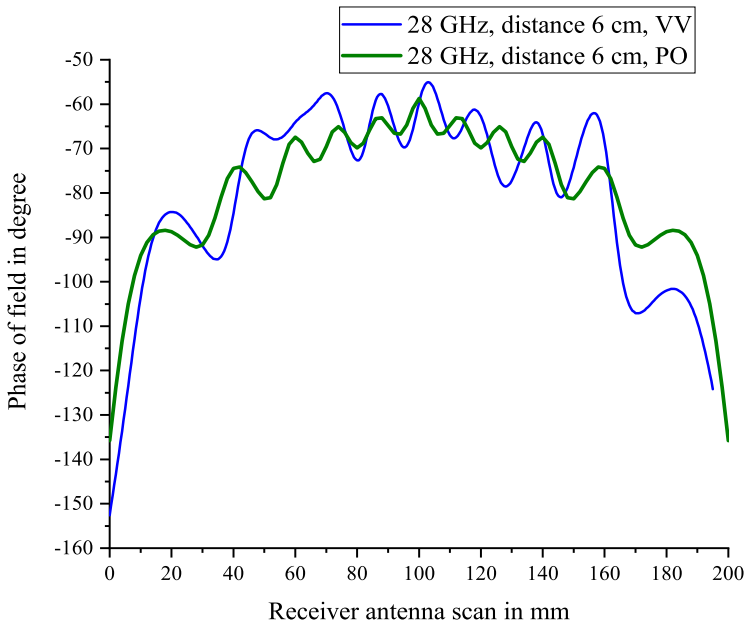

Figure 6.42 The same as Fig. 6.40 but for the phase [zOE20] [reproduced figure courtesy of The Electromagnetics Academy].

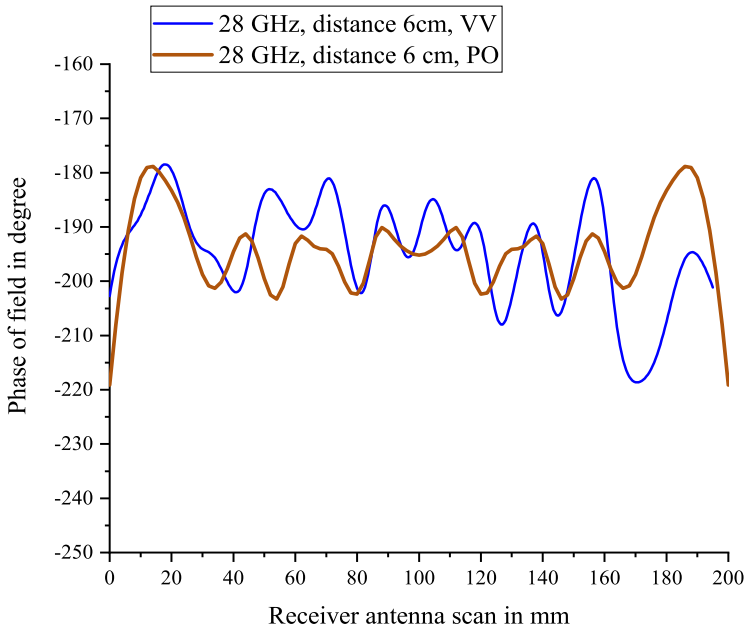

Figure 6.43 The same as in Fig. 6.42 but for the radome with metalens.

true field distribution from the GO field distribution. A further subdivision of the metalens into

concentric regions is limited by the size of the unit cells. As it is observed in Figs. 5.5 and 5.6, the PO solutions are insufficient when the metasheet cannot be considered homogeneous and large compared to the wavelength. Furthermore, dividing the metalens into more regions complicates the design of the metalens.

Chapter 7

Conclusion and Outlook

Electromagnetic metamaterials are artificial composites with a wide range of applications at microwave and optical frequencies. Metamaterials are used in different fields such as communication, radar and military. In this thesis, planar periodic transparent arrays of ring-shaped metal resonators on dielectric substrates were analyzed by using semianalytical methods, full-wave simulations and measurements. The focus was on such topics as analysis of transparent metasheets with an emphasis on the phase control, detailed parametric study of transmission and reflection at planar metamaterial arrays with circular rings as inclusions, a semianalytical method for rapid simulation of such arrays, development and application of PO based approaches to calculation of transmission through homogenized metasheets of finite size, design and experimental demonstration of a metalens for correction of the phase distortions caused by a hemispheric radome in the Ka frequency band.

Infinite periodic planar arrays of circular metal rings were analyzed because the circular ring is the simplest isotropic particle, which can be easily manufactured. In contrast to the square ring or Jerusalem cross, the circular ring is less studied in the literature. As it is shown in Fig. 2.6, the electric field is uniform between the square-shaped particles but this situation is not valid for circular rings; therefore, a simple transmission line equivalent model cannot be found.

A semianalytical approach was developed for the fast design of metasheets built from circular rings. In this approach, the equations for impedances of the equivalent circuit are parameterized and fitted to match the values of transmission coefficients obtained by full-wave simulations at selected frequency points. Full-wave simulations, for example with the finite element method, require large memory and long computation time. The advantages of the semianalytical approach are that it decreases the number of full-wave simulations and can be used for different frequency ranges and greater number of dimensional parameters of the resonators, which are demonstrated in the thesis. This approach can be applied for arrays of metal planar resonators with and without

dielectric substrate. The approach can be extended to anisotropic and bi-anisotropic resonators and to unit cells with lumped and/or active elements.The approach can be used as a design tool in engineering praxis.

The semianalytical approach was used for the design of a metalens for a hemispheric radome in the Ka band. The radome and metasheet must be electrically large to allow for a sufficiently large number of unit cells, which are necessary to replace the metasheet with effectively homogeneous material layers. For easiness of the production, the Ka band was selected for measurement and simulation. The designed metalens works well for the phase correction in the frequency range between 27 GHz and 29.5 GHz , which means a bandwidth of 2.5 GHz. Planar metalenses can be designed for differently shaped radomes by doing necessary modifications, because the phase distortions of the radomes depend on the shape of the radome.

The measured results are slightly unsymmetric with respect to the symmetry axis of the radome, which are explained by the limited sensitivity of the measurement facility in the Ka band. Small changes in the setup cause oscillations in the results. This should be improved. In this thesis, the distance between the electrically large scatterer and the observation point was defined experimentally by comparing the calculated and measured results. When the distance between the receiving antenna and metasheet decreases, it is observed that the accuracy of the measured results decreases. The correct choice of this distance is important to measure the electromagnetic response of each region of the metasheet separately and accurately.

The PO method is generally applied to electrically large dielectric or perfect electric conductor surfaces. In this study, PO was applied to electrically large planar metasheets, which are divided into square or concentric circular regions filled with electrically small metal rings. In order to decrease the complexity of the simulations, the shape was chosen as planar, but the PO method can be used for curved shapes too. The measured and calculated results matched well. This result shows that the PO solution, despite the approximations used in this study, is sufficiently accurate to predict the electromagnetic response of transparent metasheets, even of those composed of several subregions.

As a future work, curved metasheets can be designed and used directly as a surface of the radome. The material of the metasheet should be chosen to make the radome sustainable in heavy weather conditions. For example, Polyurethane foam can be an option as a material for the radome, because it has good dielectric properties and at the same time, good structural strength [Mey15]. The type of the material depends on the type of the radome and its application area. Polyurethane foam can be used in aerospace applications. Teflon coated Fiberglass (TSFG)

can also be chosen as a material for radomes to protect antennas on airborne platforms [BIA+17]. Such antennas face heavy environmental conditions such as aerodynamic load, variable temperature and pressure. For broadband applications, multilayer radomes can be designed. Working on the semianalytical method further to include the relative permittivity of the dielectric substrate as a parameter for controlling the electromagnetic response is necessary, because it will help to reduce the number of full-wave simulations for structures involving dielectric substrates. The case of a plane wave incident obliquely on the radome should also be analyzed to account for additional reflections from the walls of the radome.

Appendix A

Derivation of Surface Integral for a Single Facet

The calculation of the surface integral in (6.25) is explained here. Ω_n is the integration surface (Fig. 6.12). Let x and y be new coordinates, not necessarily orthogonal, measured along two nonparallel edges of the integration region, such that the vector r_1. The boundaries of the line integrals are 0.5 and −0.5, because (A.1) is parameterized according to center of facet ($\mathbf{r_{cn}}$). $d\Omega$ is expressed in terms of $\mathrm{d}x\,\mathrm{d}y$ as [Here the upper equation (A.3)]. The vector $\mathbf{r_1}$ which is the position vector on the surface area, is described as

$$\mathbf{r_1} = \mathbf{r_{cn}} + a_n x\,\hat{u}_x + b_n y\,\hat{u}_y, \tag{A.1}$$

where $-0.5 < x < 0.5$, $-0.5 < y < 0.5$, $a_n\hat{u}_x = \mathbf{r_{2n}} - \mathbf{r_{1n}}$, $b_n\hat{u}_y = \mathbf{r_{3n}} - \mathbf{r_{2n}}$,and $\hat{u}_x$, $\hat{u}_y$ are the unit vectors along the selected edges of the integration region. Defining $|\mathbf{r} - \mathbf{r_1}| = R(\mathbf{r_1})$, equation (6.25) is expressed as

$$\iint_{\Omega_n} e^{-jk_0R(\mathbf{r_1})} \left| \frac{\partial \mathbf{r_1}}{\partial x} \times \frac{\partial \mathbf{r_1}}{\partial y} \right| \mathrm{d}x\,\mathrm{d}y, \tag{A.2}$$

where

$$\left| \frac{\partial \mathbf{r_1}}{\partial x} \times \frac{\partial \mathbf{r_1}}{\partial y} \right| \mathrm{d}x\,\mathrm{d}y = a_n b_n \mathrm{d}x\,\mathrm{d}y = \mathrm{d}\Omega. \tag{A.3}$$

Assuming that the integration region is small, a Taylor approximation can be used in the phase part of the exponential function as

$$R(\mathbf{r_1}) \approx R(\mathbf{r_{cn}}) + (\mathbf{r_1} - \mathbf{r_{cn}}) \nabla R(\mathbf{r_1})|_{\mathbf{r_{cn}}}, \tag{A.4}$$

where $\nabla R(\mathbf{r_1})$ is expressed as

$$\nabla R(\mathbf{r_1}) = \nabla |\mathbf{r} - \mathbf{r_1}| = \frac{\mathbf{r} - \mathbf{r_1}}{|\mathbf{r} - \mathbf{r_1}|}. \tag{A.5}$$

Equation (A.5) is inserted in (A.4) and it is written as

$$\begin{aligned} R(\mathbf{r_1}) &\approx R(\mathbf{r_{cn}}) + (\mathbf{r_1} - \mathbf{r_{cn}}) \frac{\mathbf{r} - \mathbf{r_1}}{|\mathbf{r} - \mathbf{r_1}|}\bigg|_{\mathbf{r_{cn}} = \mathbf{r_1}} \\ &\approx R(\mathbf{r_{cn}}) + (\mathbf{r_1} - \mathbf{r_{cn}}) \frac{\mathbf{r} - \mathbf{r_{cn}}}{|\mathbf{r} - \mathbf{r_{cn}}|}, \\ &\approx R(\mathbf{r_{cn}}) + (\mathbf{r_1} - \mathbf{r_{cn}}) \cdot \hat{s}_{cn}, \end{aligned} \tag{A.6}$$

where $\hat{s}_{cn} = \frac{\mathbf{r} - \mathbf{r_{cn}}}{|\mathbf{r} - \mathbf{r_{cn}}|}$. Equation (A.6) is inserted in the phase part of exponential function in (A.2) to give

$$e^{-jk_0 R(\mathbf{r_1})} = e^{-jk_0 (R(\mathbf{r_{cn}}) + (\mathbf{r_1} - \mathbf{r_{cn}}) \cdot \hat{s}_{cn})} \tag{A.7}$$

and (A.2) becomes

$$e^{-jk_0 R(\mathbf{r_{cn}})} e^{jk_0 \mathbf{r_{cn}} \cdot \hat{s}_{cn}} \iint_{\Omega_n} e^{-jk_0 \mathbf{r_1} \cdot \hat{s}_{cn}} \mathrm{d}\Omega. \tag{A.8}$$

Inserting (A.1) in (A.8) results in the equations

$$\begin{aligned} e^{-jk_0 R(\mathbf{r_{cn}})} e^{jk \mathbf{r_{cn}} \cdot \hat{s}_{cn}} \iint_{\Omega_n} e^{-jk_0 (\mathbf{r_{cn}} + a_n x \hat{u}_x + b_n y \hat{u}_y) \cdot \hat{s}_{cn}} \mathrm{d}\Omega = \\ e^{-jk_0 R(\mathbf{r_{cn}})} \iint_{\Omega_n} e^{-jk_0 (a_n x \hat{u}_x + b_n y \hat{u}_y) \cdot \hat{s}_{cn}} \mathrm{d}\Omega. \end{aligned} \tag{A.9}$$

Using (A.3), equation (A.9) becomes a Riemann integral

$$a_n b_n e^{-jk_0 R(\mathbf{r_{cn}})} \iint_{\Omega_n} e^{-jk_0 a_n x \hat{u}_x \cdot \hat{s}_{cn}} e^{-jk_0 b_n y \hat{u}_y \cdot \hat{s}_{cn}} \mathrm{d}x \mathrm{d}y. \tag{A.10}$$

The integral is written as the product of two one-dimensional integrals according to

$$a_n b_n e^{-jk_0 R(\mathbf{r_{cn}})} \int_{0.5}^{-0.5} e^{-jk_0 a_n x \hat{u}_x \cdot \hat{s}_{cn}} \mathrm{d}x \int_{0.5}^{-0.5} e^{-jk_0 b_n y \hat{u}_y \cdot \hat{s}_{cn}} \mathrm{d}y. \tag{A.11}$$

Both integrals are calculated in the same way, so let us consider the integral with respect to x:

$$\int_{0.5}^{-0.5} e^{-jk_0 a_n x \hat{u}_x \cdot \hat{s}_{cn}} \mathrm{d}x = \frac{1}{-jk_0 a_n \hat{u}_x \cdot \hat{s}_{cn}} (e^{-jk_0 \frac{1}{2} a_n \hat{u}_x \cdot \hat{s}_{cn}} - e^{jk_0 \frac{1}{2} a_n \hat{u}_x \cdot \hat{s}_{cn}}). \tag{A.12}$$

Using

$$\sin(\alpha) = \frac{e^{j\alpha} - e^{-j\alpha}}{2j} \tag{A.13}$$

and the definition of the sinc function

$$\mathrm{sinc}(\alpha) = \frac{\sin(\alpha)}{\alpha}, \tag{A.14}$$

equation (A.12) becomes

$$\int_{0.5}^{-0.5} e^{-jk_0 a_n x \hat{u}_x \cdot \hat{s}_{cn}} \mathrm{d}x = \frac{\sin\left(k_0 \frac{1}{2} a_n \hat{u}_x \cdot \hat{s}_{cn}\right)}{k_0 \frac{1}{2} a_n \hat{u}_x \cdot \hat{s}_{cn}}$$
$$= \mathrm{sinc}(\frac{1}{2} k_0 a_n \hat{u}_x \cdot \hat{s}_{cn})$$
$$= \mathrm{sinc}(\frac{1}{2} k_0 (\mathbf{r_{2n}} - \mathbf{r_{1n}}, \hat{s}_{cn})). \tag{A.15}$$

After applying the same calculation process to the second integral in (A.11), the surface integral calculation is completed and leads to

$$\iint_{\Omega_n} e^{-jk_0|\mathbf{r}-\mathbf{r_1}|} d\Omega \cong a_n b_n \mathrm{sinc}(\frac{k_0}{2}(\mathbf{r_{2n}} - \mathbf{r_{1n}}, \hat{s}_{cn}))\mathrm{sinc}(\frac{k_0}{2}(\mathbf{r_{3n}} - \mathbf{r_{2n}}, \hat{s}_{cn}))e^{-jk_0|\mathbf{r}-\mathbf{r_{cn}}|}. \tag{A.16}$$

Appendix B

Asymptotic Evaluation of a PO Integral

The derivation of integral calculation for (5.19) in Section 5.3 is explained here. The integral is written in a compact form as

$$E_{tr}^{rim} = E_0 \frac{jk_0}{4} \int_{x(a)}^{+\infty} e^{-jk_0 x} A(x)\, dx \tag{B.1}$$

and

$$dx = \frac{\rho_1 d\rho_1}{\sqrt{\rho_1^2 + z^2}}. \tag{B.2}$$

In (B.1), $x = \sqrt{\rho_1^2 + z^2}$, and $A(x)$ becomes

$$A(x) = 2 + \frac{2z}{\sqrt{\rho_1^2 + z^2}} - \frac{\rho_1^2}{\rho_1^2 + z^2}. \tag{B.3}$$

The derivative of the exponential function with respect to x is calculated as

$$\frac{\partial e^{-jk_0 x}}{\partial x} = -jk_0 e^{-jk_0 x} \tag{B.4}$$

and

$$e^{-jk_0 x} = -\frac{1}{jk_0} \frac{\partial e^{-jk_0 x}}{\partial x}. \tag{B.5}$$

Inserting (B.5) in (B.1) gives

$$E_{tr}^{rim} = E_0 \frac{jk_0}{4} \int_{x(a)}^{+\infty} -\frac{1}{jk_0} \frac{\partial e^{-jk_0 x}}{\partial x} A(x)\, dx. \tag{B.6}$$

Integration by parts is applied to (B.6) as

$$E_{tr}^{rim} = -\frac{E_0}{4} e^{-jk_0 x} A(x)\Big|_{x(a)}^{+\infty} + \frac{E_0}{4} \int_{x(a)}^{+\infty} e^{-jk_0 x} \frac{\partial A(x)}{\partial x}\, dx. \tag{B.7}$$

The second term in the right-hand side of (B.7) is $O(\frac{1}{k_0})$ and can be neglected in the high-frequency limit, because it describes asymptotically smaller terms. The integration of the exponent brings a large parameter k_0 in the denominator in front of the integral. So (B.7) becomes

$$E_{tr}^{rim} = -\frac{E_0}{4} e^{-jk_0 x} A(x)\Big|_{x(a)}^{+\infty}. \tag{B.8}$$

The contribution from infinity is equal to zero, and (B.8) recovers (5.20).

Bibliography

[AGK15] A. Ahmed, I. A. Goldthorpe, and A. K. Khandani. Electrically tunable materials for microwave applications. *Applied Physics Reviews*, 2(1), 2015.

[Agued] Art Aguayo. Analyzing advances in antenna materials @ONLINE. https://www.rogerscorp.com/documents/1796/acm/articles/analyzing-advances-in-antenna-materials.pdf, 2018 (accessed).

[AMC94] Dr. V. P. Pyati A. M. Capt. Radome depolarization and phase front distortion effects on boresight error prediction. pages pp. 177–182. Proceedings of IEEE National Radar Conference, (1994).

[And75] I. Anderson. On the theory of self-resonant grids. *The Bell System Technical Journal*, 54:pp. 1725–1731, 1975.

[ANSeda] ANSYS. Hfss open regions@ONLINE. https://www.ansys.com/-/media/ansys/corporate/resourcelibrary/techbrief/ab-hfss-open-regions.pdf, 2019 (accessed).

[Ansedb] Ansys. Lecture 9: Unit cell analysis (infinite array)@ONLINE. http://www.ece.uprm.edu/~rafaelr/inel6068/HFSS/HFSS_Antenna_v2015_v1/lectures_trainee/ANSYS_HFSS_Antenna_L09_0_Unit_Cell.pdf, 2019 (accessed).

[Anyed] Ansys HFSS @ONLINE. https://www.ansys.com/products/electronics/ansys-hfss, 2018 (accessed).

[ARA17] M. A. Antoniades, S. A. Rezaeieh, and A. M. Abbosh. Bandwidth and directivity enhancement of metamaterial-loaded loop antennas for microwave imaging applications. International Workshop on Antenna Technology: Small Antennas, Innovative Structures, and Applications (iWAT), (2017).

[Bah03] I. Bahl. *Lumped Elements for RF and Microwave Circuits*. Artech House, (2003).

[Bal05] C. A. Balanis. *Antenna Theory: Analysis and design*. Wiley, New York, (2005).

[BBM+16] M. Barbuto, F. Bilotti, A. Monti, D. Ramaccia, and A. Toscano. Engineered electromagnetic surfaces and their applications. In A. Tiwari, R. Wang, and B. Wei, editors, *Advanced Surface Engineering Materials*. Wiley Scrivener Publishing, New York, (2016).

[BIA+17] L. Boskovic, M. Ignatenko, C. Andrews, R. Hasse, and D. S. Filipovic. Electromechanical analysis of flat radomes for airborne antennas at K Ka V-band. pages 497 – 498. IEEE International Symposium on Antennas and Propagation and USNC/URSI National Radio Science Meeting, (2017).

[BIR08] A. Bondeson, P. Ingelstrom, and T. Rylander. *Computational Electromagnetics*. Springer, New York and London, second edition, (2008).

[BKGA11] P. P. Bhattacharya, R. Khandelwal, R. Gera, and A. Agarwal. Smart radio spectrum management for cognitive radio. *International Journal of Distributed and Parallel Systems (IJDPS)*, 2(4):12 pages, 2011.

[BL05a] A. Boag and C. Letrou. Multilevel fast physical optics algorithm for radiation from non-planar apertures. *IEEE Transactions on Antenna and Propagation*, 53(6):pp. 2064–2072, 2005.

[BL05b] R. J. Burkholder and T. Lee. Computation of radiation patterns involving numerical double integration. *IEEE Transactions on Antenna and Propagation*, 53(5):pp. 1843–1845, 2005.

[BM12] M. Blaha and J. Machac. Planar resonators for metamaterials. *Radioengineering*, 21(3):pp. 852–859, 09 2012.

[BMea11] D. Bouyge, D. Mardivirin, and J. Bonache et al. Split ring resonators (srrs) based on micro-electro-mechanical deflectable cantilever-type rings: Application to tunable stopband filters. *IEEE Microwave and Wireless Components Letters*, 21(5):pp. 243–245, 2011.

[Boa04] A. Boag. A fast physical optics (FPO) algorithm for high frequency scattering. *IEEE Transactions on Antenna and Propagation*, 52(1):pp. 197–204, 2004.

[Boo46] H. G. Booker. Slot aerials and their relation to complementary wire aerials (Babinet's principle). *Journal of the Institution of Electrical Engineers - Part IIIA: Radiolocation*, 93(4):pp. 620–626, 1946.

[BRAJ06] X. L. Bao, G. Ruvio, M. J. Ammann, and M. John. A novel gps patch antenna on a fractal hiimpedance surface substance. *IEEE Antennas Wirel Propag Lett*, 5:pp. 323–326, 2006.

[Broed] R. G. Brown. Green's function for the wave equation @ONLINE. https://webhome.phy.duke.edu/~rgb/Class/phy319/phy319/node75.html, 2007 (2018 accessed).

[BSU69] J.J. Bowman, T.B.A. Senior, and P.L.E. Uslenghi. *Electromagnetic and Acoustic Scattering by Simple Shapes*. Elsevier Science Publishing Co Inc.,U.S., (1969).

[BW99] M. Born and E. Wolf. *Principles of Optics: Electromagnetic Theory of Propagation, Interference and Diffraction of Light*. Cambridge University Press, (1999).

[Cah93] D. Cahan. *Hermann von Helmholtz and The Foundations of Nineteeth Century Science*. University of California Press, (1993).

[Cap09] F. Capolino. *Handbook of Metamaterials: Theory and Phenomena of Metamaterials*. CRC Press, Taylor and Francis Group, (2009).

[CB16] S. Chalia and M. K. Bharti. Mathematical modeling of ogive forebodies and nose cones. *International Research Journal of Engineering and Technology (IRJET)*, 3:pp. 744–747, (2016).

[Cened] Metamaterials Commercialization Center. Technology @ONLINE. http://metamaterialscenter.com/technology/, 2018 (accessed).

[Cha88] R. Chatterjee. *Antenna theory and practice*. John Wiley and Sons, (1988).

[CHD09] H. Chen, X. Hou, and L. Deng. Design of frequency-selective surfaces radome for a planar slotted waveguide antenna. *IEEE Antennas and Wireless Propagation Letters*, 8:pp. 1231–1233, 2009.

[CI94] P. W. Cramer and W. A. Imbriale. Speed up of near-field physical optics scattering calculations by use of the sampling theorem. *IEEE Transactions on Magnetics*, 30(5):pp. 3156–3159, 1994.

[CM12] F. Costa and A. Monorchio. A frequency selective radome with wideband absorbing properties. *IEEE Transactions on Antennas and Propagation*, 60:pp. 2740–2747, 2012.

[Col60] R. E. Collin. *Field Theory of Guided Waves*. McGraw-Hill, New York, (1960).

[Col92] R. E. Collin. *Foundations for Microwave Engineering*. McGraw Hill Education; 2nd edition, New York, (1992).

[Coo11] J. Coonrod. Understanding when to use FR4 or high frequency laminates. *On Board Technology, (www.Onboard-Technology.com)*, 2011.

[Coreda] Ansoft Corporation. Ansoft maxwell 3d @ONLINE. http://ansoft-maxwell.narod.ru/en/CompleteMaxwell3D_V11.pdf, 2019 (accessed).

[Coredb] Rogers Corporation. Rt/duroid laminates@ONLINE. https://www.rogerscorp.com/acs/producttypes/6/RTduroid-Laminates.aspx, 2018 (accessed).

[CPL91] P. Callaghan, E. A. Parker, and R. J. Langley. Influence of supporting dielectric layers on the transmission properties of frequency selective surfaces. *IEE Proceedings—H, Microwaves,Antennas and Propagation*, 138(5), 1991.

[CR12] S. Chakrabarti and S. Ramakrishna. Magnetic response of split ring resonator metamaterials: From effective medium dispersion to photonic band gaps. 78:pp. 483–492, (2012).

[Cra91] G. D. Crabtree. A numerical quadrature technique for physical optics scattering analysis. *IEEE Transactions on Magnetics*, 27(5):pp. 4291–4294, 1991.

[CRT81] G.A.E. Crone, A.W. Rudge, and G.N. Taylor. Design and performance of airborne radomes: a review. pages 451 – 464. IEE Proceedings F - Communications, Radar and Signal Processing, (1981).

[CSL09] T. J. Cui, D. Smith, and R. Liu. *Metamaterials: Theory, Design, and Applications*. Springer Publishing Company, Incorporated, (2009).

[Cui17] T. J. Cui. Microwave metamaterials—from passive to digital and programmable controls of electromagnetic waves. *Journal of Optics*, 19:pp. 1–16, 2017.

[CWR+06] H. Chen, B. I. Wu, L. Ran., T.M. Grzegorczyk, and J.A. Kong. Controllable left-handed metamaterial and its application to a steerable antenna. *Appl. Phys. Lett.*, 89(053509):pp. 1–3, 2006.

[Das15] S. Dasgupta. Polymer matrix composites for electromagnetic applications in aircraft structures. *Journal of the Indian Institute of Science*, 95(31):pp. 275–296, 2015.

[DeLed] Jean-Jacques DeLisle. What are the differences between various em-simulation numerical methods? @ONLINE. https://www.mwrf.com, 2018 (accessed).

[Die13] K. Diest, editor. *Numerical Methods for Metamaterial Design*. Springer Science and Business Media, Dordrecht Heidelberg New York London, (2013).

[Dined] S. Dinesh. What is hfss @ONLINE. https://de.scribd.com/document/149888010/What-is-HFSS, 2018 (accessed).

[DPC14] T. Debogovic and J. Perruisseau-Carrier. Mems-reconfigurable metamaterials and antenna applications. *International Journal of Antennas and Propagation*, 2014(138138):8 pages, 2014.

[DSNP+12] M. Durán-Sindreu, J. Naqui, F. Paredes, J. Bonache, and F. Martín. Electrically small resonators for planar metamaterial, microwave circuit and antenna design: A comparative analysis. *Applied Sciences*, 2(2):pp. 375–395, 04 2012.

[ea06] T. Driscoll et. al. Free space microwave focusing by a negative-index gradient lens. *Applied Physics Letters*, 88(081101), 2006.

[ea07a] R. B. Greegor et. al. Microwave focusing and beam collimation using negative index of refraction lenses. *IET Microwaves, Antennas and Propagation*, 1(1):pp. 108–115, 2007.

[ea07b] T. Zentgraf et al. Babinet's principle for optical frequency metamaterials and nanoantennas. *Phys. Rev. B*, 76:033407, 2007.

[ea10] R. Melik et al. Nested metamaterials for wireless strain sensing. *IEEE Journal of Selected Topics in Quantum Electronics*, 16(2):pp. 450–458, 2010.

[ea12a] F. Aieta et al. Aberration-free ultrathin flat lenses and axicons at telecom wavelengths based on plasmonic metasurfaces. *Nano Letters*, 12(9):pp. 4932–4936, 2012.

[ea12b] H. Zhou et. al. Filter-antenna consisting of conical fss radome and monopole antenna. *IEEE Transactions on Antennas and Propagation*, 60:pp. 3040–3045, 2012.

[ea13] A. Ebrahimi et al. Interlayer tuning of x-band frequency-selective surface using liquid crystal. In *Proceedings of 3rd Asia-Pacific Microwave Conference, APMC, Korea*, page 1118–1120. IEEE, (2013).

[ea15] V. S. Asadchy et. al. Broadband reflectionless metasheets, frequency selective transmission and perfect absorption. *Phys. Rev. X*, 5(3):pp. 1–10, 2015.

[ea16a] M. Khorasaninejad et. al. Metalenses at visible wavelengths: Diffraction-limited focusing and subwavelength resolution imaging. *Science*, 352(6290):pp. 1190–1194, 2016.

[ea16b] Y. M. Wu et al. A frequency independent method for computing the physical optics based electromagnetic fields scattered from a hyperbolic surface. *IEEE Transactions on Antenna and Propagation*, 64(4):pp. 1546–1552, 2016.

[Edged] David Edgar. Hybrid fe-bi for efficient simulation of radiation and scattering@ONLINE. https://support.ansys.com/staticassets/ANSYS%20UK/staticassets/FEBI_HFSSUGM_UK_2011.pdf, 2019 (accessed).

[EH96] T. Eibert and V Hansen. Calculation of unbounded field problems in free space by a 3D FEM/BEM-hybrid approach. *Journal of Electromagnetic Waves and Applications*, 10(1):pp. 61–78, 1996.

[Eib04] T. F. Eibert. Iterative-solver convergence for loop-star and loop-tree decompositions in method-of-moments solutions of the electric-field integral equation. *IEEE Antennas and Propagation Magazine*, 46(3):pp. 80–85, 2004.

[Erd56] A. Erdélyi. *Asymptotic Expansions*. Dover Publications, (1956).

[Fre00] A. Fresnel. *Memoir of the diffraction of light in The Wave Theory of Light Memoirs by Huygens, Young and Fresnel*. H. Crew.New York, USA: American Book Company, (1900).

[Galed] Galileognss. Galileo frequency bands @ONLINE. https://galileognss.eu/galileo-frequency-bands/, 2018 (accessed).

[Gaved] H. P. Gavin. The Levenberg-Marquardt method for nonlinear least squares curve-fitting problems @ONLINE. https://www.semanticscholar.org/paper/The-Levenberg-Marquardt-method-for-nonlinear-least-Gavin/1829418bae60a0b9f6efa38005b9f527be6e9570, 2013 (2019 accessed).

[Gla89] S. A. Glassner. *An Introduction to Ray Tracing*. Morgan Kaufmann Publishers, Inc. (Copyright Elsevier), pages:35,36,37,137,138,139,140, (1989).

[GPG14] K. Gangwar, Dr. Paras, and Dr. R.P.S. Gangwar. Metamaterials: characteristics, process and applications. *Advance in Electrical and Electronic Engineering*, 4:pp. 97–106, 2014.

[Hag05] S. Hagdahl. *Hybrid Methods for Computational Electromagnetics in Frequency Domain*. PhD thesis, Numerisk analys och datalogi (NADA), (2005).

[Han64] R. C. Hansen. *Apertures*, volume 1. Academic Press, New York, London, (1964).

[HCWC15] F. Huang, C. Chiu, T. Wu, and Y. Chiou. A circular-ring miniaturized-element metasurface with many good features for frequency selective shielding applications. *IEEE Transactions on Electromagnetic Compatibility*, 57:pp. 365–374, 2015.

[Heu73] J. C. Heurtley. Scalar rayleigh–sommerfeld and kirchhoff diffraction integrals: A comparison of exact evaluations for axial points. *Journal of the Optical Society of America*, 63(8):pp. 1003–1008, 1973.

[HH95] H. D. Hristov and M. H. A. J. Herben. Millimeter-wave fresnel-zone plate lens and antenna. *IEEE Transactions on Microwave Theory and Techniques*, 43:pp. 2779–2785, 1995.

[HL16] S. Gong H. Liu, Y. Liu. An ultra-wideband horizontally polarized omnidirectional connected vivaldi array antenna. International Symposium on Antennas and Propagation (ISAP), (2016).

[HLW] Y. Huang, J. Li, and G. Wen. *Active and Tunable Metamaterials*. IntechOpen.

[HPH+07] P. He, P. V. Parimi, Y. He, V. G. Harris, and C. Vittoria. Tunable negative refractive index metamaterial phase shifter. *Elect. Lett*, 43:pp. 1440–1441, 2007.

[HPS10] D. Huang, E. Poutrina, and D. R. Smith. Analysis of the power dependent tuning of a varactor-loaded metamaterial at microwave frequencies. *Applied Physics Letters*, 96(10):pp. 1–3, 2010.

[Hri00] H. D. Hristov. *Fresnel Zones in Wireless Links, Zone Plate Lenses and Antennas*. Norwood, MA:Artech House, (2000).

[Huy93] C. Huygens. *Traité de la lumière*. Dunod, (1993).

[IH91] W. A. Imbriale and R. Hodges. Linear phase approximation in the triangular facet near-field physical optics analysis of reflector antennas. *Applied Computational Electromagnetic Society Journal*, 6(2):pp. 74–85, 1991.

[JRM55] PhD. J. R. Mentzer. *Scattering and Diffraction of Radio Waves*. Pergamon Press, London and New York, (1955).

[JW70] Jr. J.D. Walton. *Radome Engineering Handbook: Design and Principle*. Georgia Institute of Technology Engineering Experiment Station Atlanta, Georgia, Marcel Dekker, INC, New York, (1970).

[KA13] T. Kohama and M. Ando. Numerical integration of physical optics for 2-dimensional scatterer using fresnel zone numbers with frequency-independent computation time. In *International Symposium on Electromagnetic Theory*, pages pp. 789–791. IEEE, (2013).

[KA18] V. S. Kumbhar and M. S. Andhare. Review on performance enhancement techniques for microstrip patch antenna using metamaterials. *International Journal of Recent Trends in Engineering and Research*, 3(11):pp. 123–129, 2018.

[KO60] R. King and G.H. Owyang. Complementarity in the study of transmission lines. *IEEE Trans.Microw. Theory Tech.*, 8:pp. 172–181, 1960.

[Kon86] J. A. Kong, editor. *Electromagnetic Wave Theory*. John Wiley and Sons., USA, (1986).

[Kot23] F. Kottler. Electromagnetische theorie der beugung an schwarzen schirmen. *Ann. Phys. (Leipzig)*, 71:pp. 457–508, 1923.

[Koz10] D. J. Kozakoff. *Analysis of Radome-Enclosed Antennas*. Artech House, Boston, London, second edition, (2010).

[KPDRT18] D. H. Kwon, G. Ptitcyn, A. Díaz-Rubio, and S. A. Tretyakov. Physical conditions for full control of transmission through non-reflecting metasurfaces. *2nd URSI Atlantic Radio Science Meeting, AT-RASC*, pages pp. 1–3, 2018.

[KRCB12] G. Kitic, V. Radonic, and V. Crnojevic-Bengin. Soil moisture sensors based on metamaterials. *Songklanakarin Journal of Science ad Technology*, 34(6):pp. 689–693, 2012.

[KS10] N. Kundtz and D. R. Smith. Extreme-angle broadband metamaterial lens. *Nature Materials*, 9:pp. 129–132, 2010.

[Lah16] A. Lahiri. *Basic Optics: Principles and Concepts*. Elsevier, (2016).

[LFHB14] D. Lin, P. Fan, E. Hasman, and M. L. Brongersma. Dielectric gradient metasurface optical elements. *Science*, 345:pp. 298–302, 2014.

[LG17] J. Liu and L. Guo. Fast shadowing computation for physical optics integrals in terms of levin method. *IEEE Antennas and Wireless Propagation Letters*, 16:pp. 1767–1770, 2017.

[Lia18] R. Lian. On huygens' principle, extinction theorem, and equivalence principle (inhomogeneous anisotropic material system in inhomogeneous anisotropic environment). *arXiv:1804.05760*, pages pp. 1–15, 2018.

[LJZZ15] R. Liu, C. Ji, Z. Zhao, and T. Zhou. Metamaterials: Reshape and rethink. *Engineering*, 1(2):pp. 179–184, 2015.

[Lov01] A. E. H. Love. The integration of the equations of propagation of electric waves. *Phil. Trans. Roy. Soc. London, Ser. A*, 197:pp. 1–45, 1901.

[LPC+17] I. Lee, Y. B. Park, H. Chun, Y. Kim, and I. Hong. Design of active frequency selective surface with curved composite structures and tunable frequency response. *International Journal of Antennas and Propagation*, 2017:pp. 1–10, 2017.

[Lud68] A. Ludwig. Computation of radiation patterns involving numerical double integration. *IEEE Transactions on Antenna and Propagation*, 16(6):pp. 767–769, 1968.

[Mac12] H. M. Macdonald. The effect of produced by an obstacle on a train of electric waves. *Phil. Trans. Royal Soc. London, Series A. Math. Phys. Sc.*, 212:pp. 299–337, 1912.

[Mated] MathWorks. Equation solving algorithms@ONLINE. https://de.mathworks.com/help/optim/ug/equation-solving-algorithms.html, 2019 (accessed).

[Max65] J. C. Maxwell. A dynamical theory of the electromagnetic field. *Phil. Trans.*, 166:pp. 459–512, 1865.

[MB10] A. A. Mudar and N. Behdad. Low profile, high selective, dual-band frequency selective surfaces with closely spaced bands of operation. *IEEE Transactions Antennas Propagation*, 58(12):pp. 4042–4050, 2010.

[MC10] P. J. Michael and P. M. Corcoran. Asymmetric radome for phased antenna arrays, us20100039346a1@ONLINE. https://patents.google.com/patent/US20100039346A1/en, 2010.

[McG86] D. McGrath. Planar three-dimensional constrained lenses. *IEEE Transactions on Antennas and Propagation*, 34:pp. 46–50, 1986.

[MDP48] C. G. Montgomery, R. H. Dicke, and E. M. Purcell. *Principles of Microwave Circuits*. Number 8 in Massachusetts Institute of Technology, Radiation Laboratory Series. McGraw-Hill Book Company, (1948).

[Meced] Creative Mechanisms. Everything you need to know about polypropylene (pp) plastic @ONLINE. https://www.creativemechanisms.com/blog/all-about-polypropylene-pp-plastic, 2019 (accessed).

[Mem15] M. Memarian. *Controlling Electromagnetic Fields Using Periodic Structures: Gratings, Metamaterials, and Photonic Crystals*. PhD thesis, Graduate Department of Electrical and Computer Engineering University of Toronto, (2015).

[Mey15] G. Joel Meyer. Polyurethane foam: Dielectric materials for use in radomes and other applications. Technical report, General Plastics Manufacturing Company, 2015.

[MH13] I. McGregor and K. M. Hock. Complementary split-ring resonator-coupled traveling wave accelerating structure. *Physical Review Special Topics. Accelerators and Beams*, 16(8):pp. 1–9, 8 2013.

[MK11] S. E. Mendhe and Y. P. Kost. Metamaterial properties and applications. *International Journal of Information Technology and Knowledge Management*, 4(1):pp. 85–89, 2011.

[MM01] A. S. Marathay and J. F. McCalmont. Vector diffraction theory for electromagnetic waves. *Journal of the Optical Society of America A*, 18(10):pp. 2585–2593, 2001.

[MPM95] T. D. McGrath, M. P. Proudfoot, and A. M. Mehalic. The microstrip constrained lens. *Microwave Journal*, 38(1), 1995.

[Mun00] B. A. Munk. *Frequency selective surfaces: theory and design*, volume 29. Wiley Online Library, (2000).

[NAM10] G. Nicolas, P. Aldo, and D. A. McNamara. Thin microwave quasi-transparent phase-shifting surface(pss). *IEEE Transactions on Antennas and Propagation*, 58(4):pp. 1193–1201, 2010.

[Naq16] J. Naqui. *Symmetry Properties in Transmission Lines Loaded with Electrically Small Resonators*. Springer International Publishing Switzerland, (2016).

[Nas96] B.M. Nasir. Radome materials, fabrication, design with applications and theory, and frequency selective surface techniques. IEE Colloquium on Advances in Electromagnetic Screens, Radomes and Materials, (1996).

[NIKS13] X. Ni, S. Ishii, A. V. Kildishev, and V. M. Shalaev. Ultrathin, planar, babinet inverted plasmonic metalenses. *Light: Science and Applications*, 2:pp. 1–6, 2013.

[NJ15] S. Narayan and R. M. Jha. Electromagnetic techniques and design strategies for FSS structure applications. *IEEE Antennas and Propagation Magazine*, 57(5):pp. 135–158, 2015.

[Orfed] S. J. Orfanidis. Electromagnetic waves and antennas (chapters 1, 2, 5) @ONLINE. http://eceweb1.rutgers.edu/~orfanidi/ewa/, 2019 (accessed).

[OT17] A. V. Osipov and S. A. Tretyakov. *Modern Electromagnetic Scattering Theory with Applications*. John Wiley & Sons, (2017).

[Par18] K. Parveen. Metamaterials: Types, applications, development, and future scope. *International Journal of Advance Research, Ideas and Innovations in Technology*, 4(3):pp. 2325–2327, 2018.

[Pat88] P. H. Pathak. *Techniques for High Frequency Problems, Antenna Handbook*. Springer, (1988).

[Pen00] J. B. Pendry. Negative refraction makes a perfect lens. *Phys. Rev. Lett.*, 85:pp. 3966–3969, 2000.

[PG13] G. Prema and P. Gayatri. A frequency reconfigurable rotatable antenna design for cognitive radio systems. *International Journal of Engineering Research and Technology (IJERT)*, 63(5):pp. 1342–1349, 2013.

[PHA+08] J. Parsons, E. Hendry, B. Auguié, W. L. Barnes, and J. R. Sambles. Localised modes of sub-wavelength hole arrays in thin metal films. *Proceedings of SPIE - The International Society for Optical Engineering*, (031005):pp. 1–9, 2008.

[PSK05] D. Peroulis, K. Sarabandi, and L. P. B. Katehi. Design of reconfigurable slot antennas. *IEEE Transactions on Antennas and Propagation*, 53(2):pp. 645–654, 2005.

[PYQG15] F. Wei P.-Y. Qin and Y. J. Guo. A wideband-to-narrowband tunable antenna using a reconfigurable filter. *IEEE Transactions on Antennas and Propagation*, 63(5):pp. 2282–2285, 2015.

[QHT09] C. Qiang, M. F. Hui, and J. C. Tie. Broadband planar luneburg lens based on complementary metamaterials. *Applied Physics Letters*, 95:181901, 2009.

[Rao05] S. S. Rao. *The Finite Element Method in Engineering*. Elsevier, USA, (2005).

[RLJ17] Z. Zhao R. Liu and J. Jin. Metamaterial, metamaterial preparation method and metamaterial design method, May 16 (2017). US Patent 9,653,815.

[Rot84] W. Rotman. Analysis of an EHF aplanatic zoned dielectric lens antenna. *IEEE Transactions on Antennas and Propagation*, AP-32(6):pp. 611–617, 1984.

[Run07] O. Runborg. Mathematical models and numerical methods for high frequency waves. *Commun. Comput. Phys*, 2(5):pp. 827–880, 2007.

[RW59] B. Richards and E. Wolf. Electromagnetic diffraction in optical systems. *Proc. R. Soc. London Ser. A*, 253:pp. 358–379, 1959.

[Sam84] S. Samuel. *Microwave Antenna Theory and Design*. Peter Peregrinus Ltd, (1984).

[SC39] J. A. Stratton and L. J. Chu. Diffraction theory of electromagnetic waves. *Phys. Rev.*, 56:pp. 99–107, 1939.

[SCC+10] S. Shelley, J. Costantine, C. G. Christodoulou, D. E. Anagnostou, and J. C. Lyke. Fpga-controlled switch-reconfigured antenna. *IEEE Antennas and Wireless Propagation Letters*, 9:pp. 355–358, 2010.

[SCP13] D. Shrekenhamer, W.-C. Chen, and W. J. Padilla. Liquid crystal tunable metamaterial absorber. *Physical Review Letters*, 110(17):pp.1–5, 2013.

[Sha15] A constitutive description of nonlinear metamaterials through electric, magnetic, and magnetoelectric nonlinearities. In I. V. Shadrivov, M. Lapine, and Y. S. Kivshar, editors, *Nonlinear, Tunable and Active Metamaterials*. Springer International Publishing, (2015).

[Sha18] R. Shavit. *Radome electromagnetic theory and design*. IEEE Press, Wiley, First edition, (2018).

[Sih07] A. Sihvola. Metamaterials in electromagnetics. *ScienceDirect*, page pp. 2–11, 2007.

[Sih09] A. Sihvola. Metamaterials: A personal view. *RadioEngineering*, 18(2):pp. 90–94, 2009.

[SMK06] I. V. Shadrivov, S. K. Morrison, and Y. S. Kivshar. Tunable split-ring resonators for nonlinear negative-index metamaterials. *Opt. Express*, 14:pp. 9344–9349, 2006.

[Som06] C. G. Someda. *Electromagnetic Waves*. Taylor and Francis Group, 2 edition, (2006).

[SS68] B. L. Seidel and C. T. Stelzried. A radiometric method for measuring the insertion loss of radome materials. *IEEE Transactions on Microwave Theory and Techniques*, 16(9):pp. 625–628, 1968.

[SS03] D. L. Sengupta and T. K. Sarkar. Maxwell, Hertz, the Maxwellians, and the early history of electromagnetic waves. *IEEE Antennas and Propagation Magazine*, 45(2):pp. 459–512, 2003.

[ST] P. Sumithra and D. Thiripurasundari. A review on computational electromagnetics methods. *Advanced Electromagnetics*, 6:pp. 42–55.

[Sug18] S. Suganthi. Optimized metamaterial loaded square fractal antenna for gain and bandwidth enhancement. 12th International Congress on Artificial Materials for Novel Wave Phenomena (Metamaterials), (2018).

[SV07] Z. Sheng and V. V. Varadan. Tuning the effective properties of metamaterials by changing the substrate properties. *Journal of Applied Physics*, 101(1), 2007.

[TBM+14] J. P. Turpin, J. A. Bossard, K. L. Morgan, D. H. Werner, and P. L. Werner. Reconfigurable and tunable metamaterials: a review of the theory and applications. *International Journal of Antennas and Propagation*, (429837):pp. 1–18, 2014.

[TC09] Y. Tawk and C. G. Christodoulou. A new reconfigurable antenna design for cognitive radio. *IEEE Antennas and Wireless Propagation Letters*, 8:pp. 1378–1381, 2009.

[Teced] Zebra Technologies. Choosing the right wireless network for expansive outdoor spaces@ONLINE. https://www.zebra.com/content/dam/zebra_new_ia/en-us/solutions-verticals/product/Narrowband%20Digital%20Wireless/9160%20G2%20Narrowband%20Wireless%20Gateway/White%20Papers/narrowband-white-paper-english.pdf, 2019 (accessed).

[Ton17] X. C. Tong. *Functional Metamaterials and Metadevices*, volume 262. Springer Series in Materials Science, September (2017).

[Tre03] S. A. Tretyakov. *Analytical modeling in applied electromagnetics*. Artech House, (2003).

[Tre15] S. A. Tretyakov. Metasurfaces for general transformations of electromagnetic fields. *Phil. Trans. R. Soc. A*, 373(2049):pp. 1–10, 2015.

[TUZ17] S. Tretyakov, A. Urbas, and N. Zheludev. The century of metamaterials. *Journal of Optics*, 19(080404):pp. 1–3, 2017.

[Ufi08] P. Y. Ufimtsev. New insight into the classical Macdonald physical optics approximation. *IEEE Antennas and Propagation Magazine*, 50(3):pp. 299–337, 2008.

[Uma89] K. Umashankar. *Introduction to Engineering Electromagnetic Fields*, volume 4. World Scientific, (1989).

[Ves68] V. G. Veselago. The electrodynamics of substances with simultaneously negative values of permittivity and permeability. *Sov. Phys. Usp.*, 10(4):pp. 509–514, 1968.

[Wal01] R. M. Walser. Electromagnetic metamaterials. In *Complex Mediums II: Beyond Linear Isotropic Dielectrics*, volume 4467, pages 1–16. International Society for Optics and Photonics, (2001).

[Wil85] J. C. Wiltse. The fresnel zone-plate lens. *Proc. SPIE 0544, Millimeter Wave Technology III*, 1985.

[You07] T. Young. *A Course of Lectures on Natural Philosophy and Mechanical Arts*. McGraw-Hill, London, UK, (1807).

[Yua15] Y. Yuan. Recent advances in trust region algorithms. *Mathematical Programming*, 151(1):pp. 249–281, 2015.

[zAB+07] E. Özbay, K. Aydin, S. Butun, K. Kolodziejak, and D. Pawlak. Ferroelectric based tuneable SRR based metamaterial for microwave applications. In *Proceedings of European Microwave Conference, EUMC*, page 497–499. IEEE, 2007.

[ZHW+12] J. Zhong, Y. Huang, G. Wen, H. Sun, and W. Zhu. The design and applications of tunable metamaterials. *Procedia Engineering, SciVerse ScienceDirect*, 29:pp. 802–807, 2012.

[ZKD+07] Q. Zhao, L. Kang, B. Du, B. Li, and J. Zhou. Electrically tunable negative permeability metamaterials based on nematic liquid crystals. *Applied Physics Letters*, 90(1), 2007.

[zOE17a] E. Öziş, A. V. Osipov, and T. F. Eibert. Metamaterials for microwave radomes and the concept of a metaradome: Review of the literature. *International Journal of Antennas and Propagation*, 2017:pp.1–13, 2017.

[zOE17b] E. Öziş, A. V. Osipov, and T. F. Eibert. Physical optics and full-wave simulations of transmission of electromagnetic fields through electrically large planar meta-sheets. *Advances in Radio Science: ARS*, 15:pp.29–35, 2017.

[zOE18] E. Öziş, A. V. Osipov, and T. F. Eibert. A semi-analytical approach for fast design of microwave metasheets with circular metal rings on dielectric substrates. *Progress In Electromagnetics Research C*, 88:pp. 13–25, 2018.

[zOE20] E. Öziş, A. V. Osipov, and T. F. Eibert. Design of a metalens for correcting the phase distortions of a hemispheric dielectric radome in the ka band. *Progress In Electromagnetics Research M*, 90:pp. 47–58, 2020.

Publications of Author

- E. Öziş, A. V. Osipov and T. F. Eibert, "Analyzing scattering and reflection from metasheets of bi-anisotropic particles," *ONERA-DLR Aerospace Symposium,* Köln, Germany, 2014.
- E. Öziş, A. V. Osipov and T. F. Eibert, "Enhancing microwave radomes with metamaterials," *Kleinheubacher Tagung,* Miltenberg, Germany, 2015.
- E. Öziş, A. V. Osipov and T. F. Eibert, "Metamaterials for microwave radomes: an overview," *Progress in Electromagnetics Research Symposium*, Prague, 2015.
- E. Öziş, A. V. Osipov and T. F. Eibert, "Physical optics and full wave simulations of transmission of electromagnetic fields through electrically large planar meta-sheets,"*Kleinheubacher Tagung,* Miltenberg, Germany, 2016.
- E. Öziş, A. V. Osipov and T. F. Eibert, "An approximation for reflection and transmission coefficients of periodic arrays of metal rings and circular slots," *Kleinheubacher Tagung,* Miltenberg, Germany, 2017.
- E. Öziş, A. V. Osipov and T. F. Eibert, "Physical optics and full-wave simulations of transmission of electromagnetic fields through electrically large planar meta-sheets," *Advances in Radio Science*, vol. 15, pp. 29-35, 2017.
- E. Öziş, A. V. Osipov and T. F. Eibert, “Metamaterials for microwave radomes and the concept of a metaradome: review of the literature,” *International Journal of Antennas and Propagation*, vol. 2017, Article ID 1356108, 13 pages, 2017.
- E. Öziş, A. V. Osipov and T. F. Eibert, "A semi-analytical model for transmission coefficient calculation for metal planar rings in meta-sheets in the microwave region," *Progress in Electromagnetics Research Symposium*, Singapore, 2017.

Publications of Author

- E. Kemptner, A. V. Osipov, E. Öziş, "Metamaterials for microwave radomes," *Annual Military Scientific Research*, vol.2016, pp.42-43, 2017.
- E. Kemptner, A. V. Osipov, E. Öziş, "Metamaterialien für Mikrowellenradome," *Wehrwissenschaftliche Forschung*, vol.2016, pp.42-43, 2017.
- A. V. Osipov, E. Kemptner, E. Öziş and H. Kobayashi , "Microwave metamaterials for increased survivability of future systems (invited)," *IEICE Workshop of Technical Committee on Space, Aeronautical and Navigational Electronics (IEICE-SANE)*, IEICE Technical Report, vol. 116, pp. 35-40, 2017.
- E. Öziş, A. V. Osipov and T. F. Eibert, "A Semi-analytical approach for fast design of microwave metasheets with circular metal rings on dielectric substrates," *Progress in Electromagnetics Research C*, vol. 88, pp. 13-25, 2018.
- A. V. Osipov, E. Kemptner, E. Öziş, and S. Umrath, "Ausgewählte Problemstellungen zur Radartechnik in der Anwendung für hochagile Flugkörper," *Proceedings of the Angewandte Forschung für Verteidigung und Sicherheit in Deutschland*, Bonn, Deutschland, 2018.
- E. Öziş, A. V. Osipov and T. F. Eibert, "Design of a metalens for correcting the phase distortions of a hemispheric dielectric radome in the Ka band," *Progress In Electromagnetics Research M*, vol. 90, pp. 47-58, 2020.